The migration of single hot Jupiters

Balance of evidence tips towards dynamical and tidal evolution

Submitted by
Mohammad Nawal Husnoo
to the University of Exeter as a thesis for the degree of
Doctor of Philosophy in Physics
March 2013

(Signature) .....

Abstract

In this thesis, we revisit the seventeen year old question of how hot Jupiters got to their short period orbits, given that gas-giant planet building is supposed to take place beyond the ice-line at about 3 AU. Two major theories are generally used to explain this mystery. Firstly, exchange of energy and angular momentum between the newly-built planet and the progenitor dust and gas disk could result in planetary migration to a short period. This is generally believed to result in planets on circular orbits, with orbital angular momenta that are aligned with the host star spin. The competing theory which has gained more support in recent years, is that gravitational interactions leading to planet-planet scattering and/or Kozai interactions with massive and distant objects caused the planets to migrate violently (scattering) or slowly (Kozai) to short period, eccentric and misaligned orbits. These orbits are then expected to circularise and align under tidal interactions with the host star. In addition, the host star is expected to show evidence of spin-up if the tide on the star is strong enough.

Our contribution to this field is to provide additional support for the scenario involving dynamical interaction and tidal damping. We present observational evidence in the form of 158 new radial velocity measurements for 12 planets and a reanalysis of existing radial velocity data and photometric constraints from the literature for a total of 64 planetary systems. We also critically consider a further 30 newly announced planets from the literature. We show that there is no evidence for a finite eccentricity in several cases that were previously claimed to be "exceptions" to the observed trend that *close-in planets are on circular orbits* and the generally accepted reason that *they underwent strong tidal interactions*. We also show that the dissipative effect of tides raised in the planet by the star and vice versa explain all the eccentricity and spin-orbit alignment measurements available for transiting planets. We find evidence for excess rotation of the star in 6 systems, showing that heavy and close-in objects can exert strong tidal effects on the star. Hot Jupiters on circular orbits clump on the mass-period relation, which thus appears to be related to the stopping mechanism of orbital migration for hot Jupiters.

Contents

List of Figures

List of Tables

Author's declaration

The work described in this thesis was done in collaboration with other researchers at several different institutions. The research problem itself ("Is correlated noise affecting the observational support for tidal effects in the sample of transiting exoplanets?") was the idea of Frédéric Pont.

The work in Section 3.5 is my own work, with only supervisor oversight from Frédéric Pont. I adapted the approach as described by Sivia (2006), keeping in mind the importance of red-noise as described by Pont, Zucker, and Queloz (2006).

Chapter 4 contains material covered in the paper by Husnoo et al. (2011), which I wrote by expanding a 2 page template that my supervisor Frédéric Pont provided me, along with a lot of advice, into the final 9 page paper. I performed the analysis myself, but I received a lot of advice on the details of the writing-up through extensive discussions with the other co-authors, especially from Tsevi Mazeh (Tel Aviv University), Claire Moutou (Laboratoire d'Astrophysique de Marseille), Guillaume Hébrard (Institut d'Astrophysique de Paris) and François Bouchy (Institut d'Astrophysique de Paris). The radial velocity measurements for the orbits of WASP-12 and WASP-14 were obtained by several members of the SOPHIE team (Anne Eggenberger, Isabelle Boisse, Rodrigo Díaz and Luc Arnold) and reduced by Guillaume Hébrard on behalf of Frédéric Pont. The data for the Rossiter-McLaughlin sequence were captured by the SOPHIE Consortium team on behalf of Elaine Simpson (Queens University Belfast).

Chapters 5 and 6 contain material covered in the paper by Husnoo et al. (2012). Again, I performed all the analysis and wrote the paper myself, but benefited from extensive discussions with the co-authors Frédéric Pont, Tsevi Mazeh and Daniel Fabrycky on the details of the presentation of the paper. The initial results in this paper were originally published in a paper by Pont et al. (2011), which my supervisor wrote and to which I contributed the initial results. This latter paper benefited from discussions in Tel-Aviv with Tsevi Mazeh, and Daniel Fabrycky (Harvard-Smithsonian Centre for Astrophysics). The SOPHIE data in these latter two papers were reduced by Guillaume Hébrard on behalf of Frédéric Pont, while the HARPS data was obtained on behalf of Tsevi Mazeh by ESO. All three papers benefited hugely from the detailed and careful reports of the anonymous referees. I am also grateful to Gilles Chabrier and Tim Naylor for their enthusiastic comments at various points, on tidal effects and Bayesian data analysis, respectively.

The code used to model the Rossiter-McLaughlin effect in Section 3.1.2 was initially implemented by Frédéric Pont using the equations of Giménez (2006) in Python, but the code was too slow for interactive use. I ported this code to C, profiled it, implemented several improvements to speed up the code, and wrote wrapper functions so that the faster version could be called from Python. The code for modelling the transit lightcurve (Section 3.2) was implemented by Suzanne Aigrain following Mandel and Agol (2002), and I used this as is. The code for the MCMC and radial velocity analysis (Section 3.1) was initially implemented by Frédéric Pont in Python, but I have re-implemented it from scratch in Python to include multiple datasets, and ported the slower subroutines to C to speed them up.

The summaries in Sections 7.1.1 and 7.1.2 refer to my own work, whenever they refer to this thesis. The only input from the co-authors at that stage was

to ask questions about the procedure to ensure I wasn't doing anything obviously wrong. The work in Section 7.1.3 is where the co-authors Frédéric Pont, Tsevi Mazeh, and Daniel Fabrycky contributed most, by helping with the interpretation of the Figure 6.1 in terms of the Roche limit, and suggesting the reference to Ford and Rasio, 2006. The actual comparison with the works of Winn et al. (2010) was my own work, although the division of "aligned" and "misaligned" at $\lambda = 30^{o}$ is the suggestion of Frédéric Pont. The Figures 6.2, 6.3 and 6.4 were my own idea, although Frédéric Pont suggested that I use colours to differentiate between "normal" (circular/aligned/normal rotation) and "interesting"(eccentric/misaligned/fast rotation) rather than symbols. The latter suggestion improved the prevention enormously.

Acknowledgments

I am grateful to Matthew Bate and Chris Brunt, who conducted my interview for a PhD position at the University of Exeter. By granting me the Exoplanet Science Strategy scholarship, they gave me the opportunity to become a scientific researcher, which is something I dreamed about since I was about 13 years old.

I am immensely grateful to my supervisor, Frédéric Pont, who showed me the delights of the Bayesian approach to statistics and science, as well as mentored me through the perilous obstacle course that is a PhD programme. His scientific flair and his numerous and regular contributions to the field are well known, but he still finds time to read around all manners of topics, which have led to a number of stimulating conversations over a glass at the pub after our meetings (also at the pub, usually).

I am also grateful to my boyfriend Daniel Griffin, who has been there for me for the last three years, and has supported me through the hard times when my research progress stalled, and also helped me celebrate the little victories along the way.

I am grateful to Tim Naylor, Nathan Mayne, Isabelle Baraffe, Peter Petrov and Pete Vukusic, for providing me with a lot of advice and pastoral support during the harder times.

I am thankful for my parents (Feeroza and Parvez) and brother Sultan, who kept awake late into the night (four timezones ahead) once a week to chat with me. My parents also made a lot of sacrifices to give me the education that allowed me to get this far in following my dreams.

I am also thankful for my office mates Catherine Huitson, Alex Pettitt and Paul Wilson, from whom I have learnt a lot, and with whom I have had such great times! Last but not least, I am thankful to have such good friends as Adam Armstrong and Andy Birkin, who patiently put up with all my rants and frustrations, as well as my moments of joy during the last seven years or so.

Last but not least, I am grateful to my external examiner, Carole Haswell and my internal examiner, Matthew Browning, for the thesis defence exercise, which was excellent fun.

Chapter 1

Introduction

In this chapter, we describe the problem of migration for hot Jupiters. We describe the two major theories typically used to explain this mystery, and then look at the evidence that was accumulating in favour of strong tidal interactions in these systems as of 2009. We then consider how the matter became more confusing as new observations of eccentricities were made available. In fact, several very short period systems were initially claimed to have small but finite eccentricities, undermining the observed trend for tidal circularisation. Exotic scenarios were postulated, but it eventually became clear that many of these "exceptions" were spurious. We also present an outline of the rest of the thesis.

1.1 Other worlds out there

About five centuries ago, planet Earth was demoted from being considered to be the center of the Universe to being a mere planet in the Solar System, orbiting the Sun (Copernicus, 1965, First Published: 1543). Our Solar System remained the only known example of such a system for the next five centuries, until Wolszczan and Frail (1992) announced the first exoplanet known to mankind that would be confirmed, using radio observations of the pulsar PSR1257+12. The first exoplanet to orbit a Sun-like star was announced by Mayor et al. (1995), around the main sequence star 51 Peg.

According to the International Astronomical Union (2006), a planet is a body that has achieved a nearly round shape (i.e. in hydrostatic equilibrium) because rigid body forces are outweighed by the self-gravity. The official definition includes a heliocentric orbit and an orbital path cleared of debris, so in the case of an exoplanet, we require the body to be in orbit around a star.

1.2 Planet formation

Almost all of our knowledge of planet formation comes from observational and theoretical studies carried out for the Solar System (e.g. see references in Lissauer, 1993, for this Section). According to the Solar Nebula theory (Pollack, 1984), the Sun is thought to have formed from the collapse of a region a giant molecular cloud. A part of the original material ended up in a flattened protoplanetary disk around the young Sun, due to the conservation of angular momentum. This disk was made up of gas and dust, from interstellar grains and

stellar nebula condensates. The dust grains began to grow by accretion, producing progressively larger rocks, which keep growing in an oligarchic manner into protoplanets (Pollack et al., 1996). These protoplanets stop growing when they have cleared the region around them, and are unable to interact and collide with their neighbours.

The planetary composition depends on the formation distance from the Sun (Barshay and Lewis, 1976). Terrestrial planets form in the inner part of the Solar System, where volatile materials such as water and other ices are depleted and refractory materials abound. Gas giants, on the other hand, are formed at a distance of several AU from the host star, beyond the ice-line. This name refers to the fact that that is the region where the volatile materials exist in condensed form due to the lower temperature. In the Core Accretion theory, they initially form in the same way as terrestrial planets, but as the mass increases past a critical core mass (Mizuno, 1980), the gravitational effects on the surrounding gas gets stronger, and the planet can accrete gas in the form of a hydrogen and helium envelope. The gas accretion then stops when the protoplanetary disk evaporates after $\sim 10^6 - 3 \times 10^7$ years due to the brightening T-Tauri star, the planet accretes all the gas available at its orbit, or a gap forms in the disk (Lissauer, 1993, and references therein.). In the case of exoplanets, Levison, Lissauer, and Duncan (1998) studied the formation of giant planets from planetary embryos. A competing scenario for the formation of gas giants is the direct gravitational collapse of a region of the protostellar nebula (Boss, 1997), which is thought to be the formation mechanism for planets at ~ 100 AU (Boley, 2009).

1.3 Close-in planets

The discovery of an exoplanet around the solar-type star 51 Peg (Mayor and Queloz, 1995) was an exciting time for the astrophysics community, because the existence of planets around other stars had been the object of speculations for a long time. The biggest surprise, however, was the short period of the orbit. This kickstarted the study of such close-in planets, called hot Jupiters because of the high temperatures reached from the intense stellar insolation. Since 1995, several hundred such hot Jupiters have been discovered, with a large range of masses, radii, semi-major axes, and eccentricities.

Observational studies of the solar system gave no indications that such an extreme system as 51 Peg could exist, and according to the core accretion model, a gas giant cannot form that close to the star, because of the high temperature (Lin, Bodenheimer, and Richardson, 1996). The current radius and gravity of that planet makes it safe against Jeans escape (the escape velocity of hydrogen is sufficiently large as not to be exceeded by the atmosphere mean thermal speed) and hydrodynamic escape (where high energy radiation from the star is absorbed by hydrogen in the atmosphere, causing a planetary wind). In the early days of planet formation, however, the planet would have been at least ten times larger, and the surface gravity would have been a lot lower. This means that the Jeans and hydrodynamic evaporation rates would have been much higher. Stellar wind ablation would have been yet another obstacle to gas giant planet building at such a short period. Lin, Bodenheimer, and Richardson (1996) suggested that the planet must have formed beyond the ice-line at ~ 5 AU, and migrated inwards subsequently (see also Ida and Lin, 2004). Several scenarios (e.g. see

references in Ogilvie and Lin, 2004, for this Section) have been proposed to explain the migration of a gas giant to such a close orbit, and we review them in the following sections.

An alternative scenario is proposed by Ward (1997), where in-situ collapse of embryos (brought closer to the star by Type I migration) could also produce hot Jupiters. This would concentrate a large fraction of the disk's solid material in a small region, and should result in a planet rich in refractory and CHON materials. The higher density would then cause the planetary radius to be smaller than that for a planet with a composition dominated by hydrogen and helium. Given that so many close-in planets are found to have unexpectedly inflated radii (See Alonso et al., 2004; Bouchy et al., 2005; Charbonneau et al., 2000, etc.), this scenario is quite unlikely.

1.4 Disk migration

Goldreich and Tremaine (1980) studied the exchange of angular momentum between a body embedded in a disk and the disk itself, a scenario which applies to the rings of the Solar System giant planets, and the protoplanetary disk. Lin and Papaloizou (1986) studied the effects of a protoplanetary disk on protoplanets. Specifically, tidal interactions between the protoplanet and the disk could result in significant migration (Ward, 1997).

This migration of a giant planet, which clears a gap in the disk where it orbits, is called Type II migration (see Baruteau and Masset, 2012, for details of Type I migration of low mass planets in a disk, and Type III migration, of a planet in a massive disk.).

Type II migration was studied by Lin, Bodenheimer, and Richardson (1996) for the case of 51 Peg, and later by many others (see Baruteau and Masset, 2012, for copious references.). As Rasio and Ford (1996) point out, this model requires that the dissipative effect of the protoplanetary disk shuts down at a critical moment for the planet to survive. This would make such planets very rare, in contrast to observations.

One stopping mechanism, as described by Lin, Bodenheimer, and Richardson (1996), is the tidal interaction of the migrating planet with the rapidly spinning young star. Angular momentum transfer from the stellar rotation to the planetary orbit would cause the planet to migrate outward, balancing the inward migration due to the disk. Given that the star is rotating slower than the orbital motion today, it means that there was a time when the star slowed down just enough for the planet to reach corotation with the star. This would cause the angular momentum transfer to reverse direction, and the planet would plunge inwards. To avert this catastrophe, the star would need to have contracted enough by that time to make the infall timescale much longer than expected for the young star. Thus, a very precisely defined co-evolution of stellar spindown, internal contraction, and tidal interaction would be necessary to ensure the planet survives (Rasio and Ford, 1996).

A different suggestion, as described by Lin, Bodenheimer, and Richardson (1996), is that the planet migrates inwards in the protoplanetary disk until it reaches a cavity in the disk. This cavity is created by the stellar magnetosphere, which truncates the disk at about 0.08 AU, which is slightly less than the corotation radius. A planet that makes it to 0.05 AU still experiences angular momen-

tum exchange with the disk, but it is reduced by a factor M_p/M_* due to the 2:1 resonance. Tidal interactions at this point would still cause the planet to migrate inwards, but the migration timescale is now much longer than the contraction timescale, and the migration stops. Again, this scenario suffers from the fine tuning of the timescales described above.

A third mechanism has been invoked to account for the stopping mechanism for the migration of hot Jupiters to distances significantly larger than 0.05 AU but still well within the ice-line. In this case, the amount of migration that happens depends on the mass of the planet, and the mass of the disk, its viscosity, and lifetime. As long as the gas disk dissipates before the planet has plunged into the star, the planet can survive as a hot Jupiter at an intermediate period (Trilling, Lunine, and Benz, 2002, and see references in Ogilvie & Lin 2004).

There are several difficulties with the disk migration scenario. For example, the eccentricity and spin-orbit misalignment angle distribution are difficult to reproduce. Papaloizou, Nelson, and Masset (2001) looked at planets with masses between 1 and 30 Jupiter masses, interacting tidally with a disk. They found that objects with masses below 10 $M_j$remain on circular orbits, in contrast to observations (e.g. WASP-14b, $M_p = 7.34\ M_j$, $e = 0.088 \pm 0.003$, Joshi et al. 2009). Papaloizou, Nelson, and Masset (2001) did find a transition region for 10 $M_j \leq M_p \leq 20\ M_j$, and growth of eccentricity (up to about 0.25) for objects above 20 M_j. Still, this scenario struggles to explain the large eccentricities of objects like HD 80606b ($e = 0.933 \pm 0.001$, Naef et al. 2001), HD17156b ($e = 0.675 \pm 0.004$, Barbieri et al. 2007) and HAT-P-2b ($e = 0.517 \pm 0.003$, Bakos et al. 2007).

Rice, Veljanoski, and Collier Cameron (2012) use the results of Armitage (2007) at the end of disk migration, as a starting point for secular tidal interactions, to predict the distribution of hot Jupiters. In practise, they also find that disk migration alone is insufficient to predict the observed distribution, and they have to invoke a stopping mechanism, in the form of the magnetospheric cavity leading to a pile up of planets at 4 days. Even then, they have to artificially inflate the expected pile-up by about 20–30% to match the observations. Despite matching the eccentricity and period distributions, this approach completely ignores the wealth of information in the observed distribution of stellar obliquities relative to the orbital plane, as summarised by Winn et al. (2010) and Triaud et al. (2010). In particular, Winn et al. (2010) find a strong correlation with the distribution of obliquities and the stellar effective temperature (see Section 1.5), which is simply not addressed by the disk migration scenario.

1.5 Dynamical interactions and tidal circularisation

The main competing theory of hot Jupiter migration is the scenario proposed by Rasio and Ford (1996), which involves an exchange of angular momentum between two or more giant planets. This dynamical instability can be violent, in which case one planet either gets ejected from the system, or moves to a much larger orbit. The other planet gets kicked inward into an eccentric, short period orbit. Under the right circumstances (small periastron distance, large dissipation factor in the star, the planet or both), this eccentric orbit can then be damped by tidal dissipation, leaving the planet on a tight, circular orbit. Otherwise, the planet may be left on an intermediate period orbit, with a finite eccentricity. The Kozai mechanism (Kozai, 1962) is another way to migrate a planet to a

point where tidal circularisation can produce a circular planet on a tight orbit. We review the gravitational scattering and Kozai scenarios here, but defer the discussion of tidal circularisation till Chapter 2.

1.6 Gravitational scattering

In the Rasio and Ford (1996) scenario, the planets form as described by standard formation theory (see section 1.2) and interact later in their lifetimes. For example, if one planet has a different secular orbital evolution, their paths might bring them close enough to interact. Another avenue for interaction is an increase in their masses through accretion, turning a formerly stable system into an unstable one. When Rasio and Ford (1996) studied simulated systems with two gas giant planets of equal masses, they found that about half of the simulations ended in a merger, with the resultant planet found at a rather unexciting orbital distance, comparable to the initial separation. On the other hand, in those systems where the two planets did not merge, one of them moved away from the system with a small positive total energy (kinetic energy+potential energy), which meant it was leaving the system on a hyperbolic orbit. To conserve total energy and angular momentum, the planet that got left behind moved into a shorter period, eccentric orbit. Even though many of those planets remain on orbits with periods $\gtrsim$ 0.4 year, some do achieve a very high eccentricity (close to 1), and consequently have a very short periastron distance. These could then experience tidal dissipation, as explained in the next subsection, to achieve a tight circular orbit. Rasio and Ford (1996) note that they only found systems with eccentricities too small to circularise in less than about one billion years, but systems with higher eccentricities that circularise a lot faster should be possible in principle. Weidenschilling and Marzari (1996) found essentially identical results for two equal mass planets, and they cautioned that their simulations did not form enough star-grazing orbits. They suggested that two processes may be at work, gravitational scattering producing the intermediate period eccentric orbits, while the short period circular orbits involve disk migration and tidal stopping. This is in contrast to the present study, where we support the view that the majority of hot Jupiters migrate and stop by gravitational scattering and tidal interactions alone.

1.6.1 Eccentricity distribution

A strong constraint on the migration scenario may be derived from the empirical distribution of orbital eccentricities for the gas giant exoplanets. In this case, we need to exclude the close-in planets ($P_{orbit} \lesssim$ 10d), because they are affected by tidal circularisation (see Section 6.2). Ford, Havlickova, and Rasio (2001) used numerical simulations of equal mass planets starting from just within the Hill stability region, extending the work done by Rasio and Ford (1996). Again, they found that the dominant outcome was either a merger or an ejection, depending on the ratio of the planet radius to the semi-major axis. The merger scenario is expected to produce a high proportion of circular orbits at an intermediate semi-major axis, in contrast to observations, which show a wide distribution of eccentricities for planets that don't undergo strong tidal interactions. Further, even for these systems where one planet gets ejected and the other is left on

an eccentric orbit, the resulting eccentricity distribution had a higher mean and smaller spread than observations (Ford, Havlickova, and Rasio, 2001).

Ford, Rasio, and Yu (2003) study two planets with unequal masses, and three equal mass planets. For two planets with unequal masses, they show that the resulting semi-major axis for the surviving planet (when the companion is ejected) is limited to $a_{final} \geq 0.5 a_{initial}$, with the lower limit corresponding to the equal mass case. The mean of the resulting eccentricity distribution, on the other hand, depends strongly on the mass ratio. The spread of each such distribution is small, but a spread of mass ratios could easily produce a wider distribution. For a plausible mass distribution that is consistent with the known exoplanet systems at the time, they showed that the computed eccentricity distribution matched the observed one (see Figure 3 of Ford, Rasio, and Yu, 2003). Incidentally, they even found a similar agreement with observations when they simulated equal mass three-planet systems.

Adams and Laughlin (2003) performed numerical simulations of crowded systems (10 planets), using several mass distributions for the planets. They found that giant planets with semi-major axis $a \sim 1$ AU and eccentricity in the whole range ($0 \leq e \leq 1$) can be produced, from planets initially found at $5\text{AU} \leq a \leq 30\text{AU}$. Papaloizou and Terquem (2001) studied the multi-planet case with $5 \leq N \leq 100$ planets initially lying up to 100 AU from the star, and found that close encounters with the star can occur for about 10% of their simulations.

Terquem and Papaloizou (2002) consider a system where a few massive planets (7–8 M_j) form at a distance of $\sim$ 100 AU, and a lower mass planet ($\sim$0.3–8 M_j) forms in a disk closer to the star. The low mass planet forms on a circular orbit, because of dissipation in the protoplanetary disk. The outer planets undergo dynamical interactions, which results in most of them getting ejected, but a few are left on eccentric orbits. Specifically, the massive planets are modelled as distant perturbers on eccentric orbits. When the protoplanetary disk dissipates, and the orbit of the less massive planet is free to evolve, it can undergo secular gravitational interaction with the massive planets and its eccentricity can grow. For the less massive planets that don't collide with the star, many can get close enough to undergo tidal circularisation.

The dynamical effects of giant planet migration are expected to inhibit terrestrial planet formation in the region outside the shortest periastron distance of any of the giant planets (Veras and Armitage, 2005). Veras and Armitage (2006) used numerical N-body simulations of triple planet systems with a realistic range of masses to study this effect statistically. Like others in this section, they obtained eccentricity distributions for the giant planets that were consistent with the non-tidally interacting observed exoplanets. To study the possibility that interaction with a residual disk might influence the outcome, Chatterjee et al. (2008) used an initial mass distribution and a semi-major axis distribution for gas giants as predicted by the core-accretion scenario, and carried out numerical simulations of the outcomes from gravitational scattering, both with and without a residual gas disk. Raymond, Armitage, and Gorelick (2010) performed a similar study, and both studies agree that the effects of the disk is mass dependent, and only seems to affect the low mass planets ($M_p < M_{\text{Saturn}}$). For the Jupiter mass planets, the results matched the observations quite well.

Jurić and Tremaine (2008) find similar results as Chatterjee et al. (2008), deriving a computed eccentricity distribution largely consistent with observations, although their simulations underpredict objects on circular orbits at intermediate

distances. They also predict misaligned objects, with a proportion of simulated systems $\gtrsim 10$ % that are highly inclined ($\gtrsim 25°$). In other simulations, Ford and Rasio (2008) found that the two planet scenario with unequal masses overpredicts the low eccentricity planets if the mass distributions vary over two orders of magnitude, whereas it overpredicts the high eccentricity planets for a mass distribution spanning one order of magnitude. They obtain good agreement with observations if they use an intermediate value. One remaining problem is that planet-planet scattering for two planets is maximally effective at pumping up the orbital eccentricity of the surviving planet for the equal mass case, where the resulting eccentricity is about 0.62 ± 14 (from simulations). In that case, orbital eccentricities exceeding $\gtrsim 0.8$ are quite surprising (e.g. HD 80606b, $e = 0.933 \pm 0.001$, Naef et al. (2001)).

From a purely observational perspective, Wright et al. (2009) find that planets in multi-planet systems have slightly smaller eccentricities than planets in single planet systems. In addition, they find that the two cases have different period distributions. The single planets tend to pile up at ~ 3 d, and show a jump in frequency near 1AU, whereas multi-planet have a more uniform distribution in log-period. This suggests that the multi planet systems survived the dynamical interactions, whereas the the single planet systems are the result of drastic event, leaving the surviving planet on a tighter orbit.

The higher eccentricities of massive planets

An interesting constraint from eccentricity measurements comes from the observation that higher mass objects tend to have higher eccentricities (Marcy et al., 2005). This would be surprising in the disk-migration scenario, as a larger object that originally formed on a circular orbit would require a larger perturbation to alter its orbit. Halbwachs, Mayor, and Udry (2005) argued that the objects beyond the tidal circularisation limit come from the tail end of stellar formation, because their eccentricities matched the eccentricity distribution from stellar binaries. Ribas and Miralda-Escudé (2007), on the other hand, argued that the there are indeed, two populations of objects, but the dichotomy occurs in mass. The low mass objects ($M_p \lesssim 4\ M_j$) form via standard accretion of gas onto a solid core made from ice and rock from the protoplanetary disk, whereas the heavier objects ($M_p \gtrsim 4\ M_j$) are the tail end of star-formation, having been formed from direct fragmentation and collapse of the gas cloud that gave rise to the system. Core-accretion planets would form with initially circular orbits, and would have to acquire their measured eccentricities later on in their lives. The heavier objects would have to be formed beyond ~ 30 AU, and then they would migrate inwards, acquiring their large eccentricities from the migration process. This scenario would cleverly explain the brown-dwarf desert by positing that the brown dwarfs would struggle to migrate by the same mechanism because of their heavier mass. The low mass objects would also have an upper limit set by the material in the protoplanetary disk, whereas the high mass objects would have a lower mass limit due to the fragmentation process.

Ford and Rasio (2008) cautioned against this choice of $M_p = 4\ M_j$, which was based on a marginal correlation between planet mass and stellar metallicity. Ford and Rasio (2008) then argued that a larger sample of planets having a host star with and without a binary companion would be needed to test this hypothesis. On the other hand, Wright et al. (2009) find that high mass planets

$M \sin i > 1\ M_j$ have a broad distribution of eccentricities within $0 < e < 0.5$, but low mass planets have a distribution that shows a peak near $e = 0$. More recent work by Raymond, Armitage, and Gorelick (2010) also confirms that the observed eccentricity distribution matches the isolated planet-planet scattering scenario, and the mass dependence is easily explained if the masses of the two objects have similar masses.

As described in Section 1.9, we use an updated sample of systems in this study, and we find that the eccentricity distribution of the more massive planets are not surprising when we consider all the planets and the tides in the star and the planet.

1.6.2 Semi-major axis distribution

In addition to reproducing the observed eccentricity distributions, several of the works described in the two previous sections also find support for the dynamical scattering scenario by reproducing short period objects, with semi-major axes consistent with observations. Raymond et al. (2009) looked at simulated three planet systems, with initial mass distributions consistent with observations. They found that after planet-planet scattering and the ejection of one planet, the two remaining planets remain on shorter period orbits, and are closely packed (i.e. within one or two Hill radii). This is consistent with observed multi-planet systems, which are found to be closely packed (see references in Raymond et al., 2009).

A useful constraint on the semi-major axis distribution has been suggested from the observation of multi-planet systems in resonances (Marcy et al., 2008). A strong candidate mechanism for producing such mean motion resonances (MMRs) is the gas disk migration scenario, where the planets migrate in a convergent fashion to enter the resonance (Kley, Peitz, and Bryden, 2004; Lee and Peale, 2002; Snellgrove, Papaloizou, and Nelson, 2001). On the other hand, Raymond, Armitage, and Gorelick (2010) showed that planet-planet scattering can also naturally explain resonant systems, and in addition, could also populate higher order resonances than disk migration can (see section 4.2 in Raymond, Armitage, and Gorelick, 2010). Future observations of resonant systems could help confirm this.

1.6.3 Obliquity distribution

The protoplanetary disk is expected to be aligned with the equator of the protostar, i.e. perpendicular to the spin of the star (Lissauer, 1993; Stapelfeldt et al., 1998). In that case, the obliquity of the stellar spin with respect to the orbital angular momentum would be zero. Interestingly, the different migration scenarios make very clear predictions on the resultant distribution of obliquities. For example, the disk migration scenario as outlined by Lin, Bodenheimer, and Richardson (1996) is expected to preserve any initial obliquity, whether it is zero or otherwise. Further, Lubow and Ogilvie (2001) find that the obliquity actually decays in that scenario, and Cresswell et al. (2007) find similar results. The planet-planet scattering scenario, on the other hand, predicts that the inclinations will be non-zero (Chatterjee et al., 2008; Jurić and Tremaine, 2008; Raymond, Armitage, and Gorelick, 2010). In the presence of a third body with

the right mass and orbit in the system, the Kozai mechanism can further increase the stellar obliquity (see Section 1.7).

If we could measure the obliquity of a sample of planetary systems, we could confront these theories with observations. Unfortunately, the best we can do is to obtain the sky-projected spin-orbit angle (λ) for transiting planets, via the Rossiter-McLaughlin effect (McLaughlin, 1924; Rossiter, 1924, see also Section 3.1.2 for a more detailed description of the Rossiter-McLaughlin effect). Essentially, a planet transiting across the face of a rotating star will cover part of the surface, and depending on the viewing and orbital geometry, can cause an anomaly in the spectral lines of the starlight. The first projected spin-orbit angle was measured by Queloz et al. (2000), who found that the rotation of the star HD 209458 was aligned with the orbit of the planet HD 209458b. In the following years, many similarly aligned objects were found, pushing the community to cautiously lean towards the disk migration model.

Unexpectedly, in 2008, Hébrard et al. (2008) found that the orbital plane of the planet XO-3b was misaligned with respect to the spin of the host star, with $\lambda = 70 \pm 15^\circ$. Since that time, numerous objects with a significant misalignment have been found, including objects on retrograde orbits (Triaud et al., 2010; Winn et al., 2009a). This was not easily explained by disk migration scenarios. The planet-planet scattering scenario, on the other hand, does produce objects with significant misalignments.

Indeed, Jurić and Tremaine (2008) used N-body numerical simulations to find that strong dynamical interactions can have a large impact on the orbital inclinations of planets migrating in this way. Up to about 10% of their simulations showed objects with large inclinations ($\gtrsim 50^\circ$) after the scattering process. Similar work by Chatterjee et al. (2008) obtained comparable results, and showed that an object moving to an orbit with short pericenter tends to acquire a higher inclinations, up to about 60° (See Chatterjee et al., 2008, Figure 9). Raymond, Armitage, and Gorelick (2010) found that inclinations $0^\circ \lesssim i \lesssim 15^\circ$ were quite common in most simulations, but just as in the case of eccentricity, equal mass systems produced the largest pumping up of orbital inclination, up to about $\sim 80^\circ$ (see Raymond, Armitage, and Gorelick, 2010, fig 10). Again, similarly to the eccentricity case, Raymond, Armitage, and Gorelick (2010) found that simulations including a planetesimal disk resulted in smaller inclinations than simulations without disks, but this effect is most prominent for low-mass planets. Of course, this does not explain all the obliquities measured to date: for example, the objects with much larger obliquities, including the retrograde orbits, need some other mechanism to explain them. We cover this question in Section 1.7.

As the evidence was mounting for a whole population of misaligned systems, Winn et al. (2010) pointed out an intriguing trend: hotter exoplanet host stars tend to have a higher obliquity. Albrecht et al. (2012) added more than a dozen new Rossiter-McLaughlin (RM) measurements (See Section 3.1.2) and further confirmed the trend. Since the RM effect can only measure the sky-projected angle, Schlaufman (2010) used a different method involving photometry and the projected rotational velocity of the stars, to obtain the component of the obliquity along the line of sight to 10 systems. Again, he found higher obliquities for hotter stars.

The scenario that Winn et al. (2010) propose is that the migration of all (or most of) the known hot Jupiters occur via planet-planet scattering (and possibly Kozai interactions), which leads to high obliquities. The reason that hotter stars

seem to have misaligned spins whereas cooler stars are aligned, is that the former retain their obliquities, whereas the latter lose it through tidal interactions. Indeed, Winn et al. (2010) identified a limit at T=6250 K, where the two populations seem to diverge. For stars with T<6250 K, a significant amount of the star's outer envelope is convective. This allows the star to undergo tidal dissipation via turbulent dissipation (see Section 2.2 For hot stars with T>6250K, the mass of the convective zone has shrunk to the extent that turbulent dissipation is ineffective, leaving the objects with a high obliquity. Hansen (2012) used a more theoretical approach and lacked the newer RM measurements of Albrecht et al. (2012), but still agreed qualitatively with the Winn et al. (2010) result.

1.6.4 Gravitational microlensing constraints

In addition to the eccentricity and inclination distributions, another observational constraint that could have supported the gravitational scattering scenario is a measurement of the number of free floating planets in the Galactic volume where we have found planetary systems. Unfortunately, using gravitational microlensing survey observations, Sumi et al. (2011) find that the abundance of free floating planets is about twice the number of main-sequence stars ($1.8^{+1.7}_{-0.8}$). Veras and Raymond (2012) estimated that this leads to the number of planets ejected per unstable planetary systems to be about $n_{eject} = 2 - 50$. The wide range accounts for uncertainties in the estimates of the number of stars with giant planets, and the number of such systems that become unstable. Using numerical N-body simulations, Veras and Raymond (2012) argue that even the lower limit, $n_{eject} = 2$, is implausibly large. Instead, they show that n_{eject} should be smaller than 1 for gravitational scattering, and the ratio of free-floating planets to stars should be close to one. If gravitational scattering is not enough to account for the measured value, then other mechanisms must be invoked, such as dynamical interactions in multiple star systems, or external effects such as disruption from passing stars or Galactic tides.

1.7 Kozai mechanism

As mentionned in Section 1.6.3, the planet-planet scattering model on its own, only appears to produce obliquities of up to about 60°. Because of the sky-projected nature of the measured misalignment angle λ, a large value of λ means that the obliquity ψ is large, but a small value of λ does not constrain the obliquity ψ to be small (Fabrycky and Winn, 2009). Thus, λ is a lower limit on the obliquity. Still, many objects (e.g. XO-3, Hébrard et al. (2008), HD 80606, Pont et al. (2009), etc.) have large values of projected spin-orbit angle, and thus have large obliquities, including retrograde orbits.

Kozai (1962) studied the influence of Jupiter's orbit on the highly inclined and eccentric orbits of asteroids. Similarly, Lidov (1962) studied the effect of the moon on the orbit of near-Earth artificial satellites. This mechanism is now known as the Kozai-Lidov mechanism, or simply the Kozai mechanism. Essentially, the Kozai mechanism requires three objects in a hierarchical triple, i.e. with an inner binary and an outer companion orbiting the inner binary (Eggleton and Kisseleva-Eggleton, 2006). If the orbital plane of the outer companion is inclined at $39.2° < i < 140.8°$ as compared to the inner orbit, secular interactions

due to weak perturbations from the distant third body (Fabrycky and Tremaine, 2007) can lead to large oscillations in eccentricity and inclination of the inner orbit. As long as the outer period is less than about 100 years, even a brown dwarf or a giant planet can lead to large amplitude Kozai cycles over $\sim$ 10Myr (Eggleton and Kisseleva-Eggleton, 2006), without necessarily showing up on a radial velocity measurement compaign at present-day precisions.

Mazeh, Krymolowski, and Rosenfeld (1997) first suggested that the high eccentricity ($e = 0.63 \pm 0.08$, Cochran et al., 1997) of the planet 16 Cygni Bb may be due to the Kozai effect. They used numerical simulations to study three body systems, and suggested that the distant companion 16 Cygni A, could be causing a modulation of the eccentricity of the planet, provided the orbital planes of the inner and outer binaries are separated by about 60°. Holman, Touma, and Tremaine (1997) obtained similar results, and pointed out the accompanying variation in inclination for the inner binary. Kiseleva, Eggleton, and Mikkola (1998) studied the Kozai mechanism in stellar triple systems, but included the effects of tidal friction. The Kozai mechanism causes the eccentricity to oscillate between extremes, and the pericenter distance can decrease dramatically to the point that tidal dissipation can reduce the eccentricity at a shorter semi-major axis. Observationally, Tokovinin et al. (2006) found that the period distributions for isolated stellar binaries and inner binaries in triple systems were different. This could mean that the inner binaries in the triple systems start with a similar period distribution to isolated binaries, but the Kozai mechanism forces the inner binary to have a large eccentricity, leading to a short pericenter distance and thus the inner orbit can circularise at a shorter period. Kiseleva, Eggleton, and Mikkola (1998) speculated that the same effect may be responsible for the formation of close-in hot Jupiters. Wu and Murray (2003) studied this possibility for the planet HD 80606b, which is on a highly eccentric orbit ($e = 0.933 \pm 0.001$, Naef et al. 2001). They showed how the Kozai mechanism, combined with tidal dissipation, can cause the planet to migrate inwards, after formation.

Zucker and Mazeh (2002) found that short-period, massive planets ($P < 100$ d, $M_p > 2M_j$) are more likely to be found in stellar binary systems. Desidera and Barbieri (2007) showed that the Kozai mechanism and tidal friction can operate in these systems where the stellar binary companions are close enough ($a \lesssim 300$ AU). Malmberg, Davies, and Chambers (2007) noted that the Kozai system can also lead to planet-planet scattering, when the secular evolution of one object brings it close to another. This can then lead to consequences described in Section 1.6.

Fabrycky and Tremaine (2007) extended the works of Holman, Touma, and Tremaine (1997) and Kiseleva, Eggleton, and Mikkola (1998), to look at Kozai cycles due to a distant companion in stellar triples, and include tidal friction. They also apply their results to hot Jupiters, and concluded that at most, a modest fraction of hot Jupiters could have been formed by the Kozai mechanism and tidal friction. This conclusion, however, was based on a handful of observations, and the more recent sample of exoplanets with a measured spin-orbit angle includes many objects with large obliquities, including retrograde objects. In fact, Fabrycky and Tremaine (2007) did point out that the Kozai mechanism with tidal friction yielded a population of objects where the minimum pericenter reached is equal to the Roche limit. The subsequent orbital circularisation by tidal interactions with the host star then cause the final semi-major axis to be twice the Roche limit, due to the conservation of angular momentum. This is consistent

with the results of Faber, Rasio, and Willems (2005) and Ford and Rasio (2006).

Nagasawa, Ida, and Bessho (2008) extended the numerical works of Rasio and Ford (1996) by following the orbital evolution of systems with three Jupiter-mass planets, allowing for the Kozai mechanism to operate. In contrast to previous work (Fabrycky and Tremaine, 2007; Holman, Touma, and Tremaine, 1997; Holman and Wiegert, 1999; Malmberg, Davies, and Chambers, 2007; Marzari et al., 2005) which consider Kozai interaction from stellar mass companions, Nagasawa, Ida, and Bessho (2008) use outer planets for the same purpose. They follow the setup of Marzari and Weidenschilling (2002), but include tidal damping of the orbital energy using the dynamical tide formulation of Ivanov and Papaloizou (2004) (See Section 2.4. During the chaotic stage of the system evolution, tidal damping can only circularise the orbit if the pericenter distance is small enough ($\lesssim$ 0.02-0.04 AU). Generally, the probability of such a large eccentricity (0.98-1.0) after scattering is quite low. Thus, the tidal circularisation process is too slow to form circular hot Jupiters in more than about 10% of cases (Chatterjee et al., 2008; Marzari and Weidenschilling, 2002; Weidenschilling and Marzari, 1996). On the other hand, even if the inner planet is isolated from the outer ones and safe from chaotic gravitational scattering, it can still undergo Kozai cycles on a secular timescale. Indeed, it may go through several Kozai cycles, by building up the eccentricity on a secular timescale, interacting with the outer planets repeatedly, and entering subsequent Kozai cycles with lower angular momentum each time. The later Kozai cycles can then achieve eccentricities close enough to unity that tidal circularisation can then operate on the inner orbit. In contrast to the previous studies that only considered the first stable state, Nagasawa, Ida, and Bessho (2008) find that the probability of forming hot Jupiters rises to 30% over the next few million years when the secular interactions are considered.

Retrograde orbits

Most of the early work on the Kozai migration scenario followed the quadrupole approximation of the gravitational potential, using a stellar mass perturber (Fabrycky and Tremaine, 2007; Mazeh, Krymolowski, and Rosenfeld, 1997; Wu and Murray, 2003). Unfortunately, the underlying assumption, that the inner planet's angular momentum component parallel to the total angular momentum is constant, restricts the formation of retrograde orbits with respect to the total angular momentum (Naoz et al., 2011). On the other hand, Ford, Kozinsky, and Rasio (2000) showed that with planetary perturbers, this component does not need to be constant.

Naoz et al. (2011) used the octupole approximation using Hamiltonian perturbation theory, and showed that the angular momentun component parallel to the total angular momentum can even change sign, producing a retrograde orbit (see their Figure 1. for a dramatic demonstration of a high obliquity excursion). The octupole-order evolution equations are appropriate to study closely coupled orbits involving planetary perturbers. In addition, these equations allow the Kozai cycles to be quasi-periodic, and an arbitrarily high eccentricity can be achieved, leading to a shorter pericenter distance (Ford, Kozinsky, and Rasio, 2000; Naoz et al., 2011). Thus, the Kozai effect at octupole order, coupled with tidal interactions, can form misaligned hot Jupiters on short period orbits in a two planet system within one hundred million years.

Disruption of the Kozai mechanism

Despite the success of the Kozai scenario in producing misaligned hot Jupiters with short periods, the Kozai mechanism can be disrupted in a number of cases where the apsidal motion produced by the third body is in competition with apsidal motion induced by general relativity, quadrupolar distortion of the inner binary due to their own rotation, or quadrupolar distortion of the inner binary due to each other (Eggleton and Kisseleva-Eggleton, 2006; Malmberg, Davies, and Chambers, 2007; Nagasawa, Ida, and Bessho, 2008).

1.8 Confusion: Are tides not enough?

It was clear in the early days of exoplanet science, that irrespective of the migration mechanism (Sections 1.4 –1.7), tidal interactions between the host star and the close-in hot Jupiters would be important (Lin, Bodenheimer, and Richardson, 1996; Rasio et al., 1996; Rasio and Ford, 1996). The strong tidal effects should increase sharply with decreasing period and these orbits are thus expected to circularise on a timescale much smaller than the system age. A higher tendency for such circular orbits is indeed observed in the sample of transiting planets (biased towards detection of short-period objects), as compared to those from RV surveys. This has been interpreted as a signature for tidal circularisation. The transition from eccentric orbits to circular orbits at short period has also been seen in binary star systems (e.g. Mathieu and Mazeh, 1988 and see references in section 8 of Mazeh, 2008). Indeed, if we consider a short period hot Jupiter system to be a tidally interacting binary with a tiny mass ratio, we expect the orbit to be circularised, aligned and synchronised with the stellar rotation (Hut, 1980) within a fraction of the system lifetime.

The strength of tidal interactions depends on the dissipation mechanism inside the star or the planet. Pont (2009) plotted $a/(R_p R_*)^{1/2}$ (representative of the system scale, and by proxy, the orbital period) against M_p/M_* (the mass ratio, which influences tidal interactions). If tidal effects exerted a major influence on final orbital configuration of the transiting planet systems, we would expect objects with small system scale to have eccentricities compatible with zero. Indeed, Pont (2009) found this expected trend in the then-known sample of transiting exoplanets, with heavy objects on long period eccentric orbits, and very short-period orbits that were circular.

Unfortunately, over the next few years, the picture got more complicated, as several objects were apparently found to have eccentric orbits at very short periods. In Figure 1.1, we have plotted an update of Figure 2 from Pont (2009). From the top panel, it is clear that there are many objects on eccentric orbits at very short period, which undermines the role of tidal interactions in the final orbital evolution of these exoplanets. The clear distinction between circular orbits and eccentric orbits as noted by Pont (2009) is now gone. In particular, the objects WASP-12b (Hebb et al., 2009) and WASP-14b (Joshi et al., 2009) were very puzzling cases.

WASP-12b orbits very close to its host star ($P = 1.09$ d), even by the standard of hot Jupiters. Moreover, WASP-12b has an inflated radius ($R = 1.8\ R_j$); one of the most extreme examples of anomalous radii for hot Jupiters. As a result, the planet fills its Roche lobe (Fossati et al., 2010b; Haswell et al., 2012; Li et al., 2010). With such a short orbital distance, and large size, a gas giant planet is

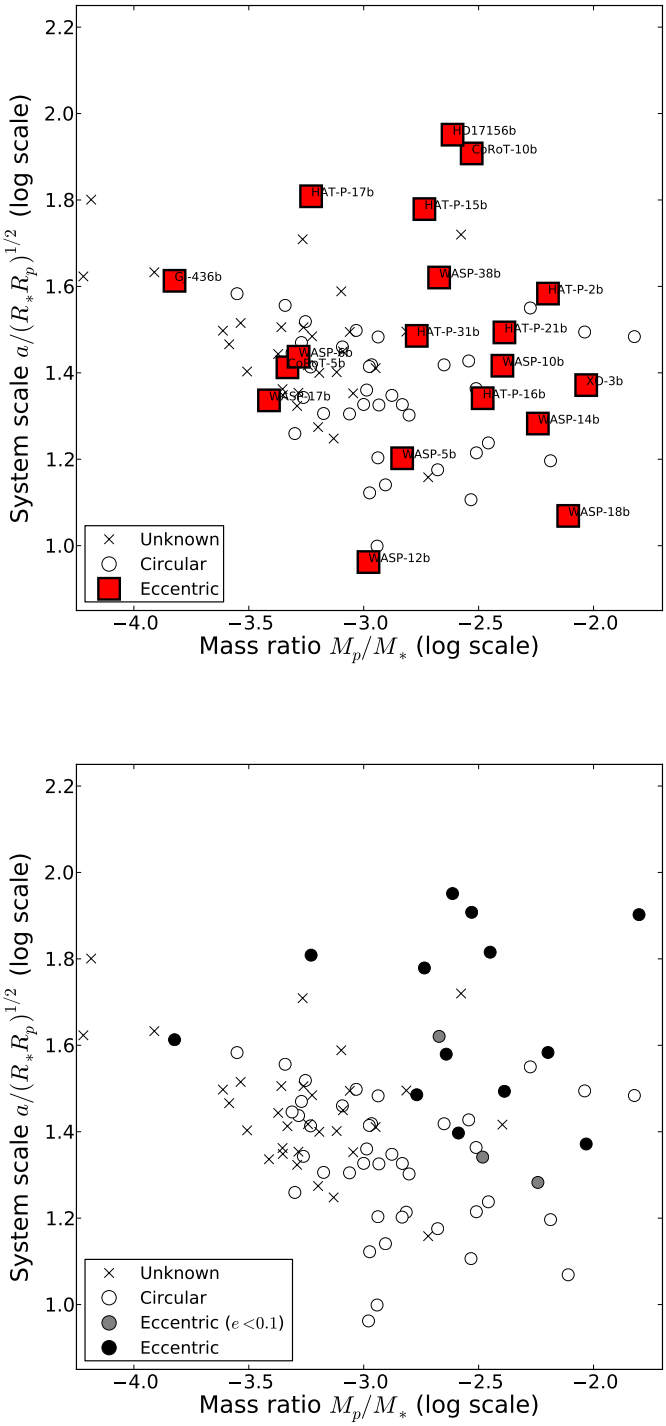

Figure 1.1: **Top:** Updated version of Figure 2 from Pont (2009). The squares represent objects on eccentric orbits, from the literature before this study. **Bottom:** Same plot as the one on the left, but taking into account the results of this study, that there is no evidence for eccentricity in CoRoT-5b, WASP-5b, WASP-6b, WASP-10b, WASP-12b, WASP-17b and WASP-18b. The crosses in both panels represent objects with unknown eccentricities.

expected to undergo complete orbital synchronization and circularization on a short time-scale ($\sim$ 100,000 years, see Section 6.2). Indeed, most planets orbiting closer than 0.05 AU are observed to have circular orbits. However, (Hebb et al., 2009) determined a value of $e = 0.049 \pm 0.015$, a 2.8 σ significant departure from circularity (based upon the Lucy and Sweeney, 1971, test). López-Morales et al. (2010) measured the secondary eclipse of WASP-12b from the ground with SPI-Cam on the ARC Telescope at Apache Point Observatory in the z' band. Their best-fitting result initially indicated an secondary eclipse with a significant time lag ($e \cos \omega = 0.0156 \pm 0.0035$) compared to the epoch expected for a circular orbit, with a similar level of significance to H09. This would have made the planet by far the subject of the strongest tidal dissipation in any known planetary system at the time – by a factor of about 400, as compared to WASP-14b (see Section 4.5). This is because of the short circularization time-scale and the reportedly significant eccentricity.

WASP-14b is, after WASP-12b, the known transiting planet having a reported non-circular orbit (Joshi et al., 2009, $e = 0.091 \pm 0.003$)) with the second-shortest period (P = 2.2 d). This makes it another test case for tidal evolution of close-in gas giants. If its orbital eccentricity is indeed near 0.1, then this non-zero but relatively low value – in the context of the distribution of giant exoplanet eccentricities – makes it likely that this planet has undergone some degree of orbital evolution, and is still subject to strong tidal forces at present. Therefore its presence may be useful to constrain the tidal synchronization timescale. It is also an important object when studying the issue of the anomalous radius of hot Jupiters because of its inflated size ($Rp = 1.28\ R_j$). WASP-14b occupies a distinctive position in the relevant parameter space: irradiation, orbital distance, eccentricity and size.

In addition to WASP-12 and WASP-14b, other particularly interesting objects were CoRoT-5b, WASP-5b, WASP-6b, WASP-10b, WASP-17b and WASP-18b. Rauer et al. (2009) derived a value of eccentricity $e = 0.09^{+0.09}_{-0.04}$ for CoRoT-5b, a 0.46 M_j planet on a 4.03 day orbit. WASP-5b is a 1.6 M_j planet on a 1.63 day orbit and was first reported by Anderson et al. (2008). Gillon et al. (2009) used z-band transit photometry from the VLT to refine the eccentricity of WASP-5b to $e = 0.038^{+0.026}_{-0.018}$, and these authors made a tentative claim for the detection of a small eccentricity. Gillon et al. (2009), derived an eccentricity $e = 0.054^{+0.018}_{-0.015}$ for WASP-6b, a 0.50 M_j planet on a 3.36 day orbit. Christian et al. (2009) reported that the 2.96 M_j planet WASP-10b had an orbital eccentricity of $e = 0.059^{+0.014}_{-0.004}$, with a period of 3.09 days. In the case of WASP-17b, a 0.49 M_j planet on a 3.7 d orbit, Anderson et al. (2010) preferred a model with $e = 0.129^{+0.106}_{-0.068}$. WASP-18b, a 10.3 M_j planet on a 0.94 d orbit, was found to have an eccentricity of $e = 0.0092 \pm 0.0028$ by Hellier et al. (2009).

At this point, it looked like the tides mechanism was either not strong enough to explain the eccentricities of short period exoplanets, or some mechanism was keeping a non-zero eccentricity in those systems. For example, Ribas et al. (2009) concluded that the eccentric orbit of the transiting hot Neptune GJ-436b (Butler et al., 2004, $e = 0.12 \pm 0.06$) could be explained by an additional low-mass planet in the system, that would pump up the eccentricity via secular interactions. In the case of WASP-12b, Li et al. (2010) found that the alleged eccentric orbit would imply a huge amount of tidal energy dissipation in the planet, leading to a large mass-loss and causing the inflated radius. In that case again, the eccentricity would need to be pumped up by some other means, for example a hypothetical

resonant super-Earth. Based on such examples, Ibgui, Burrows, and Spiegel (2010) simply assumed that the planets WASP-4b, WASP-6b, WASP-12b, WASP-15b, and TrES-4b had non-zero eccentricities, and concluded that continuous tidal dissipation could produce the large radii. On the other hand, Beerer et al. (2011) found that the inflated planet WASP-4b cannot be explained by tidal inflation alone, given that the eccentricity component $e\cos\omega$=0.0024 at the 2-σ level. Thus, different objects would need to have different inflation mechanisms, because tidal inflation due to residual eccentricity is not always plausible.

1.9 Updated observational constraints

The present time is significant in the study of exoplanets, because a number of high quality measurements are now available for the three main observable effects of tides: circularization, synchronization and spin-orbit alignment. In this study, we used 158 new radial velocity observations of the known transiting exoplanet systems for 6 objects with the HARPS spectrograph and 6 objects with the SOPHIE spectrograph (see Section 3.1.3 for more details). We carried out a literature survey and collected radial velocity measurements for 54 transiting planets, as well as other relevant data such as the orbital periods and the time of mid-transit. Where available, we also used the secondary eclipse constraint on the eccentricity component $e\cos\omega$ from published photometric studies.

Given the rapid rate of announcement of new transiting exoplanets, we had to stop the clock somewhere, and we picked the 1st of July 2010. We selected only objects that had been reported in peer-reviewed journals or on the online preprint archive ArXiV.org. Moreover, we selected systems with well measured parameters (planetary radius R_p and mass M_p to within 10%) and excluded faint objects ($V > 15$). At that time, 64 such systems were known. We reanalyse the existing radial velocity data for 54 transiting systems, providing additional radial velocity measurements for 12 out of these 64 systems, and include information on 10 out of these 64 systems without further reanalysis of orbital ephemeris. These systems are listed in Table 5.1. In Section 5.7, we include a further 30 systems, most of which had been discovered in the mean time.

In addition to the reanalysis of RV measurements with photometric constraints, we also introduce two modifications to the Markov Chain Monte Carlo (MCMC) process commonly used by teams analysing RV data to work out the orbital parameters of transiting exoplanets. This involves a new treatment of the correlated noise present in most RV data sets, as well as analysing the data in model selection mode to check if an eccentric orbit is indeed justified, given the additional complexity of the eccentric version of a Keplerian orbit (see Section 3.3 for more the details of our analysis). The results of this study are encouraging: it would appear that the confusing picture sketched in Section 1.8 was misleading.

The presence of residual correlated noise is apparent in the López-Morales et al. (2010) data (see Figure 4.3) for WASP-12b, as expected for ground-based photometry at such a high accuracy — the depth of the secondary eclipse is only about 0.08$\pm$0.02 per cent. A space-based measurement of the WASP-12b secondary eclipse with the Spitzer Space Telescope (Campo et al., 2011) unambiguously showed that the timing of the secondary eclipse was consistent with a circular orbit. This result suggested that the López-Morales et al. (2010) time lag was probably due to instrumental systematics, and that the orbit of WASP-12b

is probably circular. A highly fine-tuned orbital alignment would be required to reconcile the Spitzer result with the ground-based measurement of the eccentricity. Following this, López-Morales et al. (2010) have reanalysed their data and revised their estimate to $e\cos\omega = 0.016 \pm 0.011$, an eccentricity with a much lower significance.

Our own results (Husnoo et al., 2011), with the help of the new radial velocity measurements, confirm the strong indications of Campo et al. (2011), that all the available data for WASP-12b is compatible with a circular orbit, and that the eccentricity of the best-fitting orbit to the radial velocity of Hebb et al. (2009) and subsequently the secondary eclipse data of López-Morales et al. (2010) may be due to correlated noise. Not accounting for this noise in the statistical analysis could lead to an apparent 3-σ significance for the rejection of the null hypothesis ($e = 0$), but the new data strongly suggest that the orbit of WASP-12b is indeed circular. A circular orbit for WASP-12b removes the need for models to explain the survival of such an eccentricity at this very short period, in face of what would have been extremely strong tidal effects. In particular, the scenario of Li et al. (2010), using the eccentricity from H09 to infer values of mass-loss and tidal dissipation for WASP-12b, loses its principal empirical support.

It is interesting to note that there is an inherent bias in eccentricity measurements from radial velocities, because a Keplerian orbit cannot get more circular than $e = 0$. Any noise applied to a circular orbit will result in an eccentric best-fitting orbit. Underestimating the noise will lead to spurious detections of small eccentricities. This was already recognised in the context of stellar binaries by Lucy and Sweeney (1971). These authors showed that spurious eccentricity detections tended to dominate for $e < 0.1$ for a typical precision at that time and stellar binary amplitudes. Four decades later, both companion masses and RV accuracies having changed by about three orders of magnitudes, and the same issue resurfaces for exoplanets. In the same way, Laughlin et al. (2005) showed that the measured orbital eccentricity of HD 209458b, $e = 0.014 \pm 0.009$ was consistent with the results of simulated data for a circular orbit. Shen and Turner (2008) also performed an extensive analysis involving simulated data to show that the estimation of eccentricities for exoplanets in the literature may be overestimated in about 10 per cent of cases. Recently, Zakamska, Pan, and Ford (2010) studied this effect in the Butler et al. (2006) catalogue of radial velocity planets.

In this study (Husnoo et al., 2012; Pont et al., 2011), we find that another six planets that were previously believed to have eccentric orbits, actually have observed orbital eccentricities that are compatible with zero. For example, WASP-10 is a transiting planet closer than 0.04 AU, with an orbit that was previously believed to be eccentric. Christian et al. (2009) found an eccentricity of $e = 0.059^{+0.014}_{-0.004}$, which is at a similar level of significance as the Hebb et al. (2009) result for WASP-12. Maciejewski et al. (2011) revisited this system and concluded that it was important to take stellar activity into account when using the original radial velocity measurements to compute the orbital eccentricity. This led these authors to conclude the orbit of WASP-10 was probably circular. In our own study, we also conclude that the original detection of a non-zero eccentricity was probably spurious (see Section 5.3). Similarly, we find that the orbital eccentricities of CoRoT-5b, WASP-5b, WASP-6b, WASP-17b and WASP-18b were overestimated, and the adoption of an eccentric orbit for these objects is not justified by the available observational data.

In contrast, we confirm the eccentricity of HAT-P-16b, $e = 0.034 \pm 0.003$, the smallest eccentricity that is reliably measured so far for an exoplanet as well as that of WASP-14b, which is the planet at the shortest period ($P = 2.24$ d), with a confirmed eccentricity, $e = 0.088 \pm 0.003$. The latter illustrates the capacity of SOPHIE to measure accurate values of orbital eccentricity for transiting planets, given a sufficient number of measurements well distributed in phase and spread over different nights (the measurements for WASP-12 having most weight towards an eccentric solution were gathered during only two different nights).

Our results are shown in the bottom panel of Figure 1.1. We have plotted an updated version of Figure 2 from Pont (2009), with empty circles representing circular orbits, filled circles representing eccentric orbits, and grey circles representing orbits caught in the process of circularisation. The picture is now a lot clearer compared to the one in the top panel of Figure 1.1, where several short-period orbits are unexpectedly eccentric.

The eccentricity distribution at short period has a crucial importance for any theory of planetary formation and orbital evolution. Planets on orbits that are consistent with circular gather in a well- defined region of the mass-period plane, close to the minimum period for any given mass (Husnoo et al., 2012; Pont et al., 2011). In this study, we find that there are no exceptions to this pattern. As an ensemble, the totality of transiting planets considered in this study is in agreement with classical tide theory, with orbital circularisation due to tides raised on the planet by the star and tides on the star raised by the planet, to varying degree depending on the position of the planet-star system in the mass-period plane.

Further constraints on migration

In addition to the eccentricity, the obliquity of the planetary system (see Section 6.4) and the rotation rate of the star (see Section 6.3) can also inform us about the formation history. In this study, we perform an analysis of all the available eccentricity, spin-orbit, and stellar rotation period measurements available for transiting exoplanets, and we conclude that gravitational scattering, coupled with the Kozai mechanism and tidal interactions are the most likely scenario to explain the migration of hot Jupiters. We consider the spin-orbit measurements from Triaud et al. (2010) and Albrecht et al. (2012), and we essentially confirm the results of Winn et al. (2010), as explained in Section 6.4 We find that our results are compatible with tidal theory, and that there is no need for perturbing stellar or planetary companions to excite non-negligible eccentricities in short period orbits.

Conclusion

In this chapter we have described the broad questions addressed in this thesis. Essentially, hot Jupiters as found close to their stars, couldn't have formed in their current locations, because the volatile materials evaporate and condense beyond the iceline. A migration mechanism must be invoked to explain their positions, and the two major lines of thought on this matter involve either tidal interactions with a protoplanetary disk, or dynamical interactions between two

or more giant planets followed by tidal interactions with the host star.

We will look at the theory of tides (Chapter 2), going over the different mechanisms for tidal interactions. In Chapter 3, we consider how the measurements used in this study are made, and we describe our analysis procedures. We look at the results on an object-by-object basis in Chapters 4 and 5. This is followed in Chapter 6 by a global analysis of the ensemble of information on transiting exoplanets, including the new measurements available in the literature since this study was originally published. We conclude that a dynamical history followed by tidal circularisation, alignment and synchronisation is the scenario that is the most consistent with observations.

Chapter 2

Theories of tidal interactions

In this chapter, we look at the different types of tidal interaction that could occur in a hot Jupiter system. The strength of tidal dissipation is dependent on the mass of the objects, the separation distance, and their internal compositions. In addition, entirely different tidal forcing and dissipation mechanisms can operate in different regimes. We first describe the equilibrium tide, and focus on the particular case of the weak friction model. We then briefly consider the dynamical tide, including the gravity and inertial modes, as well as their dissipation mechanism.

2.1 Tidal influence

Classical philosophers linked the oceanic tides on Earth with the motion of the moon (Van Der Waerden, 1987). Seminal work by G. Darwin (Darwin, 1879, 1890) put the equilibrium tide model (Section 2.3) for the Earth-Moon system on a firm mathematical footing. Later work showed evidence of tidal interactions in the other Solar System planets and moons (Peale, Cassen, and Reynolds, 1979), binary stars (Jeans; 1929), and galaxies (Ostriker, Spitzer, and Chevalier, 1972).

Since the term *tidal forcing frequency* σ will be used a lot in this chapter, let us describe what it means. This frequency depends on which tide is involved: the semi-diurnal tide ($\sigma = 2|\omega_p - n|$, where ω_p is the planet rotation rate, and n is the orbital mean motion), or the eccentric annual tide ($\sigma = n$). When the planet is not synchronised, the semi-diurnal tide can dominate, and when the planet is synchronised, the annual tide dominates. In the intermediate regime, there is a rich spectrum of tidal frequencies that excite tidal interactions, leading to tidal dissipation.

2.2 The equilibrium tide

Tidal effects arise when an extended body is found in a non-uniform gravitational field. For example, if we have a heavy planet on a short period orbit (e.g. CoRoT-3b, 21.7 M_j, $P_{orb} = 4.26$ d) around a star, the gravitational field of the planet across the star varies significantly and this non-uniform potential causes a distortion in the star (see for example Mazeh and Faigler, 2010). The star is no longer just spheroidal (from fast rotation, $P^*_{rot} \approx 4$ d), but additionally takes the shape of an ellipsoid with three unequal axes. This is called the equilibrium tide, because the star is assumed to be in hydrostatic equilibrium (Zahn, 2005).

It is an intuitive idea: the non-uniform gravitational potential due to the planet and the centrifugal force cause two bulges on the star (Figure 2.1). As the planet moves along its orbit, the equilibrium tide follows the planet. If the star were an ideal fluid with zero viscosity, it would adjust instantaneously to the tidal perturbation. In reality, the star is not an ideal fluid, so there will be some viscosity (for example, turbulent viscosity — see Zahn, 1977) that delays the arrival of the tide. If the planet orbits more slowly than the stellar rotation, the tidal bulge on the star that is closest to the planet will lead the planet, whereas if the planet orbits faster than the stellar rotation, the closest tidal bulge will trail behind the planet. Similarly, the star's gravitational potential can cause equilibrium tides on the planet, which work in a similar way.

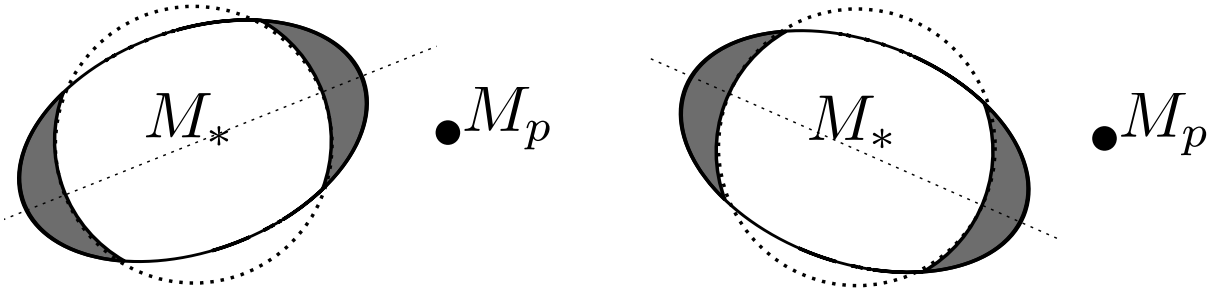

Figure 2.1: In each case, the stellar rotation and orbits are anti-clockwise. **Left:** The star rotates faster than the planet's orbit ($\Omega_* > n$) and the bulge due to the equilibrium tide leads the planet. **Right:** The planet orbits faster than the stellar rotation ($n > \Omega_*$) and the bulge lags behind the planet.

For tides on the planet, the delay in the arrival of the tidal bulge causes the dissipation of energy inside the planet. This dissipation of energy without a transfer of angular momentum causes the planet's orbit to become less eccentric (Goldreich and Soter, 1966). For tides on the star, the tidal bulges interact with the orbit, and cause both the dissipation of orbital energy, and the transfer of angular momentum between the orbit and the spin of the star. The mechanism for dissipation inside the two bodies (star and planet) is uncertain. For example, Darwin (1879) assumed some kind of unspecified friction in the fluid flow inside a planet, and Zahn (1975) considered turbulent viscosity in the convective envelopes of low mass stars.

Given the uncertainties in the dissipation mechanism, it is convenient to parametrise this dissipation in terms of some bulk dissipation rate, often represented by the tidal quality factor Q. A higher Q means lower a dissipation rate, while a lower Q means a higher dissipation rate. This Q value is typically estimated by physically modelling the energy stored and eventually dissipated in the bulge. Usually, mixing length theory provides a way to guesstimate the viscosity, which is then coupled with an assumption for the frequency dependence (Zahn, 1977, Zahn, 1989, etc. See Hansen, 2012 for a review).

Another approach is to consider constraints from the orbital evolution of the spin and orbital survival of satellites (Goldreich and Soter, 1966) or planets (Hebb et al., 2010). Essentially, this allows one to place a lower limit on the value of Q: if the Q were smaller than a given value, the dissipation rate would have been so strong that the object's orbit would have decayed, and the object would have been destroyed. In general, the bulk dissipation constant would depend on

the tidal excitation frequency σ, as well as the internal composition and structure of the object.

2.2.1 Constant ϵ and constant Q formulations

There are several formulations for the bulk dissipation rate in the literature. Darwin (1879, 1880) assumed that the fluid viscosity was responsible for the tidal dissipation, and split the perturbing tidal potential into a Fourier series which could then include the frequency-dependence of the viscosity. Adding these components together provides the bulk dissipation. In contrast, MacDonald (1964) assumed the dissipation mechanism to be frequency-independent, in which case the tidal quality factor Q was related to ϵ, the phase lag between the tidal potential maximum and the arrival of the bulge's maximum:

$$Q^{-1} = \tan 2\epsilon \tag{2.1}$$

In this case, the tidal quality factor Q was defined in terms of the peak energy E_* stored in the system during one tidal cycle, and the average rate of energy dissipation:

$$Q^{-1} = \frac{1}{2\pi E^*} \oint \frac{dE}{dt} dt \tag{2.2}$$

Goldreich (1963) follows this general approach, deriving equations for the tidal evolution of orbital elements to first order in eccentricity. Goldreich and Soter (1966) also followed the MacDonald (1964) approach, adopting a constant phase lag, which has the same restrictions on e and ψ. In the general case, the problem with this approach is that the phase lag ϵ, and hence the dissipation, does not decrease for vanishing frequencies. Instead, it switches to zero in a discontinuous manner when the tidal forcing frequency is zero. Similarly, it can swap to a negative value discontinuously when the direction of the tidal perturbation changes relative to the body. Another assumption in this approach is that the amplitude of each component is constant. These assumptions are only valid for the small eccentricities e and inclinations ψ that are observed in the Solar System, because the approximations only work if the tidal potential has a narrow range of frequencies (Greenberg, 2009).

Unfortunately, many influential studies have made heavy use of this constant-Q approach in regimes with $e > 0.2$. For example, Jackson, Greenberg, and Barnes (2008a) acknowledge that the Goldreich and Soter (1966) formulation is only valid for small e and ψ, which means higher order corrections are needed for the larger eccentricities that the exoplanets they consider would have had in the past. Yet, they integrate the equations of Goldreich and Soter (1966) backwards in time, to estimate the original orbital elements of these systems before tidal interactions started. Unfortunately, as Leconte et al. (2010) explained, the higher order terms are critical to the study of the high eccentricity regime, and including these terms produces qualitatively different outcomes because the energy dissipation is otherwise underestimated by several orders of magnitude.

Jackson, Greenberg, and Barnes (2008a) justify their choice of approximation with the fact that their approach was conservative. This made sense in 2008, when they were trying to show that tidal interactions had been important — models with the higher order terms would produce an even greater amount of dissipation, and simply confirm their results. Unfortunately, this justification fails when we consider that the largest change in eccentricity occurs early in

the system history, and therefore integrating the truncated equations backwards would not lead back to the starting position. Indeed, Jackson, Greenberg, and Barnes (2008b) went on to use this approach to study the effects of the tidal heating from eccentricity damping, and concluded that the inflated hot Jupiters could have derived their extra heating from tides in recent times. As Leconte et al. (2010) showed, this is dubious, because a consistent calculation of the radius and tidal evolution of the inflated hot Jupiters shows that the heating would have occurred too early in their history to maintain their present-day inflated radii.

Another study that uses the same approach for the Fourier decomposition and constant Q approach is that of Ferraz-Mello, Rodríguez, and Hussmann (2008). On the other hand, this approach is probably acceptable in cases of small eccentricity (Bodenheimer, Laughlin, and Lin, 2003; Bodenheimer, Lin, and Mardling, 2001; Lin, Bodenheimer, and Richardson, 1996).

2.2.2 Constant Δt formulation

An alternative to the constant phase (or constant-Q) formulation is the one with constant time lag Δt. This was used by Darwin (1879) and Alexander (1973): the viscous dissipation is assumed to produce a constant time lag between the maximum of the perturbing potential at the surface of one body, and the arrival of the tidal bulge. This is an arbitrary but convenient approximation, based on an ideal viscoelastic body: in the absence of detailed knowledge about the viscoelastic properties of giant planets, the constant time lag approach allows one to compute the tidal evolution for all eccentricities, and the free parameter Δt is not dependent on the tidal frequency ($\sigma = 2|\omega_p - n|$ for semi-diurnal tides in a non-synchronous object on a circular orbit, and $\sigma = n$ for a pseudo-synchronous object on an eccentric orbit – see Leconte et al., 2010).

For an incompressible giant planet, the phase lag ϵ and the tidal quality factor Q are related by the following (Efroimsky and Williams, 2009, eqn 105)

$$\frac{1}{Q(\sigma)} = \frac{\tan\epsilon(\sigma)}{1 - \left(\frac{\pi}{2} - \epsilon(\sigma)\right)\tan\epsilon(\sigma)} \tag{2.3}$$

and for a perfect viscoelastic oscillator, ϵ is given by Greenberg (2009),

$$\tan\epsilon(\sigma) = \frac{\sigma}{\tau(\omega_0^2 - \sigma^2)} \tag{2.4}$$

where ω_0 is the natural frequency of the oscillator (≈ 30 min, estimated out from the free-fall time for a planet) and τ is a viscous damping timescale. In the limit of $\omega_0 >> \sigma$ (i.e. a realistic tidal period of several days), the phase lag becomes (Leconte et al., 2010)

$$\epsilon(\sigma) \approx \frac{\sigma}{\tau\omega_0^2} \equiv \sigma\Delta t \tag{2.5}$$

The constant Δt model is therefore equivalent to a body that has $Q^{-1}(\sigma) \approx \epsilon(\sigma) \propto \sigma$ (Greenberg, 2009; Leconte et al., 2010). The tidal evolution equations reproduced in Section 2.3 are exact for all eccentricities and obliquities, in the viscous dissipation approximation (Leconte et al., 2010). In contrast, the approaches using a constant ϵ or Q involve a Fourier decomposition of the forcing potential, followed by a phase lag corresponding to each tidal frequency. The constant Q

model corresponds to a truncation of the Equations 2.7 and 2.6 (see later). This is why that these approaches are limited to small eccentricities. In fact, Leconte et al. (2010) show that for a pseudo-synchronous planet, the truncated models can lead to a growth of the semi-major axis if $e \sim 0.21$, and a growth of the eccentricity for $e \sim 0.33$. In the full model, both a and e are seen to decrease with time (see Figure 1 of Leconte et al., 2010). We revisit the the weak friction model as applied to the equilibrium tide in the next section (Section 2.3).

2.2.3 Eggleton et al. formulation

Eggleton, Kiseleva, and Hut (1998) followed a slightly different route. Instead of immediately assuming that the lag time Δt is a constant, they considered the case where it is proportional to the quadrupolar tensor of the mass distribution in a frame that rotates with the star. With a few simplifying assumptions (such as an isotropic viscosity, a small but dominant quadrupolar tensor), they linearise the continuity equation for the flow inside the body, and show that this approach is similar to the constant time lag (constant Δt) approach. The resulting equations are valid to large eccentricity and obliquities, unlike the constant Q or constant phase approach. This formulation is preferred by many authors, such as Barker and Ogilvie (2009); Bolmont et al. (2012); Dobbs-Dixon et al. (2004); Fabrycky and Tremaine (2007); Hansen (2010, 2012), because it affords clearer physical insights on the dissipation of the equilibrium tide.

2.3 Equilibrium tide: the weak friction model

In this section, we focus on the theory of equilibrium tides, as described by Leconte et al. (2010), following Hut (1981). As shown in Figure 2.1, the tidal potential due to the planet causes the star to deform into an ellipsoid. The non-zero viscosity of the star causes the bulge to lead ($\Omega > n$), or lag behind the planet ($\Omega < n$). This viscous dissipation model of the equilibrium tide is suitable for describing tidal dissipation in planets, viscous dissipation does not appear to be relevant for stars. It does however, approximate turbulent dissipation, which occurs in the convective envelope of lighter stars (Hut, 1981). Even though the frequency-dependence of the tidal quality factor Q may be very different in objects without a convective envelope, or objects where the dynamical tide dominates, Ogilvie and Lin (2004) and Ogilvie and Lin (2007) show that the frequency-averaged quality factor can still be independent of frequency in the limit of small Ekman number (i.e. in cases where viscosity is negligible) as long as the ratio of the tidal frequency and the orbital motion $\sigma/n > 2$. Of course, the actual dissipation mechanism may be very different, such as radiative damping (Zahn, 1975), wave breaking (Barker and Ogilvie, 2010), etc.

2.3.1 Tidal bulges

The tidal bulges can be replaced by point two masses, each one being given by $\mu = \frac{1}{2} k_{2,*} M_p \left(\frac{R_*}{r}\right)^3$, where R_* is the stellar radius, and r represents the instantaneous distance between the star and planet centers. The star is then represented by a point mass $M_* - 2\mu$. Confusingly, Leconte et al. (2010) call $k_{2,*}$ the star's Love number of degree 2, whereas Hut (1981) called it the apsidal motion

constant of the primary, following from Lecar, Wheeler, and McKee (1976). In practise, the Love number $k_{2,*}$ is twice the apsidal motion constant (Ragozzine and Wolf, 2009), and in this study, we only ever use it in a factor $k_{2,*}\Delta t_*$ which is unknown by about two orders of magnitude (see for example Barker and Ogilvie 2009; Carone and Pätzold 2007; Hansen 2012, etc).

Physically, the Love number represents the ratio of the perturbation induced in the internal potential of the star, due to the tidal potential from the planet (Gavrilov and Zharkov, 1977). For a rigid body, this quantity would be zero. The Love number is a bulk physical characteristic that reflects the internal distribution of mass in a body, including the central condensation of a star or the presence/absence of a solid core in a planet (Ragozzine and Wolf, 2009). A liquid planet of uniform density would have a value of $k_2 = 3/2$ (Goldreich, 1963). A Sun-like star has a value of $k_{2,*} \approx 0.03$ whereas the value for Jupiter is $k_{2,J} \approx 0.49$ (Ragozzine and Wolf, 2009).

The gravitational force between the two bulges is ignored, because the corresponding quadrupole term in the expansion of the gravitational potential is negligible. Similarly, the theory can be applied to two deformable objects separately (so far, we have focussed on a deformable star and a point-like planet). In this case, we assume the tidal bulges on the two objects don't interact, and we can simply calculate the effects on rate of change of the orbital parameters by each body separately, and add them up.

2.3.2 Orbital and rotational evolution

The gravitational forces between each bulge on the deformable star and the perturbing planet are not the same, because of the different distances. This causes a torque to be exerted on the star by the planet (and vice-versa), allowing the system to exchange energy and angular momentum between the stellar rotation and the orbit (Hut, 1981). The average rate of energy and momentum exchange is worked out from the torque acting over a whole orbit, and divided by the period. Together, these give the rate of change of the eccentricity and semi-major axis ($\dot{e}$, $\dot{a}$). The change in orbital angular momentum causes a change in in e and a. The rate of change of the stellar rotation Ω_* can also be computed if we assume that the star-planet system conserves angular momentum. This would be the case if the angular momentum loss due to the stellar wind is neglected.

In addition to the orbital evolution due to the exchange of energy and angular momentum from the torque, the non-zero viscosity of the star causes a time lag in the arrival of the bulge. In this case, the perturbing force on the star is radial and does not cause an exchange of angular momentum, but it does cause orbital energy to be dissipated in the star. This contributes an extra term to the rate of change of the orbital parameters e and a.

The equations given by Hut (1981) were limited to small obliquities, but Leconte et al. (2010) extended them to arbitrary obliquities. We reproduce these equations here, because they are used in Chapter 6.

The evolution of the semi-major axis a is described by the differential equation

$$\frac{1}{a}\frac{\mathrm{d}a}{\mathrm{d}t} = \frac{4a}{GM_*M_p}\left\{K_p\left[N(e)x_p\frac{\omega_p}{n} - N_a(e)\right] + K_*\left[N(e)x_*\frac{\omega_*}{n} - N_a(e)\right]\right\} \quad (2.6)$$

where the terms $N(e)$, N_a are functions of the eccentricity e alone, and are defined later in this section. The two terms K_* and K_p represent the contributions

from dissipation in the star and planet respectively, and will also be described later on. The orbital frequency is given by $n = \frac{2\pi}{P_{orb}}$, where P_{orb} is the orbital period, while $\omega_* \frac{2\pi}{P_{rot,*}}$ and $\omega_p = \frac{2\pi}{P_{rot,p}}$ are the rotational angular frequency of the star and planet respectively. Similarly, $P_{rot,*}$ and $P_{rot,p}$ are the rotational periods of the star and planet respectively. The parameter x_* is the cosine of the stellar obliquity ε_*, and x_p is the cosine of the planetary obliquity ε_p relative to the total angular momentum plane. The evolution of the eccentricity e is given by

$$\frac{1}{e}\frac{\mathrm{d}e}{\mathrm{d}t} = \frac{11a}{GM_*M_p}\left\{K_p\left[\Omega_e(e)x_p\frac{\omega_p}{n} - \frac{18}{11}N_e(e)\right] + K_*\left[\Omega_e(e)x_*\frac{\omega_*}{n} - \frac{18}{11}N_e(e)\right]\right\} \tag{2.7}$$

and the functions $\Omega_e(e)$ and $N_e(e)$ will be defined later on. The evolution of the angular momentum of the star and planet are given by the following two equations

$$\frac{\mathrm{d}C_*\omega_*}{\mathrm{d}t} = -\frac{K_*}{n}\left[\left(1+x_*^2\right)\Omega(e)\frac{\omega_*}{n} - 2x_*N(e)\right] \tag{2.8}$$

$$\frac{\mathrm{d}C_p\omega_p}{\mathrm{d}t} = -\frac{K_p}{n}\left[\left(1+x_p^2\right)\Omega(e)\frac{\omega_p}{n} - 2x_pN(e)\right] \tag{2.9}$$

where the C_* and C_p are the principal moments of inertia of the star and planet respectively. The obliquities evolve as

$$\frac{\mathrm{d}\varepsilon_*}{\mathrm{d}t} = \sin\varepsilon_*\frac{K_*}{C_*\omega_*n}\left[(x_* - \eta_*)\Omega(e)\frac{\omega_*}{n} - 2N(e)\right] \tag{2.10}$$

$$\frac{\mathrm{d}\varepsilon_p}{\mathrm{d}t} = \sin\varepsilon_p\frac{K_p}{C_p\omega_pn}\left[(x_p - \eta_p)\Omega(e)\frac{\omega_p}{n} - 2N(e)\right] \tag{2.11}$$

where the functions $\Omega(e)$ and $N(e)$ are used as before. The parameter η is the ratio of rotational angular momentum to orbital angular momentum for each object:

$$\eta_* = \frac{M_p + M_*}{M_pM_*}\frac{C_*\omega_*}{a^2n\sqrt{1-e^2}} \tag{2.12}$$

$$\eta_* = \frac{M_p + M_*}{M_pM_*}\frac{C_p\omega_p}{a^2n\sqrt{1-e^2}} \tag{2.13}$$

The terms describing the strength of the dissipation stellar and planetary tides are given by

$$K_* = \frac{3}{2}k_{2,*}\Delta t_*\left(\frac{GM_*^2}{R_*}\right)\left(\frac{M_p}{M_*}\right)^2\left(\frac{R_*}{a}\right)^6 n^2 \tag{2.14}$$

$$K_p = \frac{3}{2}k_{2,p}\Delta t_p\left(\frac{GM_p^2}{R_p}\right)\left(\frac{M_*}{M_p}\right)^2\left(\frac{R_p}{a}\right)^6 n^2 \tag{2.15}$$

The ratio of the stellar term to the planetary term is

$$\frac{K_*}{K_p} = \frac{k_{2,*}\Delta t_*}{k_{2,p}\Delta t_p}\left(\frac{M_p}{M_*}\right)^2\left(\frac{R_*}{R_p}\right)^5 \tag{2.16}$$

which means the typical values of $\frac{k_{2,*}\Delta t_*}{k_{2,p}\Delta t_p} \sim 100$, $\left(\frac{M_p}{M_*}\right)^2 \sim (10^{-3})^2$ and $\left(\frac{R_*}{R_p}\right) \sim 10^5$ lead to a ratio of about 10. This means the stellar tide can dominate, unless the terms in the square brackets of Equations 2.6 and 2.7 have different orders of magnitude. We now list the parameters $N(e)$, $N_a(e)$, $N_e(e)$, $\Omega(e)$, $\Omega_e(e)$:

$$N(e) = \frac{1 + \frac{15}{2}e^2 + \frac{45}{8}e^4 + \frac{5}{16}e^6}{(1-e^2)^6} \tag{2.17}$$

$$N_a(e) = \frac{1 + \frac{31}{2}e^2 + \frac{255}{8}e^4 + \frac{185}{16}e^6 + \frac{25}{64}e^8}{(1-e^2)^{15/2}} \tag{2.18}$$

$$N_e(e) = \frac{1 + \frac{15}{4}e^2 + \frac{15}{8}e^4 + \frac{5}{64}e^6}{(1-e^2)^{13/2}} \tag{2.19}$$

$$\Omega(e) = \frac{1 + 3e^2 + \frac{3}{8}e^4}{(1-e^2)^{9/2}} \tag{2.20}$$

$$\Omega_e(e) = \frac{1 + \frac{3}{2}e^2 + \frac{1}{8}e^4}{(1-e^2)^5} \tag{2.21}$$

2.4 The dynamical tide

A star or planetary body can be considered as a 3D oscillator (Goldreich and Nicholson, 1989; Zahn, 1975). For example, when a planet on an eccentric orbit reaches periastron, the tidal potential perturbation is at a maximum, and can excite normal modes of oscillation in the host star. This means that orbital energy is converted into oscillations that can be then be damped to dissipate the energy. This process can occur at each periastron, and the energy is dissipated during the rest of the orbit. If all the energy of an encounter is dissipated during that time, the total energy of the orbit will keep decreasing on secular timescales, while the angular momentum is unchanged. This causes the orbit to circularise. On the other hand, if the damping is too slow, the newly excited modes from a more recent encounter can be out of phase with the previous encounter, and the overall response can be chaotic. If the orbit is circular, any deviation from synchronous rotation can still induce oscillations and this mechanism can still occur.

Three restoring forces can be involved in the propagation of these waves (Zahn, 2008):

- buoyancy due to gravity can produce *gravity modes* of oscillation
- the Coriolis force can produce *inertial modes* of oscillation, and
- the compressibility of the gas can produce *acoustic modes* of oscillation.

Collectively, these oscillations are called the dynamical tide.

2.4.1 Gravity modes

Observations of high mass binaries showed circular orbits at short period (Primini, Rappaport, and Joss, 1977), even though the extended radiative envelope of a high mass star is free of convective turbulence and thus cannot support turbulent dissipation of the equilibrium tide. Cowling (1941) considered the possibility of non-radial oscillations in a high mass polytropic star in a binary and Zahn (1970) extended this work to include realistic stars, with a convective core and a radiative envelope. Gravity modes can be excited close to the convective-radiative boundary, on the radiative side. At that point, the Brunt-Väisälä frequency (the frequency at which a parcel of a statically stable environment will oscillate if displaced vertically) becomes equal to the tidal forcing frequency, and the wavelength of the gravity modes are long enough to couple with the tidal potential (Goldreich and Nicholson, 1989). As the gravity wave undergoes only a weak radiative dissipation in the interior, it propagates to the stellar surface, where it dissipates in a thin layer, depositing angular momentum. The dissipation layer achieves a synchronised state first, and then acts as a barrier to outgoing waves, causing them to dissipate further inside. In this case, the star can become synchronised from the outside in. The dissipation by radiative damping was described by Zahn (1975).

Radiative damping would generally be more applicable to high mass stars, but Terquem et al. (1998) considered its relevance in the case of solar-type stars. They studied a close binary system where a solar-type star has a companion on a circular orbit, and was heavy enough to exert tidal forces on the host. The Coriolis force was ignored (i.e. non-rotating star), and they considered dissipation in the convective zone and the radiative by turbulent dissipation, and radiative damping respectively. They compared their results with the equilibrium tide limit, and found that this didn't work for a standard solar model. In fact, they found that the turbulent viscosity would have to be about 50 times larger than mixing-length theory would predict. Instead, they found that g-mode oscillations induced from inside the radiative core can extend into the outer convective region, where they are dissipated by turbulent viscosity. Strong dissipation can occur if the g-mode oscillations achieve a global resonance.

Another mechanism for the dissipation in solar-type stars was suggested by Goodman and Dickson (1998), who studied the effects of non-linear wave breaking. Essentially, if an internal gravity wave is excited at the interface between the radiative core and the convective envelope, it can propagate towards the center. These waves can reflect coherently, and thus feed into a global standing mode in the radiative zone (Barker and Ogilvie, 2010). If the tidal frequency matches such a global standing mode, efficient dissipation can only occur at that particular frequency , and thus the contribution to the overall dissipation rate is minimal. Indeed, because of the stellar spin-down, the system does not stay very long in any resonance, and simply moves on (Savonije and Witte, 2002). Only in special cases can resonance locking occur, and thus allow the contribution to be larger (Witte and Savonije, 1999).

If the amplitude and frequency of the tidal forcing are large enough, and the conditions at the center of the star are favourable (stable stratification of the core, which depends on stellar mass and main-sequence age, Ogilvie and Lin 2007), the waves can enter the non-linear regime, and be reflected with a perturbed phase, or simply be dissipated because wave breaking occurs (Goodman and Dickson, 1998). This means that the energy from the wave is rapidly and irre-

versibly transformed into turbulence, which then dissipates. In this case, we can have efficient dissipation over a continuous range of tidal frequencies. Barker and Ogilvie (2010) used a numerical model based on a non-rotating star and worked out that for a given orbital period P the effective tidal quality factor Q' would be given by

$$Q' \approx 1.5e5 \left(\frac{P}{1\ \mathrm{d}}\right)^{8/3} \tag{2.22}$$

for the Sun, and it varies by $\lesssim 5$ over the mass range 0.5–1.1 $\mathrm{M}_\odot$. The conditions for wave breaking and dissipation is

$$\left(\frac{\mathrm{M}_\odot}{M*}\right)\left(\frac{M_p}{\mathrm{M}_j}\right)\left(\frac{P}{1\ \mathrm{d}}\right)^{1/6} \gtrsim 3.3 \tag{2.23}$$

Because of the dependence on a radiative core, this mechanism is ineffective in a star with a convective core, eg: WASP-18, WASP-12, OGLE-TR-56.

In the planetary context, the convective nature (Guillot et al., 2004) of the interiors of hot Jupiters means that radiative damping cannot occur there. On the other hand, the stellar insolation can cause the surface layers of hot Jupiters to reach radiative equilibrium, and thus they could support radiative damping or non-linear damping as above, once g-mode oscillations are started above the convective region (Dobbs-Dixon et al., 2004).

2.4.2 Inertial modes

The natural frequency of oscillation of a star or gas planet due to the restoring force of gravity can be estimated from the free-fall time $2\pi/\omega_0 \approx \frac{1}{4}\sqrt{\frac{3\pi}{2G\bar{\rho}}}$, where G is the gravitational constant, and $\bar{\rho}$ is the mean density (Leconte et al., 2010) — this value is ∼30 minutes for the Sun and Jupiter. Ogilvie and Lin (2004) argued that this dynamical frequency can be much larger than the tidal forcing frequency: this allowed them to linearize the fluid dynamical problem of a slowly rotating planet. These objects are expected to be adiabatically stratified, because of efficient convection (Guillot et al., 2004), which can also carry inertial waves (i.e. the restoring force is the Coriolis force, instead of gravity). If the tidal forcing frequency matches some of these inertial modes, the tidal response can be enhanced (Papaloizou and Savonije, 1997). Ogilvie and Lin (2004) argue that the dissipation of inertial waves could be important in many cases of interest.

As Savonije, Papaloizou, and Alberts (1995) pointed out, the inertial modes occur in a dense or continuous spectrum in the absence of viscosity. The response of a star can then contain strong high frequency components. Inertial modes can also travel throughout the planet or star, unlike g-modes that are stopped by the convective envelope (Ogilvie and Lin, 2004). However, once a hot Jupiter's rotation is synchronised, tidal dissipation of inertial waves becomes less efficient (Ogilvie and Lin, 2004). For $n/\Omega > 2$, the dissipation would be inefficient, and would tend to be frequency-independent. Ogilvie and Lin (2007) extended the work of (Ogilvie and Lin, 2004) to solar-type stars. Again, they concluded that inertial waves could be important in these systems.

One intriguing scenario that involves inertial waves has been suggested by Lai (2012). Winn et al. (2010) had noted that the alignment of the stellar spin with the orbit in hot Jupiter systems with cool stars could post a problem if

the entire angular momentum of the planet is surrendered to align the star: the planet would be destroyed. To get around this problem, they suggested that the core and the envelope could decouple, and thus it would take a much smaller angular momentum exchange to align the stellar envelope. As Lai (2012) point out, this is a problem because the significant differential rotation of the fluid can lead to instabilities which would quickly couple the core and the envelope.

Instead, Lai (2012) worked out that if inertial waves in the star were relevant, there would be a component that is only permissible for misaligned systems. This component would work to align the system. Once the system is aligned, this component of the oscillations is forbidden, and therefore stops working. Thus, once alignment is attained, the radial decay due to that component becomes negligible. In this case, orbital decay and spin-orbit alignment no longer share the same dissipation quality factor, and instead have two different factors, and hence two different timescales. Alignment can happen on a shorter timescale than the current age of the system, and yet the tidal decay would take longer than the current age.

Conclusion

In this chapter, we have looked at several mechanisms for tidal dissipation and orbital evolution in hot Jupiter systems. We refer to the literature on the equilibrium tide in later chapters of this thesis. In the next chapter, we give an overview of the observations and the analysis techniques used in this study.

Chapter 3

Methods of observation and analysis

In this chapter, we look at the techniques involved in making the observations used in this study, and the subsequent analysis of these observations. In particular, we use radial velocity measurements, as well as transit photometry to constrain the orbital eccentricities of close-in exoplanets. These measurements are analysed in a Bayesian framework, and we include prior information from stellar evolution in the case of WASP-12. We include a treatment of correlated noise in the analysis, and use model selection to establish the nature of the orbit, eccentric or circular.

3.1 Radial velocity

3.1.1 Origin of the radial velocity signal

When two objects are bound by the gravitational force, they will orbit each other around their common center of mass. If the mass ratio is extreme, as is the case for a star-planet system, the center of mass resides inside the heavier object, in this case, inside the star. We can measure the radial motion of the star along the line of sight using Doppler spectroscopy (see next section), because the light from the star is red-shifted when it moves towards us and blue-shifted when it moves away. This radial velocity signal follows a conic section (Murray and Dermott, 1999), given by

$$V_r = K\left[\cos(\theta + \omega) + e\cos\omega\right] \tag{3.1}$$

where e is the orbital eccentricity, ω is the argument of periastron, and θ is the true anomaly. This latter variable is obtained as follows: the time variable t is converted to the mean anomaly M_a, which is then converted to an eccentric anomaly E_a, which is in turn converted into the true anomaly θ. The mean anomaly M_a is given by

$$M_a = \frac{2\pi}{P}(t - T) \tag{3.2}$$

where P is the period of the orbit, T is time of periastron and t is the time variable. The mean anomaly M_a is related to the eccentric anomaly E_a by Kepler's equation:

$$M_a = E_a - e\sin E_a \tag{3.3}$$

which must be solved numerically for E_a, and the true anomaly is obtained using the two equations

$$\cos\theta = \frac{\cos E_a - e}{1 - e\cos E_a} \tag{3.4}$$

and

$$\sin\theta = \frac{\sqrt{1-e^2}\sin E_a}{1 - e\cos E_a} \tag{3.5}$$

The semi-amplitude K of the radial velocity (Pater and Lissauer, 2001) signal is given by

$$K = \frac{2\pi G}{P_{orb}}^{1/3} \frac{M_p \sin i}{(M_* + M_p)^{2/3}} \frac{1}{\sqrt{1-e^2}} \tag{3.6}$$

where P_{orb} is the orbital period, M_p is the mass of the planet, and M_* is the mass of the star. The inclination i tells us how the orbit is oriented relative to the line of sight – in practise, it introduces a degeneracy $M_p \sin i$ whereby a light planet with an orbit aligned with the line of sight can give a radial velocity signal as large as that from a heavier planet with an inclined orbit w.r.t. the line of sight. This means that a radial velocity time series can only tell us the minimum mass $M_p \sin i$ of the planet, not its absolute mass M_p.

3.1.2 The Rossiter-McLaughlin effect

Our data for WASP-12 (but not the other objects) included an additional signal: the Rossiter-McLaughlin effect. Light from a rotating star will have a blue shifted component, corresponding to the part of the star rotating towards us, and a red-shifted component, corresponding to the part rotating away from us. When a planet transits across the face of the host star, this planet blocks some of the stellar light for some time. If the conditions are right (eg: the star rotates fast enough to produce a differential Doppler signal, but not so fast that it makes spectroscopic measurements difficult.), this can produce an additional Doppler signal superimposed on the orbital motion of the star (the smaller bump up and down in the middle of the phase curve for WASP-12 in the Figure **??**.) This signal is caused by the blocking of part of the red-shifted or blue-shifted light in turn. The exact shape of this additional signal can tell us the projected spin-orbit angle for the star-planet system. A system where the orbital plane is aligned with the stellar equator will produce a symmetrical signal, and a misaligned system will produce an asymmetrical or even inverted signal. A complication to this picture is that the stellar limbs are darkened, an effect due to the decrease in gas density as the planet moves from the center of the star to the edge. To model the radial velocity signature of the Rossiter-McLaughlin effect, we use the equations from Giménez (2006). This takes in the current orbital phase (calculated from time t, and orbital parameters), the projected rotational velocity of the star $v \sin i$, and the limb darkening parameters.

We use a quadratic limb darkening law, using two parameters u_1 and u_2. These are estimated from the Claret (2004a) database. We used the online tool *VizieR*(Claret, 2004b), and select Table 4, which lists the quadratic limb darkening coefficients (a, b). We narrow down the rows using the search facility, and we select the closest combination of ($\log g$, $T_{\rm eff}$ and $[M/H]$), picking the values for the g band.

3.1.3 Radial velocity measurements

Since 2008, our team had been collecting new radial velocity measurements for known transiting exoplanets as part of an on-going project (Hébrard et al., 2008; Mazeh et al., 2008), with a view to refine two orbital parameters that are critical in studying the orbital evolution of exoplanets: the eccentricity, and the sky-projected spin-orbit angle.

In this study, we used 158 new radial velocity measurements for 6 objects in the Northern hemisphere, and 6 objects in the Southern hemisphere (see Chapters 4 and 5, and Tables A.3, A.4, A.5, A.6, A.7, A.8, A.9, A.10, A.11, A.1, A.2 and A.12). These measurements were obtained with the SOPHIE spectrograph (Bouchy and The Sophie Team, 2006), mounted on the 1.93m telescope at the Haute Provence Observatory, and the HARPS spectrograph (Mayor et al., 2003), mounted on the 3.6m ESO telescope at La Silla, Chile. Both instruments have participated in the detection of numerous transiting exoplanets, notably the CoRot and WASP transit searches.

Each instrument is a fiber-fed echelle spectrograph, where two fibers bring light to the spectrograph: one fiber is fed from the telescope (Perruchot et al., 2008), and the other brings light from a comparison lamp (ThAr). SOPHIE, unlike HARPS, has two sets of fibers: one called high-resolution (HR), and one called high-efficiency (HE). For bright objects, the HR mode is used, and it can reaches a stability of a few m s^{-1}.

The HE mode lacks two components, a 40.5 μm slit that increases the spectral resolution, and a scrambler that is used to keep the illumination uniform despite changes due to guiding or atmospheric effects. This difference allows a higher throughput in HE mode than in HR mode, and allows the observation of fainter targets ($\sim$ 1 mag). Unfortunately, this mode is less optimised for precise radial velocity measurements. It turns out that the zero-point of the instrument could drift by a large amount (up to several dozens of m s^{-1} in some cases, see Figure 3.1) over several months. This effect is monitored and corrected for as part of the long term improvement of the SOPHIE correction pipeline (Bouchy et al., 2009a), but it is useful to keep this in mind, especially with older datasets that were collected before this issue was recognised.

From spectra to radial velocity

Each exposure from the instruments results in a CCD frame that is treated in the usual way for CCD astronomy: a correction is applied for bad pixels, a dark current frame is substracted and a flat-field correction is applied. The position of the diffraction orders are then obtained, and the spectrum is wavelength-calibrated. This is then cross-correlated with an appropriate synthetic spectrum, chosen from a library of synthetic spectra for stars of each spectral type observed. The resulting cross-correlation function (CCF) is then normalised and translated into the solar system barycenter frame of reference, and a Gaussian function is fitted. The mean of this Gaussian function gives the radial velocity, and the uncertainty in the radial velocity is computed from the width of the CCF as explained in a paper by Baranne et al. (1996).

3.2 Transit photometry

For the WASP-12 object, we fit not only the radial velocity, but also the transit photometry originally collected by the discovery team (Hebb et al., 2009). A transit occurs when a planet passes in front of the host star during its orbit. The probability of transit is low (Winn, 2010): roughly 0.005 for a star the size of the Sun, and a planet at 1 AU. This probability scales as R_*/a, causing a selection effect for close-in hot Jupiters. The detection of a hot Jupiter is also helped by the deeper transit signal, as compared to a smaller planet. We model the transit using the equations from Mandel and Agol (2002), using the quadratic limb darkening in the z-band for the WASP-12 transit photometry.

3.2.1 Secondary eclipse & eccentricity

When a transiting planet disappears behind the host star, this is called a secondary eclipse. In practise, the information in the transit and secondary eclipse light curves constrain the eccentricity in the following way (Winn and Holman, 2005):

$$e\cos\omega \simeq \frac{\pi}{2P}\left(t_2 - t_1 - \frac{P}{2}\right), \tag{3.7}$$

where $t_2 - t_1$ is the time difference between an secondary eclipse and a transit and P is the orbital period. The component $e\sin\omega$ is dependent on a ratio involving the durations of the secondary eclipse and transit,

$$e\sin\omega \simeq \frac{T_{\rm tra} - T_{\rm occ}}{T_{\rm tra} + T_{\rm occ}}, \tag{3.8}$$

where $T_{\rm tra}$ and $T_{\rm occ}$ are the transit and secondary eclipse durations respectively. The constraint on $e\cos\omega$ component of the orbital eccentricity is much stronger and can help to constrain the eccentricity of the planet (Campo et al., 2011; López-Morales et al., 2010).

When analysing the secondary eclipse photometry for WASP-12, we simply set the limb darkening to zero, and model the secondary eclipse using a scaled copy of the transit model. This scale parameter s can be converted to an secondary eclipse depth by multiplying it by the corresponding transit depth.

3.3 Bayesian analysis

We use our new RV measurements (Section 3.1.3), in addition to a compilation of existing RVs, as well as photometric constraints, from the literature (the orbital period P, the mid-transit time $T_{\rm tr}$, and $e\cos\omega$ where it is available from secondary eclipses), to derive updated estimations of the orbital parameters for the known transiting planets.

We follow a Bayesian approach in our analysis (see for example, Gregory, 2005). Firstly, we engage in parameter estimation to determine updated values for the orbital eccentricity e, and the mass of the planet (related to the semi-amplitude K, see equation 3.6). We do this by using a Markov Chain Monte Carlo (MCMC) integration (see Section 3.4), to produce best-fit values and a derived uncertainty for each parameter. Secondly, we run the MCMC twice,

once with a free eccentricity, and then with a fixed eccentricity $e = 0$, to model a circular orbit. We use the best fit models from this procedure to compare the two models, circular orbit versus eccentric orbit. This hypothesis testing step allows us to determine if the additional complexity of an eccentric orbit is justified by the data.

There are several major advantages to using a Bayesian approach in this context. Firstly, it allows us to derive combined constraints from radial velocity datasets and transit light curves (in the case of WASP-12). Secondly, it allows us to include various priors on parameters where available ($e \cos \omega$ is available for some transiting systems from the secondary eclipse). In the case of WASP-12, we can include a prior from stellar evolution models when modelling the light curve. Finally, the Bayesian approach provides a natural method to get rid of "nuisance parameters" (such as the angle of periastron ω), and provides the marginalised posterior distributions for the useful parameters (e.g. the eccentricity e, the semi-amplitude K, etc.)

3.4 Parameter estimation

We use a Markov Chain Monte Carlo (MCMC) code to fit the RV measurements (and transit light curve, in the case of WASP-12), and to derive updated values and uncertainties for the orbital parameters. The use of MCMC methods in this context has been described by many authors, including Holman et al. (2006). Our implementation is itself described by Pont et al. (2009). For each parameter, the MCMC produces a marginal posterior distribution.

In this case, we are using the MCMC for Bayesian parameter estimation. Let M_1 be the statement "The orbit of WASP-12 is circular." Further, let D be the statement "The N measurements D_1, D_2, ... D_N had values d_1, d_2, ... d_N at times t_1, t_2, ... t_N". Let the parameters X and Y represent the parameters of an orbit (in practise, there are four parameters for modelling a circular RV orbit, and six parameters for an eccentric orbit — here we use two to simplify this explanation). The Bayesian approach allows us to express all our knowledge of the parameters X and Y as the joint posterior distribution $p(X, Y|D, M_1, I)$, where the expression X, Y represents the logical conjunction operator "*and*", and the symbol $|$ means "given D and I", where I represents any prior information we have. In this case, the posterior distribution is given by Bayes' theorem,

$$p(X, Y|D, M_1, I) = \frac{p(D|X, Y, M_1, I) \times p(X, Y, M_1, I)}{p(D|M_1, I)} \tag{3.9}$$

The first term in the numerator on the RHS represents the likelihood function for this data D, as described further in the next section. The second term represents the joint prior for the parameters of interest. The term $p(D|M_1, I)$ represents the marginal likelihood, which acts as a normalisation constant in the parameter estimation problem. The posterior distribution is therefore proportional to the product of the likelihood and the prior. To determine the preferred value of parameter X, and the associated uncertainty, we wish to have the marginal posterior distribution $p(X|D, M_1, I)$, where the effects of parameter Y are taken into account. This is done by integrating the joint posterior distribution over all possible values of Y:

$$p(X|D, M_1, I) = \int_{y_{\min}}^{y_{\max}} p(X, Y|D, M_1, I) dY \tag{3.10}$$

In practise, this is a multi-dimensional integral, because of the large number of parameters. We use the MCMC method with the Metropolis-Hastings (Chib and Greenberg, 1995) algorithm, which provides a convenient albeit computationally intensive solution to this problem. The Markov Chain part of the MCMC refers to the fact that each entry in the chain depends on the one previous entry in a probabilistic fashion. After a number of steps, the chain loses memory of where it has been before, and simply samples the joint posterior distribution for the parameters. The MCMC procedure carries out this integration in the following fashion:

1. We start off with a set of "guessed" parameters X_0, Y_0, (in practise, we start off with literature values for known objects).

2. We calculate the "merit value" for this set of parameters. The merit function is the product of the likelihood and any *a priori* information we want to impose on the posterior distribution. This includes a component for correlated noise in the data, which we discuss in the next section.

3. We now take a jump in parameter space: for each parameter, we take the current value of the parameter and add a random number drawn from a normal distribution $\mathcal{N}(0, 1)$ (multiplied by a "scale" parameter, adjusted by hand to give an acceptance rate between 10% and 50% in step 6.

4. We calculate the "merit value" for this new set of parameters.

5. We compare the new merit value to the old merit value.

6. If the ratio is larger than unity, the new parameters provide a better fit to the data and we accept the jump: we store the values of the parameters in our MCMC chain.

7. If the ratio is less than unity, it indicated the new set of parameters are worse than the one before. We draw a random number from a uniform distribution, and we keep the new set of non-optimal parameters if the ratio of the new and old merit is larger than the number we just drew. If not, we keep the old set of parameters, and reject the new set.

8. We go back to step 3, and repeat this for a large number of times (eg: 400,000–800,000 steps).

In step 7, keeping a set of parameters that don't improve the solution allows the chain to explore parameter space in a random walk, and allows us to escape a local maximum in the k-dimensional merit surface, where k is the number of parameters. The actual likelihood function used in the analysis is described later in Section 3.8.

3.5 Correlated noise

Random Gaussian noise will, by definition, add a positive or negative contribution to a RV measurement with equal probability. In practise, RV measurements for faint objects ($V \gtrsim 12$ mag) can be contaminated with non-Gaussian sources of noise in the data (such as instrumental systematics and stellar variability). As shown in Figure 3.1, this can reach several dozen meters per second over several months. In a single night, this can be as much as several meters per second. This means that a each RV in a series of measurements taken in one single night will be offset by a similar amount due to the correlated noise, in addition to any astrophysical signal and Gaussian noise present. If we use a diagonal matrix for the uncertainties when analysing the data, we risk over-counting the RVs affected by this correlated noise. This can lead to an underestimation of the uncertainties in the final system parameters by a large factor (Pont, Zucker, and Queloz, 2006)

One shortcut that is commonly used (e.g. the M.I.T. team lead by Josh Winn, Winn et al. 2006, and our own team in the past Pont, Zucker, and Queloz 2006; Pont et al. 2009) is to add an extra term (in quadrature) to the instrumental uncertainty. This extra term is often called "*red noise*" and is given by $\sqrt{N}\sigma_r$, where the σ_r represents the magnitude of the red noise, and N is the number of measurements that were taken together (and thus suspected to have been offset in a similar manner). We used this approach in the study of WASP-12 (Husnoo et al., 2011).

When we move on to the large sample of objects described in Chapter 5, this technique presents a difficulty: the correlations may last for more than one night, and it becomes difficult to decide what value of N to use: should a single measurement at the end of a night be counted as part of the next set of measurement early the following night? In this study, we use a slightly different technique, based on a correlation timescale.

The fitting statistic χ^2 is usually defined by

$$\chi^2 = \sum_i^N \left(\frac{v_{o,i} - v_{m,i}}{\sigma_i} \right)^2 \tag{3.11}$$

where $v_{o,i}$ is the observed RV at time t_i and $v_{m,i}$ is the RV predicted by the model. The quantity σ_i is the instrumental uncertainty, and may include the red noise term above added in quadrature. This definition of χ^2 is equivalent (Sivia, 2006) to the inner product $(\mathbf{F} - \mathbf{D})^{\mathrm{T}} \mathbf{C}^{-1} (\mathbf{F} - \mathbf{D})$, where $\mathbf{F}$ and $\mathbf{D}$ are the model and observed RV time series expressed as a column vector, and $\mathbf{C}$ is a covariance matrix with elements

$$C_{k,k'} = \begin{cases} \sigma_i^2 & \text{for } i = i' \\ 0 & \text{otherwise,} \end{cases} \tag{3.12}$$

The covariance matrix is a square matrix, with N diagonal elements representing the formal uncertainties on the measurements. The non-diagonal elements are zero. If the measurements are not independent, we need to include a term for correlated noise in the non-diagonal elements:

$$C_{i,i'} = \delta_{i,i'} \sigma_i^2 + \sum_{k=1}^{M} \sigma_k^2 \exp - \frac{(t_i - t_{i'})^2}{2\tau_k^2} \tag{3.13}$$

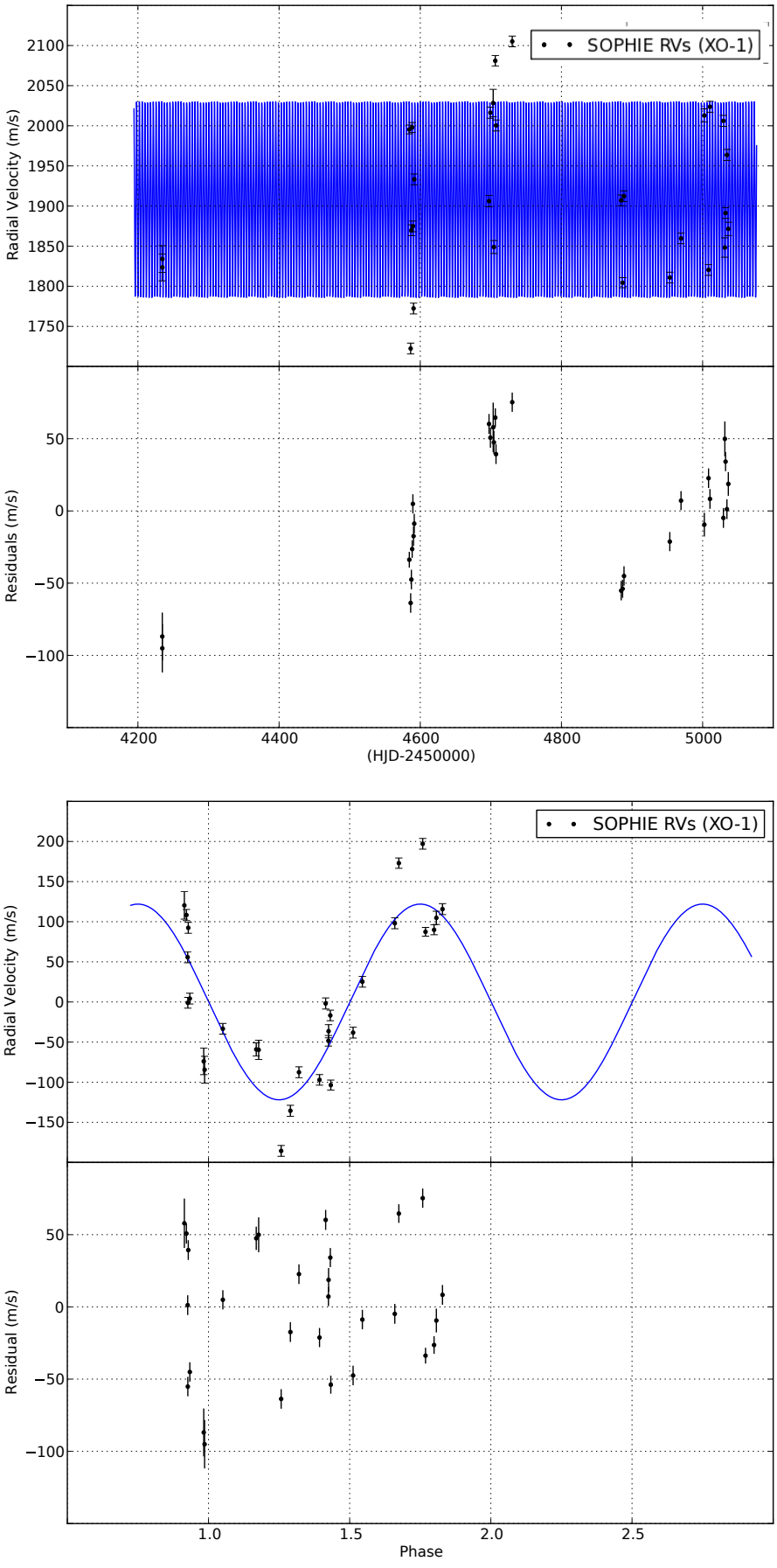

Figure 3.1: Instrumental drift over several months (SOPHIE measurements of XO-1). The solid line represents a circular orbit. An eccentric orbit doesn't improve the fit appreciably. Note: we were unable to correct for this drift in a consistent manner and thus decided against using the XO-1 dataset.

where the index i represents each RV, and the index k is summed over M terms representing correlation at M different timescales. The term $\exp -\frac{(t_i - t_{i'})^2}{2\tau_i^2}$ is called a squared exponential stationary covariance kernel. The stationary part of the name means the covariance matrix does not change during the MCMC integration. The parameter σ_k here represents the red noise associated with a timescale τ_k.

It is difficult to estimate the values of τ_k and σ_k. In principle, we should assign a prior probability over a large range of values for each parameter, and marginalise over these nuisance parameters. In practise, RV datasets suffer from incomplete orbital coverage, sparse sampling, and large uncertainties. Our prior experience (Pont et al., 2009) suggests that correlations over several hours to about a day are the most important, so we elect to choose a single correlated noise term, setting $M = 1$. The corresponding parameters for this term are then labelled τ_r and σ_r. For datasets where the reduced χ^2 for a given model (circular or eccentric) was larger than unity, we estimated σ_r by repeating the MCMC analysis with different values of σ_r until the best-fitting orbit resulted in a reduced χ^2 of unity for some optimal value of σ_r. For the correlation timescale, we used $\tau_r = 1.5$ d in most cases, as described in more detail in Section 5.2.

3.6 Stellar prior

When we fit the transit light curve for WASP-12, we need a value for the system scale a/R_*, where a is the semi-major axis and R_* is the stellar radius and we also need the scaled planet radius R_p/R_*. R_p/R_* is constrained by the transit depth, and a/R_* is constrained by the transit duration and the ingress duration, and this constrains the stellar density (Winn, 2010). We want to include all relevant prior information in this analysis, and stellar models can provide a prior on the connection between stellar mass, radius and effective temperature $T_{\rm eff}$, while spectroscopic analysis can provide a constraint on the effective temperature. For WASP-12, we use $T_{\rm eff} = 6300^{+200}_{-100}$ K from Hebb et al. and we include the stellar model prior in the following fashion.

Girardi et al. (2002) from the Italian group working in Padova, Italy, assembled a database of stellar models in 2002, providing theoretical isochrones. This table is available in electronic format online, and Aparicio and Gallart (2004) interpolated this database in the metallicity and age grid. Pont and Eyer (2004) resampled this database so that the probability density of models is proportional to the proportion of stars with a given mass and age as seen for a random population of stars in the Galactic disk. Various assumptions go into this procedure, such as the initial mass function of the Galaxy, and the uniform age distribution used. This probability resampled grid was used in the PhD thesis of Alapini-Odunlade (2010), who sorted the grid by density, and labelled the entries for stellar density, mass, radius and effective temperature with an integer index k. In this work, we use the index k for our MCMC jumps, meaning we sample the stellar prior with the correct probability for stellar density. This avoids the problem with a simple jump in stellar density space, as that would assume the density of stars are uniformly distributed — they are not: most stars in the Galactic disk are low mass, and therefore high density stars. The extent of the grid is large enough to thoroughly cover the probability space for WASP-12: $M_* = [0.6, 10] M_\odot$, $R_* = [0.6, 455] R_\odot$ and $T_{\rm eff} = [2300, 26000]$ K. The prior infor-

mation is then imposed on the MCMC chain by penalising jumps that cause $T_{\rm eff}$ to fall outside the range allowed by the spectroscopic result by Hebb et al.

3.7 Other priors

As described in Section 3.2, the detection of a secondary eclipse can set a powerful constraint on the $e\cos\omega$ projection of the eccentricity. We use the model parameters $e\cos\omega$ and $e\sin\omega$ for computational efficiency (Ford, 2006). If we use e and ω, we are setting the desired flat priors on these parameters. Unfortunately, correlations between the two parameters can cause the MCMC to waste a lot of time attempting to make unfavourable jumps which are more likely to get rejected.

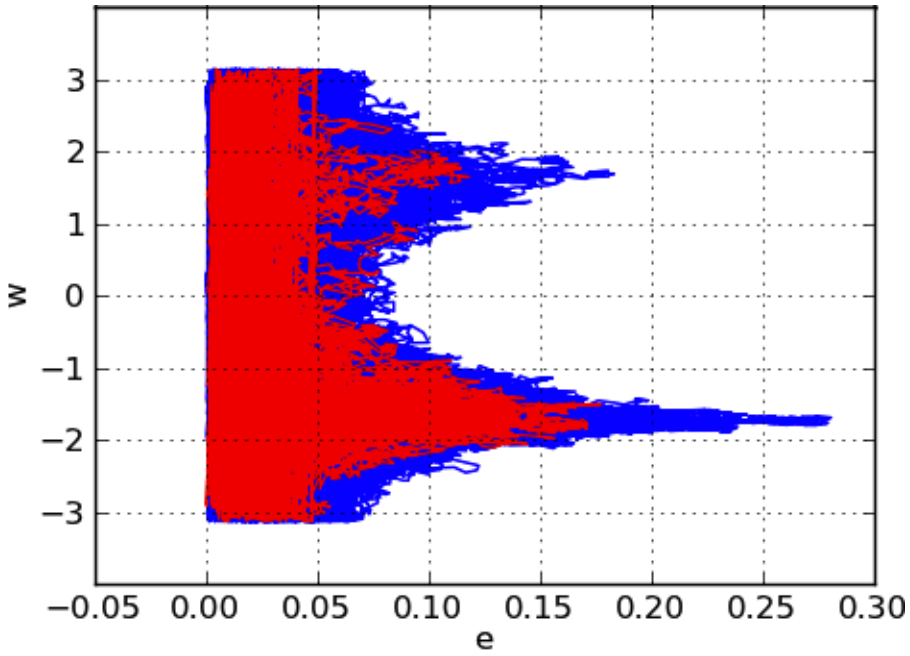

Figure 3.2: For correlated parameters, we need to use very small steps to sample the posterior distribution adequately; otherwise, many steps are rejected. Both cases lead to an inefficient algorithm.

We therefore set flat priors on $e\cos\omega$ and $e\sin\omega$, but this is something that we need to be careful about, because it means we have a linear prior $\propto e$ as explained by Ford (2006) and more recently by Eastman, Gaudi, and Agol (2013). In fact, in this study, it simply means that we will overestimate the upper limits on eccentricity for orbits that are consistent with circular, which leads to a conservative estimate of the upper limits. In the case of the eccentric orbits, the information contained in the data is so consistently compelling that the final estimate of the eccentricity e is independent of the actual prior on the eccentricity.

We also include an *a priori* constraint for the orbital period P and the mid-transit time $T_{\rm tr}$, which are well constrained by transit photometry. In the case of WASP-12 where we fit both the RV datasets and the photometry, we omit this constraint.

3.8 Merit function

From Sivia (2006), the likelihood function for some data sampled with a Gaussian distribution of errors is given by:

$$\mathrm{P}(\mathbf{D}|\theta, I) = \frac{\exp\left[-\frac{1}{2}(\mathbf{F}-\mathbf{D})^{\mathrm{T}}\mathbf{C}^{-1}(\mathbf{F}-\mathbf{D})\right]}{\sqrt{(2\pi)^{N}\det(\mathbf{C})}}, \tag{3.14}$$

where $\mathbf{D}$ is the radial velocity time series data expressed as a vector, θ is the vector of model parameters, $\mathbf{F}$ is the predicted values from the Keplerian model. The argument of the exponential is the χ^2 described in Section 3.5, which includes a component for correlated noise. The value returned by the merit function to the MCMC algorithm is this likelihood function, with which we multiply terms for the stellar prior in the case of WASP-12 (Section 3.6), the constraint on $e\cos\omega$ from secondary eclipse photometry where available and the constraints on the orbital period P and the mid-transit time T_{tr} (Section 3.7) from transit photometry. This general procedure is common in the literature (e.g. Winn et al., 2006).

3.9 Eccentricity bias

When radial velocity measurements are analysed to produce orbital parameters, it is common to leave the eccentricity e as a free parameter in the Keplerian orbit model (e.g. Gillon et al., 2009; Hebb et al., 2009; Rauer et al., 2009). This parameter is then constrained by the radial velocity measurements. Other authors (e.g. O'Donovan et al., 2007; Shporer et al., 2009) fix the eccentricity $e = 0$, using the argument that tidal effects should circularise the orbits of close-in planets. Yet others (e.g. Collier Cameron et al., 2007; Hellier et al., 2009; West et al., 2009) fix the eccentricity $e = 0$ because their radial velocity datasets do not provide adequate constraints on the parameter.

As pointed out by Lucy and Sweeney (1971) who studied binary stars, any observational noise in radial velocity measurements will always bias the derived eccentricity towards a higher value, even for circular orbits. This is because the eccentricity has a lower bound, and noise can only increase it. These authors showed that spurious eccentricity detections tended to dominate for $e < 0.1$ for a typical precision of the instruments at that time and for typical stellar binary radial velocity amplitudes. Four decades later, both companion masses and RV accuracies having changed by about three orders of magnitudes, so the issue resurfaces now in the field of exoplanets. The effect has been demonstrated for the exoplanet HD 209458 by Laughlin et al. (2005), where synthetic datasets for a circular orbit yielded a range of eccentricities consistent with the measured value of $e = 0.014$. The F-test suggested by Lucy & Sweeney is useful in this case, as it allows one to do hypothesis testing on the possibility that the circular orbit cannot be rejected. Some authors have taken this route (e.g. Anderson et al., 2011; Enoch et al., 2011). As explained by Anderson et al. (2012), if we use a non-zero eccentricity when analysing the transit light curve of a planet on a circular orbit, we can derive wrong estimates for the planet radius. Shen and Turner (2008) also performed an extensive analysis involving simulated data to show that the estimation of eccentricities for exoplanets in the literature may be overestimated in about 10% of cases. Recently, Zakamska, Pan, and Ford (2010) studied this effect in the Butler et al. (2006) catalog.

3.10 Model selection

In this study, the eccentricity distribution of the known transiting exoplanets plays a critical role. It is therefore important that we obtain reliable estimates of the eccentricities. Since any noise will yield a non-zero estimate for the value of the eccentricity e, we use Bayesian model selection to evaluate the evidence discriminating between a circular and eccentric orbit.

It is difficult to establish a prior odds ratio for the two models, so we set the priors to be equal (even though it is clear that circular orbits are more likely for close-in planets — see for example Wang and Ford 2011, who discussed planets discovered with radial velocity). By Bayes' theorem, the posterior odds ratio for the eccentric orbit compared to the circular orbit is

$$O_{e,c} = \frac{P(\text{eccentric}|\text{data})}{P(\text{circular}|\text{data})} = \frac{P(\text{data}|\text{eccentric})}{P(\text{data}|\text{circular})} \frac{P(\text{eccentric})}{P(\text{circular})}, \tag{3.15}$$

and we set the prior odds ratio to unity. Thus, the posterior odds ratio (the first term on the far RHS) is equal to the global likelihood ratio for the two models, also called Bayes' factor. The global likelihood ratio can be worked out from

$$P(\text{data}|\text{Model}_\text{j}) = \int_{\Theta_j} L(\Theta_j|\text{data}) \times P(\Theta_j|\text{Model}_\text{j}) d\Theta_j \tag{3.16}$$

where Θ_j represent the vector of parameters for each model j, $L(\Theta_j|\text{data})$ is the likelihood of the data given model M_j and $P(\Theta_j|\text{Model}_\text{j})$ is the joint prior distribution of the parameters. Assuming the likelihood function is Gaussian and strongly peaked, we can approximate this integral with a Laplace integral (Kass and Raftery, 1995), which gives the Bayesian Information Criterion (BIC):

$$\text{BIC} = -2 \ln L_\text{max} + k \ln N, \tag{3.17}$$

where N is the number of measurements, k is the number of parameters in the model used and L_max is the maximum likelihood obtained for each model. The maximum likelihood corresponds to the smallest value of χ^2 (as given in Section 3.5) and we obtain it directly from the MCMC for each model. If we replace L_max with the expression given by $\text{P}(\mathbf{D}|\theta, I)$ in Equation 3.14 above,

$$\text{BIC} = \chi^2_\text{min} + k \ln N + \ln \left((2\pi)^N |\mathbf{C}| \right), \tag{3.18}$$

where χ^2_min is the minimum value of χ^2 achieved by the model, N is the number of measurements, k is the number of parameters in the model, and $|\mathbf{C}|$ is the determinant of the correlation matrix given in Section 3.5 above.

The radial velocity data for a Keplerian orbit involves 6 free parameters: the period P, a reference time such as the mid-transit time T_tr, a semi-amplitude K, a mean velocity offset V_0, the argument of periastron ω and the eccentricity e (in practice, we use the two projected compoments $e\cos\omega$ and $e\sin\omega$ instead of e and ω, as explained in Section 3.7). In this study, we use the period P, mid-transit time T_tr and their corresponding uncertainties as *a priori* information. We thus count them as two additional measurements in the calculation of the BIC, while the number of free parameters in each model (circular or eccentric) is now decreased by two. In this case, a circular model would have 2 free parameters (V_0 and K), while an eccentric model would have 4 free parameters (V_0, K, e, and ω).

The term $k \ln N$ thus penalises a model with a larger number of parameters (for example, an eccentric orbit), and we seek the model with smallest BIC. For each object, we repeated the MCMC analysis using the optimal value for σ_r for a circular orbit and an eccentric orbit separately, at $\tau = 1.5$ d (see Section 5.2). We call these two families. For each family, we performed a fit with a circular model and an eccentric model. In most cases, the two families agreed on a circular model (indicated by "C" in Table 5.1) or an eccentric model (indicated by "E" if $e > 0.1$ in Table 5.1), indicating this with a smaller BIC_c or a smaller BIC_e respectively. If the two families favoured a circular (or eccentric) orbit, we give the parameters from the family using an optimal value of σ_r for the circular (or eccentric) orbit. In a number of such cases, however, the upper limits on the orbital eccentricity were larger than $e = 0.1$. We labelled these eccentricities as "poorly constrained" (indicated by "P" in Table 5.1). In a few cases, the small number of measurements or the quality of measurements (e.g. for faint targets, or low mass planets) meant the two families disagreed: the family using the optimal value of σ_r for a circular orbit gave a smaller value of BIC_c, favouring the circular orbit and the family using the optimal value of σ_r for an eccentric orbit gave a smaller value of BIC_e, favouring the eccentric orbit. We labelled these cases "poorly constrained" as well.

Comparison of the BIC with the F-test

The BIC comparison can be related to the F-test if one considers the critical value F^* where BIC_e, the BIC for an eccentric orbit, and BIC_c, the BIC for a circular orbit become equal. The level of significance would depend on both k and N. From Atukeren (2010),

$$F^* = \left(N^{\frac{k_e - k_c}{N}} - 1\right)\left(\frac{N - k_e}{k_e - k_c}\right) \tag{3.19}$$

where $k_e = 6$, $k_c = 4$ and N is the number of data points. Thus,

$$F^* = \left(N^{\frac{2}{N}} - 1\right)\left(\frac{N - 6}{2}\right) \tag{3.20}$$

and the circular hypothesis is favoured if $F < F^*$, (c.f. $\mathrm{BIC}_c < \mathrm{BIC}_e$). Following Lucy and Sweeney (1971), F is calculated from

$$F = \frac{N - 6}{2}\frac{\chi_c^2 - \chi_e^2}{\chi_e^2} \tag{3.21}$$

and the significance of a given comparison (eccentric versus circular) is probability of falsely rejecting the null hypothesis (circular orbit), i.e. a Type I error, is given by

$$p = \left(1 + \frac{F}{\beta}\right)^{-\beta} \tag{3.22}$$

where $\beta = \frac{1}{2}(N - 6)$. This is the probability of falsely rejecting the circular orbit, assuming it is true. A small value of p (say, $p < 0.05$) means we cannot reasonably maintain that the orbit is circular, and a large value of p means we cannot reasonably maintain the orbit is eccentric. Thus, the BIC comparison can be seen as an F-test with a variable threshold for the p-value: a larger number of measurements can provide stronger evidence, and therefore this must be included in the model selection procedure (Atukeren, 2010).

Conclusion

In this chapter, we have looked at the techniques involved in making the observations used in this study, and the techniques we used in the analysis of this data. In the next chapter, we look at the analysis in detail, and describe the interesting objects in this context.

Chapter 4

Analysis: WASP-12 and WASP-14

In this chapter, we look at the objects WASP-12 and WASP-14. Both are short period exoplanets, and in 2009, both had been reported to have orbits with small but significant eccentricities. Our work contributed to show that WASP-12b was in fact on a circular orbit, and we confirmed the eccentricity of WASP-14b, the shortest period object with a confirmed and appreciably eccentric orbit. These results, together with those from Chapter 5 are used in Chapter 6 to show that the sample of currently known exoplanets is consistent with a history involving dynamical interactions and tidal effects.

4.1 Short period but eccentric orbits

Transiting planets are an important source of information on the formation, structure and evolution of exoplanets. Both WASP-12b and WASP-14b are characterized by close-in but apparently eccentric orbits, and therefore represent potentially important systems to constrain the migration, tidal and thermal evolution of gas giant planets. We combine our radial-velocity data with previously published data and a realistic treatment of correlated noise to calculate updated constraints on the orbital eccentricities.

The companion of the 11.7th-magnitude star WASP-12 is a particularly interesting example (Hebb et al., 2009, hereafter H09). It orbits extremely close to its host star, even by the standards of the so-called "hot Jupiters", with a period of 1.09 days, corresponding to an orbital distance only 3 times the radius of its host star. Moreover, WASP-12b has an inflated radius, $R \simeq 1.8\,\mathrm{R_J}$; one of the most extreme examples of anomalous radii for hot Jupiters. As a result, the planet fills about half of its Roche lobe (Li et al., 2010).

With such a short orbital distance and large size, a gas giant planet is expected to undergo complete orbital synchronisation and circularisation on a short timescale (∼100,000 yrs, using Mazeh, 2008, and assuming $Q/k \sim 10^5$), much shorter than the age of the system (2 Gyr, H09, or 1.0–2.65 Gyr, Fossati et al. 2010a).

Indeed, most planets orbiting closer than 0.05 AU are observed to have circular orbits. However, H09 determined a value of $e = 0.049 \pm 0.015$ for the orbital eccentricity of WASP-12b, a 2.8-σ significant departure from circularity (based upon the Lucy & Sweeny, 1971, test). This would make the planet by far the subject of the strongest tidal dissipation in any known planetary system — by a factor of about 400, as compared to WASP-14b. This is because of the short circularisation timescale and the reportedly large eccentricity, as discussed later.

Li et al. (2010) studied the case of WASP-12 with that value of eccentricity, and found a large implied mass loss and dissipation of tidal energy in the planet.

The measured eccentricity is based on fitting a Keplerian orbital motion to the radial velocity measurements collected by H09 with the SOPHIE spectrometer (Bouchy et al., 2009b; Perruchot et al., 2008) together with transit photometry. It must be remembered, however, that WASP-12 and WASP-14, are near the faint end of the capacity of the 1.93-m telescope at OHP, and therefore the measurements are vulnerable to correlated noise.

If a secondary eclipse can be detected with sufficient significance, this provides a stringent test of the eccentricity (see Section 3.2.1).

López-Morales et al. have measured the secondary eclipse of WASP-12b from the ground with SPICam on the ARC telescope at Apache Point Observatory in the z' band. Their initial results were submitted to arXiv.org as López-Morales et al. (2009), version 1, but their final version (López-Morales et al., 2010) differs significantly with respect to the eccentricity. We refer to their version 1 as L09. Their best-fit the result in L09 paper initially indicated a secondary eclipse with a significant time lag ($e\cos\omega = 0.0156 \pm 0.0035$) compared to the epoch expected for a circular orbit, with a similar level of significance to H09. Nevertheless, the presence of residual correlated noise is apparent in the L09 data (see Fig. 4.3), as expected for ground-based photometry at such a high accuracy — the depth of the secondary eclipse is only about 0.08 ± 0.02 %.

As a result, the issue remained inconclusive until a space-based measurement of the secondary eclipse with the Spitzer Space Telescope (Campo et al., 2011, hereafter C10) unambiguously showed that the timing of the secondary eclipse was consistent with a circular orbit. This result suggested that the L09 time lag was probably due to instrumental systematics, and that the orbit of WASP-12b was probably circular, since a fine-tuned alignment would be required to reconcile the Spitzer result with the H09 value of the eccentricity. Following this, (López-Morales et al., 2010) have reanalysed their data and revised their estimate to $e\cos\omega = 0.016^{+0.011}_{-0.009}$.

After WASP-12b, WASP-14b is a transiting planet with the second-shortest period (P=2.2 days), having a reported non-circular orbit (Joshi et al., 2009, $e = 0.091 \pm 0.003$). This makes it another test-case for tidal evolution of close-in gas giants. If its orbital eccentricity is indeed near 0.1, then this non-zero but relatively low value — in the context of the distribution of giant exoplanet eccentricities — makes it likely that this planet has undergone some degree of orbital evolution, and is still subject to strong tidal forces at present. Therefore its presence may be useful to constrain the tidal synchronisation timescale. It is also an important object when studying the issue of the anomalous radius of hot Jupiters because of its inflated size, with $R_p = 1.28\,\mathrm{R_J}$. WASP-14b occupies a distinctive position in the relevant parameter space: irradiation, orbital distance, eccentricity and size.

4.2 New observations for WASP-12 and WASP-14

We obtained 29 radial-velocity measurements for WASP-12 (16 during a single night, and 13 at various values of orbital phase, see Table A.1) and 11 for WASP-14 (see Table A.2), using the SOPHIE spectrograph installed on the 1.93-m telescope at OHP (France). The observations were gathered between 17 January

2009 and 27 March 2010. The 16 in-transit measurements for WASP-12 were initially obtained with the objective of constraining the spin-orbit angle via the Rossiter-McLaughlin effect. The typical exposure times were 1098 s and 552 s for WASP-12 and WASP-14 respectively. [1]

4.3 The orbital eccentricity of WASP-12b

4.3.1 Correlated noise in RV and photometric data

Figure 4.1 shows our radial-velocity data for WASP-12, together with a circular orbital solution (solid line, residuals shown in the lower panel) and the eccentric-orbit fit of H09 (dotted). Our radial velocity data are shown together with the H09 data in Figure 4.2. As the Figure shows, the radial-velocity signal cannot be adequately modelled by a periodic orbital signal affected by random noise. The presence of a correlated non-periodic component is especially obvious during the in-transit sequence. This could be due to instrumental noise, stellar variability or an unaccounted planetary companion in the system, all of which would behave in the same way as far as the orbital fit is concerned. Given our experience with SOPHIE in High Efficiency mode (see Figure 3.1), we consider the first cause as likely.

We use the transit lightcurve from H09 and the secondary eclipse lightcurves from L09 and C10 with our own radial velocity measurements to perform a global fit with a Keplerian orbit, and we account for the effect of red noise by modifying the uncertainties on the data as explained in Section 3.5.

For the H09 photometric transit, we estimate $\sigma_r = 0.0005$ (out of transit flux normalised to 1.0) and $N = 20$. Similarly, for the L09 data, we set $\sigma_r = 0.0002$ (out of transit flux normalised to 1.0) and $N = 9$. For the C10 data, we set $\sigma_r = 0.0005$ (out of transit flux normalised to 1.0) and $N = 9$. For our own radial velocity data, we estimate the red noise parameter to be 9 m s^{-1}, and $N = 16$ during the transit and $N = 1$ outside the transit. The former measurements are taken on the same night, so $N = 16$ guards against the possibility these points were shifted together due to instrumental systematics or other effects, while the other points are taken in different nights so that the uncertainties are not expected to be correlated.

4.3.2 Analysis

We use the MCMC procedure described in Section 3.4. We vary the period P, mid-transit time T_{tr}, system velocity v_0, eccentricity components $e\cos\omega$ and $e\sin\omega$, semi-amplitude K, impact parameter b, scaled planetary radius R_p/R_s, the stellar mass M_s, stellar radius R_s and effective temperature $T_{\rm eff}$ of the star. The scaled semi-major axis a/R_s is calculated from the assumption of a Keplerian orbit using the period P. We also include a separate term for the depth of each secondary eclipse data set, because the depth varies with wavelength.

We set the quadratic limb darkening parameters for the H09 transit to $u_a = 0.1274$ and $u_b = 0.3735$ according to Claret (2004a). We ran the MCMC code for 800,000 steps, and found 18% of the steps were accepted.

[1] These measurements were not made by the author, but by the co-authors (see Author's declaration).

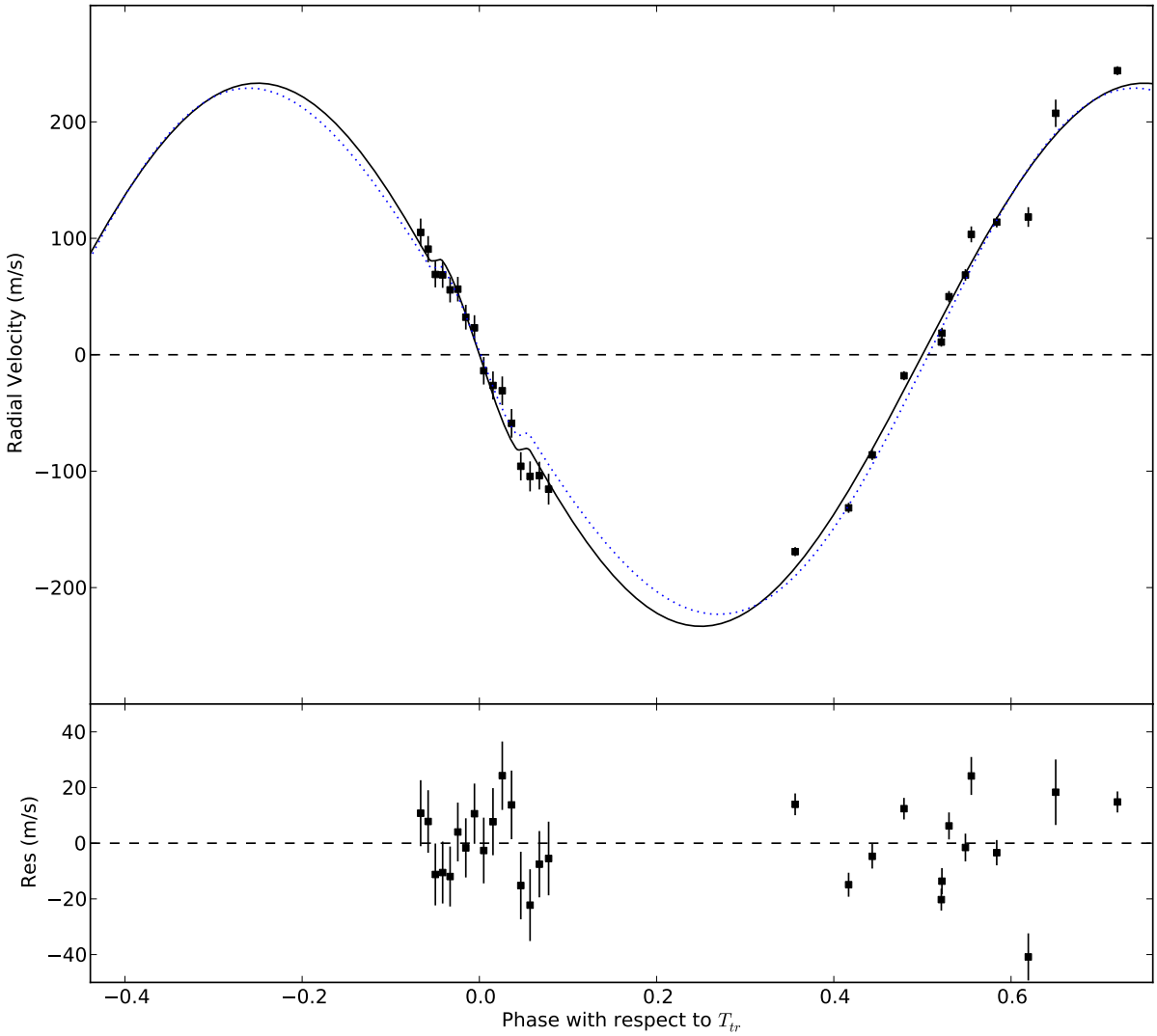

Figure 4.1: Plot showing our new SOPHIE radial velocity data for WASP-12, overplotted with a circular orbit (solid line) and an orbit with the orbital parameters given in H09. The residuals relative to the circular orbit are shown in the bottom panel.

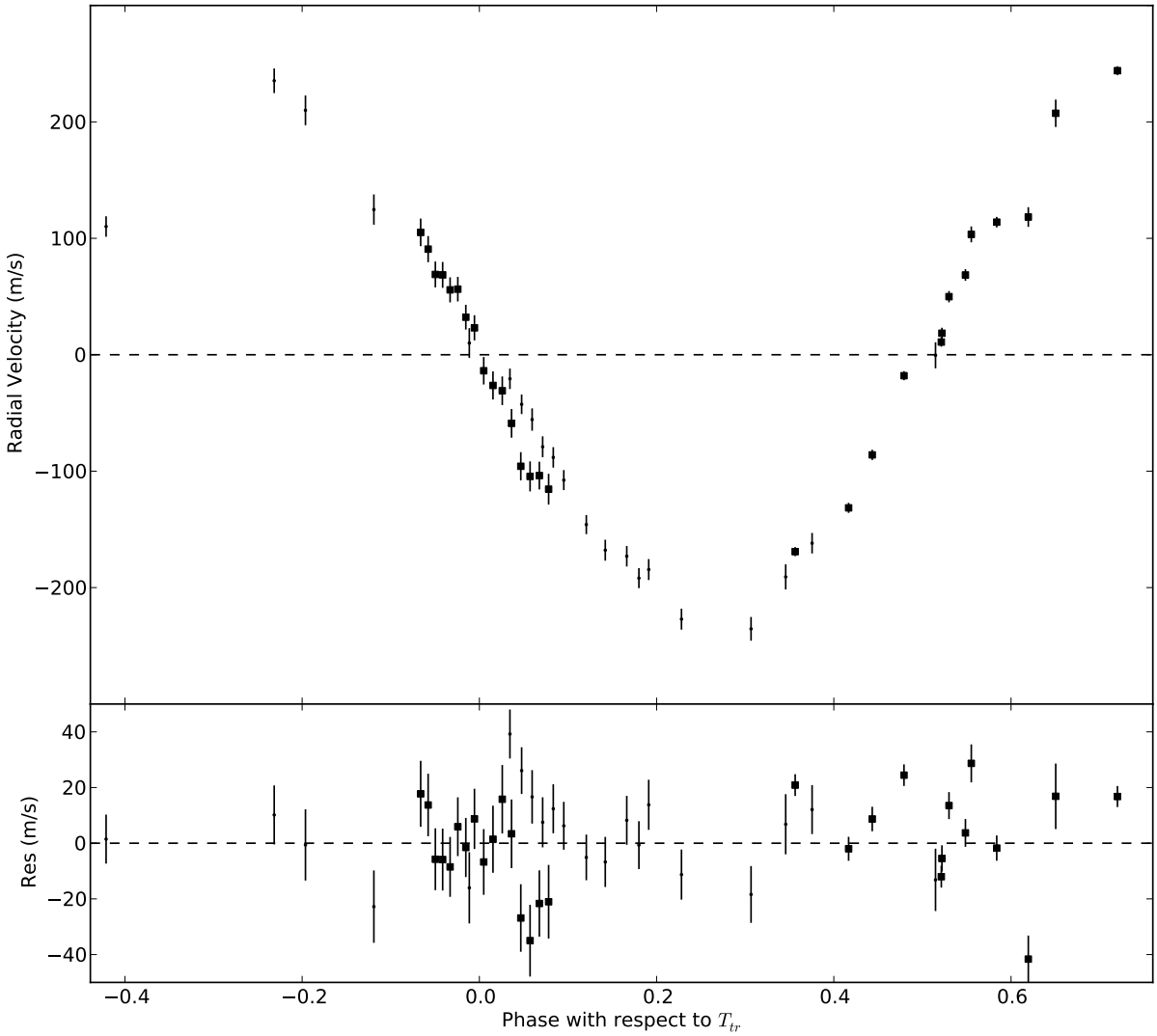

Figure 4.2: Plot showing all the radial velocity data for WASP-12, with our new SOPHIE data plotted with square symbols and the H09 data plotted with dots. Residuals for an orbit with the H09 value of eccentricity, $e = 0.049$, are shown in the bottom panel.

Parameter	H09	New SOPHIE RV and photometry
Centre-of-mass velocity V_0 [km s^{-1}]	19.085±0.002	19.062±0.014
Orbital eccentricity e	0.049±0.015	$0.018^{+0.024}_{-0.014}$
Argument of periastron ω [^{o}]	-74^{+13}_{-10}	0 (unconstrained)
$e\cos\omega$		0.0035±0.0034
$e\sin\omega$		0.0177±0.028
Velocity semi-amplitude K [m s^{-1}]	226±4	238±11

Table 4.1: System parameters for WASP-12. Left: H09. Right: Our SOPHIE radial velocity data, H09 transit photometry data and L09 and C10 secondary eclipse photometry data. Median values are quoted as well as 68.3% confidence limits.

4.3.3 Eccentricity

The best solution with our radial velocity data and the constrains from the transit and secondary eclipse light curves gives $e = 0.018^{+0.024}_{-0.014}$. The value of χ^2 for the circular orbit is $\chi^2_c = 33.60$ and the value for an eccentric orbit is $\chi^2_e = 32.19$. When these are entered into Equation 3.18 using $k = 4$ (P, T_{tr}, V_0,K) and 6 (i.e. including $e\sin\omega$ and $e\cos\omega$) respectively, and $M = 29$, we obtain the BICs as $\mathrm{BIC}_c = 47.07$ and $\mathrm{BIC}_e = 52.40$. This means that the circular orbit is preferred, because the "gain" in minimising χ^2 is offset by the penalty for including two additional parameters e and ω and that according to the data, we do not have the evidence to reasonably maintain that the orbit is eccentric. Using the Lucy & Sweeny test, the significance of the eccentricity is $p = 0.61$, corresponding to a 0.51-σ result.

Our results for the orbital parameters of the WASP-12 system are shown in Table 4.1, with the results of the analysis of our new SOPHIE RV data used in combination with the H09 transit lightcurve, and the L09 and C10 secondary eclipse lightcurves, compared to the H09 parameters.

The H09 radial-velocity data forces the solution towards a higher eccentricity, significant at the $\sim 3\sigma$ level, but Figure **??** suggests that this is probably an artefact due to an excursion of the zero-point between different nights.

It is interesting to compare the situation in radial velocity with the similar sequence of events regarding the secondary eclipse photometric data. Figure 4.3 (left panel) shows the secondary eclipse data for both L09 (top two panels) and C10 (bottom two panels). The solid line shows a circular orbit, from a global fit assuming $e = 0$. The dotted line represents the L09 solution (eccentricity $e = 0.057$, and the residuals are plotted for both datasets for the L09 (eccentric) solution. This shows that the L09 eccentric solution is somewhat plausible for the L09 data but definitely not for the C10 data. Figure 4.3 (right panel) shows the same data, and the solid line is still a circular orbit $e = 0$. The residuals for both datasets are now plotted for the circular solution $e = 0$. It is clear that the circular solution fits the C10 dataset better and remains reasonable for the L09 dataset. This could be explained if the effects of instrumental systematics had been underestimated in the original L09.

4.3.4 Rossiter-McLaughlin effect

Although our data cover a complete spectroscopic transit, and thus potentially constrains the projected spin-orbit angle of the WASP-12 system through the

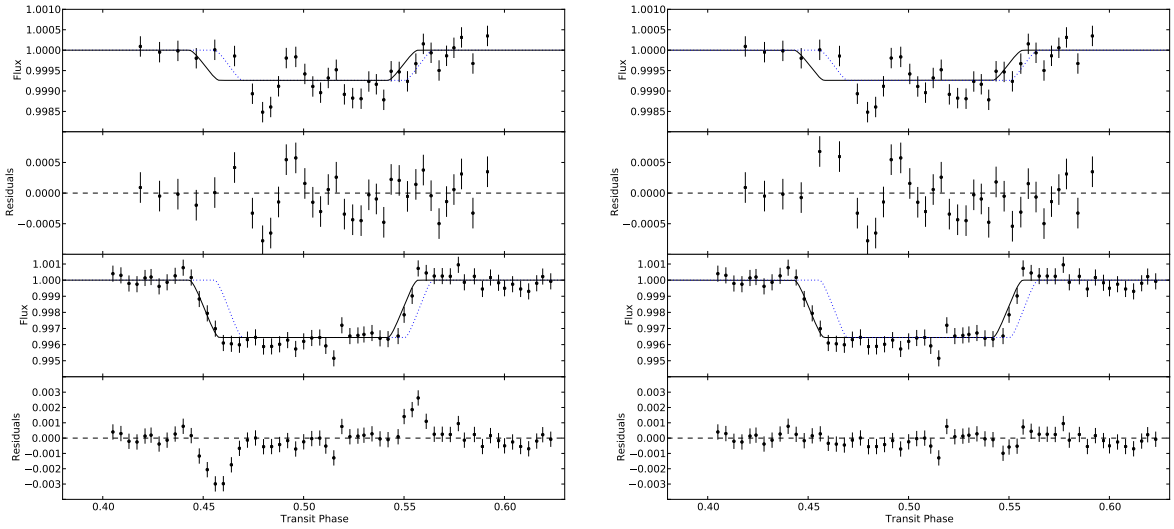

Figure 4.3: Secondary eclipse flux for WASP-12. **Both left and right:** The top two panels show L09 flux and residuals while the bottom two panels show C10 flux and residuals. As in Figure 1, solid lines represent the secondary eclipse prediction for a circular orbit ($e = 0$), and dotted lines represent the secondary eclipse prediction for an eccentric orbit (orbital eccentricity from L09 et al. $e = 0.057$).
Left: Residuals are plotted for the L09 solution of $e = 0.057$, which is clearly inappropriate for the C10 secondary eclipse (bottom).
Right: Residuals are plotted for the circular orbit, which is clearly more appropriate for the C10 secondary eclipse (bottom).

Rossiter-McLaughlin effect, the constraint is weak once the possible presence of non-random noise is taken into account. The distribution of the spin-orbit angle from our MCMC exploration spans a wide interval extending from a prograde orbit to a projected spin-orbit angle larger than 90 degrees, as shown in Figure 4.4. The data marginally favours a prograde rather than retrograde orbit, with the odds, i.e. the ratio of prograde to retrograde orbits, at 1.05. We therefore allow λ to be free in our calculations for eccentricity. This does not appreciably alter the orbital parameters (for example the derived eccentricity in the case of using a free parameter λ is $e = 0.018^{+0.024}_{-0.014}$, while fixing $\lambda = 0$ yields $e = 0.017^{+0.015}_{-0.010}$).

4.3.5 Secondary companion

We also looked for possible evidence for a second planetary companion in the system by examining the residuals as function of time and include a linear trend in the fitting process:

$$v(t) = v_{\rm keplerian}(t) + \dot{\gamma}(t - t_0), \tag{4.1}$$

We set $t_0 = 2454900$ to allow the MCMC to explore values of $\dot{\gamma}$ and we reran the MCMC twice: once for a circular orbit and once for an eccentric orbit. For the circular orbit, we found that the limits on the gradient are $\dot{\gamma} = 0.052 \pm 0.054$ m s^{-1}day^{-1} and $\chi^2 = 27.50$, giving BIC$_{\rm linear\,trend,circular} = 44.34$, using $k = 5$ to penalise this circular model for the extra term. For the eccentric orbit, we found that the limits on the gradient are $\dot{\gamma} = 0.050 \pm 0.054$ m s^{-1}day^{-1} and $\chi^2 = 27.39$,

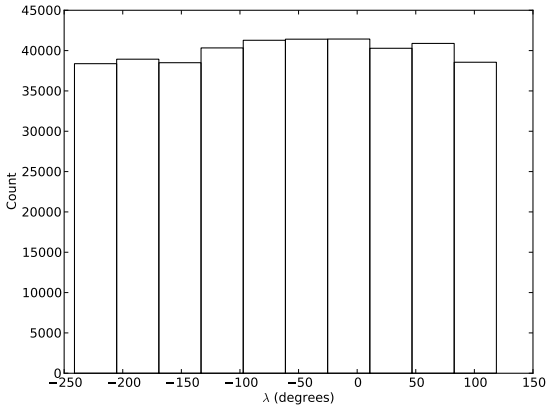

Figure 4.4: Histogram of the projected spin-orbit angle λ for WASP-12. This shows that the spin-orbit angle is not very well constrained, although it favours a prograde orbit.

giving $\mathrm{BIC}_{\text{linear trend,eccentric}} = 50.96$, using $k = 7$ to penalise this eccentric model for the extra term. This would appear to favour the circular model with a trend of $\dot{\gamma} = 0.052 \pm 0.054$ m s^{-1}day^{-1} , but since this result is consistent with no trend, and we know from experience that it is possible to obtain this magnitude of a trend ($\sim$20m s^{-1}over 400 days) with SOPHIE, we do not consider this trend to be significant.

4.3.6 Light travel time

For completeness, we include a discussion of the light travel time across the system. The negligible delay in the secondary eclipse as detected by C10, $(0.0012 \pm 0.0006)P$ would be significant if the light travel time across the system (in reality, only $\sim$ 10 seconds) were much longer than the measured delay ($\sim$ 110 seconds) and the uncertainties $\sim$ 60 seconds. In that case, the light travel time would induce a delay in the secondary eclipse detection, and a measurement showing a negligible delay would suggest an eccentric orbit was giving an offset that exactly cancelled the light travel time. This is not supported here, however, because the light travel time is smaller than both the shift and the uncertainty in the timing of the secondary eclipse according to the Spitzer measurements.

4.3.7 Apsidal precession

C10 suggested that, for an eccentric orbit, the difference between the secondary eclipse phase in C10 and L09 could be due to apsidal precession. This would require that the argument of periastron had changed from $\omega = -74^{+13}_{-10}$ in Feb 2008 (H09) to $\omega \sim -90^{o}$ in Oct 2008 (C10). In terms of the projected component of the eccentricity, $e\cos\omega$, one obtains $e\cos\omega = 0.014 \pm 0.004$ in Feb 2008 using the H09 orbital parameters, C10 found $e\cos\omega = 0.0019 \pm 0.0007$ in Oct 2008, L09 found $e\cos\omega = 0.0156 \pm 0.0035$ in Feb-Oct 2009, and our result is $e\cos\omega = 0.0037 \pm 0.0035$ for January 2009 to March 2010. When considered in the order that observations were made, these values do not support the hypothesis of apsidal precession.

4.4 The orbital eccentricity of WASP-14b

Figure 4.5 shows our new SOPHIE data and the existing FIES and SOPHIE data from Joshi et al. (2009) along with with the best-fit orbit and a circular orbit. We adopt the prior distribution on the period P from photometric data by Johnson et al. (2009) and that on the mid-transit time T_{tr} from Joshi et al. (2009). We work out the orbital parameters using both our radial velocity data and that published in the discovery paper.

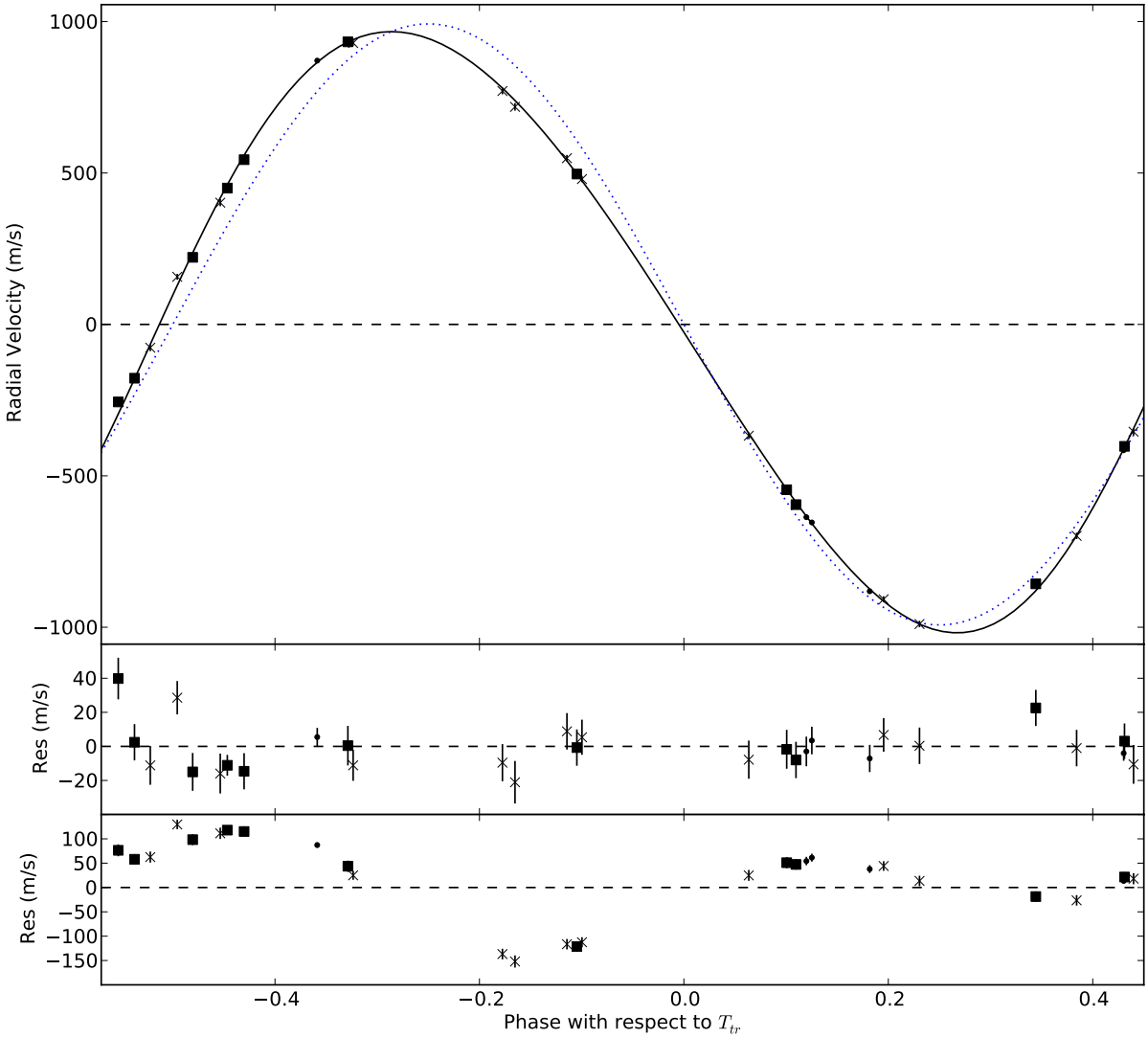

Figure 4.5: The new SOPHIE radial velocity data for WASP-14 are shown with squares, while the Joshi et al. (2009) data from FIES and SOPHIE are shown with points and crosses respectively. The solid line is the best solution with $e = 0.0877$, and the dotted line is a circular orbit. The middle panel shows residuals plotted for the best-fit orbit e=0.0877, while the bottom panel shows residuals for a circular orbit (using the parameters of Joshi et al., 2009, for the spectroscopic transit).

Parameter	Joshi et al	This paper
Centre-of-mass velocity V_0[km s^{-1}]		-4.985 ± 0.003
Orbital eccentricity e	0.091 ± 0.003	0.0877 ± 0.0030
Argument of periastron ω [^{o}]	-106.6 ± 0.7	-107 ± 1
$e\cos\omega$		-0.026 ± 0.002
$e\sin\omega$		-0.082 ± 0.003
Semi-amplitude K [m s^{-1}]	993 ± 3	991 ± 3

Table 4.2: System parameters for WASP-14. Left: Joshi et al. Right: Our results. Median values are quoted as well as 68.3% confidence limits.

We include the effect of red noise as explained in Section 3.5, adding 8 m s^{-1} of correlated uncertainties to each single datapoint and $\sqrt{N}\times 8$ m s^{-1} to each point in each group where N is the number of points were taken on the same night (determined from the timestamps).

We ran the MCMC code for 800,000 steps, and found 16% of the steps were accepted. Our results are shown in Table 4.2. Our best-fit value for the orbital eccentricity is $e = 0.0877 \pm 0.0030$, in good agreement with the value found by Joshi et al. (2009) ($e = 0.091 \pm 0.003$).

We examined the possibility of a scenario similar to that of WASP-12b, with correlated noise causing a spurious eccentricity detection. The lower panel of Figure 4.5 shows the residuals around the best-fit circular orbit (given by a MCMC run with $e = 0$ fixed). We find that, in contrast to the case of WASP-12b, the differences between observation and model assuming a circular solution are periodic and regular, which would not be the case for correlated noise. The value of χ^2 for a circular orbit is $\chi^2_c = 865$ and that for an eccentric orbit is $\chi^2_e = 29.3$. When these are entered into Equation 3.18 using $k = 3$ (two values of V_0, one for our data with SOPHIE and one for the data from Joshi *et al.*, 2009, using SOPHIE, and the semi amplitude K) and $k = 5$ (two additional parameters, the eccentricity e and the argument of periastron ω) respectively, and $M = 38$ (we used both the Joshi, 2009 SOPHIE data and our own RV), we obtain the BICs as $\mathrm{BIC}_c = 876$ and $\mathrm{BIC}_e = 47.5$. The circular orbit is thus overwhelmingly rejected. Using the Lucy & Sweeny test (Section 3.10), the significance is $p = 5.53\times10^{-25}$, corresponding to a 10.3-σ detection.

4.4.1 Secondary companion

In the same manner as for WASP-12b, we looked for possible evidence for a second planetary companion in the system by examining the residuals as function of time, by including a linear trend in the fitting process according to Equation 4.1 and we reran the MCMC for both a circular and an eccentric orbit. This time we set $t_0 = 2454460$ HJD. For the circular orbit, we found that the limits on the gradient are $\dot{\gamma} = 0.070^{+0.054}_{-0.042}$ m s^{-1}day^{-1} and $\chi^2 = 852$, giving $\mathrm{BIC}_{\mathrm{linear\,trend,circular}} = 867$, using $k = 4$ to penalise this circular model for the extra term. For the eccentric orbit, we found that the limits on the gradient are $\dot{\gamma} = 0.078^{+0.038}_{-0.046}$ m s^{-1}day^{-1} and $\chi^2 = 27.5$, giving $\mathrm{BIC}_{\mathrm{linear\,trend,eccentric}} = 49.3$, using $k = 6$ to penalise this eccentric orbit model for the extra term. The eccentric orbit without any linear trend is thus favoured, because it had the lowest BIC.

4.5 Discussion

From Mazeh (2008), we can work out the circularisation timescale for a system, using

$$\tau_{\rm circ} = \frac{P}{21\pi}\left(\frac{Q_p}{k_p}\right)\left(\frac{M_p}{M_s}\right)\left(\frac{a}{r_p}\right)^5, \tag{4.2}$$

which yields about 10^5 yr for WASP-12b, and 5×10^7 yr for WASP-14b if we assume $Q_p/k_p = 10^5$ from Goldreich and Soter (1966). This should be compared to the ages of the systems, 2.4×10^9 (H09) and $0.5-1\times10^9$ Joshi et al. (2009) yr respectively. The circularisation timescale (e.g. Jackson, Greenberg, and Barnes, 2008a; Lecar, Wheeler, and McKee, 1976) is given by

$$\frac{1}{e}\frac{de}{dt} = -\frac{1}{\tau_{\rm circ}}, \tag{4.3}$$

up to a factor of 2. We can therefore estimate that WASP-12b's orbit should be subject to tidal effects at a factor of $\sim$400 larger than WASP-14b if it really had an eccentric orbit.

Our results, on the other hand, confirm the strong indications of C10 that all the available data for WASP-12b is compatible with a circular orbit, and that the eccentricity of the best-fit orbit to the radial velocity of H09 and subsequently the secondary eclipse data of L09 may be due to correlated noise. Not accounting for this noise in the statistical analysis could lead to an apparent $\sim 3\sigma$ significance for the rejection of the null hypothesis ($e = 0$), but the new data strongly suggest that the orbit of WASP-12b is indeed circular.

A circular orbit for WASP-12b removes the need for models to explain the survival of such an eccentricity at this very short period, in face of what would have been extremely strong tidal effects. In particular, the scenario of Li et al. (2010), using the eccentricity from H09 to infer values of mass loss and tidal dissipation for WASP-12b, loses its principal empirical support.

The eccentricity of WASP-14b, in contrast, is confirmed by our measurements. This illustrates the capacity of SOPHIE to measure accurate values of orbital eccentricity for transiting planets, given a sufficient number of measurements well distributed in phase and spread over different nights (the measurements for WASP-12 having most weight towards an eccentric solution were gathered during only two different nights).

Conclusion

In this chapter, we have looked at the observational evidence for the orbital eccentricities of WASP-12b and WASP-14b. Even though the orbit of WASP-12b initially appeared to be eccentric, newer data showed the original detection was spurious. In contrast, we confirmed the orbital eccentricity of WASP-14b. In the next chapter, we expand our study, to look at a larger set of transiting exoplanets.

Chapter 5

Analysis: Known Transiting Objects

In the previous chapter, we saw how correlated noise in RV measurements can cause spurious eccentricity detections, using WASP-12b as the canonical example. The spurious detection of an eccentricity for WASP-12b suggested there could be more transiting hot Jupiters for which the eccentricity has been overestimated in the literature, due to limited datasets. In this chapter, we expand our sample, and add new measurements for some objects. This allows us to obtain a global view of the transiting exoplanet sample, and put constraints on the eccentricities.

5.1 Larger sample & new data

Given the rapid rate of announcement of new transiting exoplanets, we had to stop the clock somewhere, and we picked the 1st of July 2010. We selected only objects that had been reported in peer-reviewed journals or on the online preprint archive ArXiV.org. Moreover, we selected systems with well measured parameters (planetary radius R_p and mass M_p to within 10%) and excluded faint objects ($V > 15$). At that time, 64 such systems were known. In Chapter 4, we investigated the orbits of WASP-12b and WASP-14b, as described in the paper by Husnoo et al. (2011). In this chapter, we discuss the whole sample, as described in Pont et al. (2011) and Husnoo et al. (2012).

We carried out a literature survey and collected radial velocity measurements for 54 transiting planets, as well as other relevant data such as the orbital periods and the time of mid-transit. For the cases of CoRoT-1, CoRoT-2 and GJ-436, we also used the secondary eclipse constraint on the eccentricity component $e\cos\omega$ from Alonso et al. (2009a), Alonso et al. (2009b) and Deming et al. (2007), respectively. In addition to the cases of WASP-12 and WASP-14, we used new measurements for 10 of these 54 systems: 73 new measurements for 6 objects in the Southern hemisphere using the HARPS spectrograph (CoRoT-1, CoRoT-3, WASP-2, WASP-4, WASP-5 and WASP-7 — see Section 3.1.3 and Tables A.3, A.4, A.5, A.6, A.7 and A.8), and 45 new measurements for 4 objects in the Northern Hemisphere using the SOPHIE spectrograph (HAT-P-4, HAT-P-7, TrES-2 and XO-2 — see Section 3.1.3 and Tables A.9, A.10, A.11 and A.12)[1]. We reanalyse the existing radial velocity data for those 54 transiting systems (including the additional radial velocity measurements for 10 systems described above), and

[1]These measurements were not made by the author, but by the co-authors (see Author's declaration).

include 10 systems without further reanalysis of orbital ephemeris (CoRoT-10, HAT-P-2, HAT-P-13, HAT-P-15, HD 17156, HD 80606, HD 189733, HD 209458, Kepler-5, XO-3). These systems, and the updated estimates of their orbital eccentricities are listed in Table 5.1.

In Section 5.2, we describe our procedure for estimating the correlation timescale of the red noise in the radial velocity data. In Section 5.3, we describe the planets for which we do not consider the evidence for an orbital eccentricity compelling, despite previous evidence of a departure from circularity ($e > 1\sigma$ from zero), followed by Section 5.4, where we describe the planets for which we consider the orbital eccentricity to be either so small as to be undetectable or compatible with zero. In Section 5.5 we describe planets that can be safely considered to be on eccentric orbits and finally, in Section 5.6, we describe the planets for which we consider the orbital eccentricity to be poorly constrained (as described in Section 3.10). In Section 5.7, we include a further 16 systems, which had been discovered by the time the paper was submitted. Since the original publications, yet more systems have been reported, and we include another 14 objects.

5.2 Estimating the correlation timescale

As described in Section 3.5, we use a simplified correlation matrix based on two parameters to describe the correlation timescale τ and amplitude σ_r. There is a degeneracy between σ_r and τ for the time sampling typical of our RV data: if we assume a long timescale compared to the interval of time between the measurements, we are asserting that we have a reason to believe that several measurements may have been systematically offset in the same direction. A measurement that occurs within that timescale but is offset to a very different extent from nearby measurements (e.g. if the correlation timescale τ has been overestimated) will require a larger value of σ_r for the dataset as a whole to yield a reduced χ^2 of unity.

To estimate τ, we looked at several datasets for each of the instruments HARPS, HIRES and SOPHIE. We repeated the analysis in Section 3.4 using values of τ in the range 0.1–5 d, to check for weather-related correlations. To see the effects of choosing between an eccentric orbit or a circular orbit on our estimation of τ, we carried each analysis twice, by adjusting σ_r (see Section 3.5) to obtain a reduced χ^2 of unity (within 0.5%) for each orbital model (circular and eccentric). We plotted the optimal values of σ_r against τ for several objects using data obtained from different instruments separately, as shown in Figure 5.1. For WASP-2, we used our new HARPS measurements (Table A.5) as well as SOPHIE measurements from Collier Cameron et al. (2007). For WASP-4 and WASP-5, we used our new HARPS measurements (Tables A.6 and A.7), and for HAT-P-7, we used our new SOPHIE measurements (Table A.10) as well as HIRES measurements from Winn et al. (2009a). We found that for those datasets and objects where the orbital elements were well-constrained the plot showed a gentle increase in σ_r with τ, for $\tau \leq 1.5$d, then increased much faster for these datasets at a timescale of $\tau > 1.5$ d. For objects that have been observed with multiple instruments, this characteristic timescale is independent, both of the instrument used or the assumption about the eccentricity (i.e. free eccentricity or e fixed at zero), suggesting that the correlated noise is probably related to weather conditions. We therefore assumed a correlation timescale of 1.5 d in the rest of this

Name	Eccentricity (literature)	Eccentricity *(this work)*	95% limit	E	$M_p(M_j)$ *(this work)*
CoRoT-1b	–	0.006±0.012	(<0.042)	C	1.06±0.14
CoRoT-2b	–	0.036±0.033	(<0.10)	P	3.14±0.17
CoRoT-3b	$0.008^{+0.015}_{-0.005}$	0.012±0.01	(<0.039)	C	21.61±1.2
CoRoT-4b	0 ± 0.1	0.27±0.15	(<0.48)	P	0.659±0.079
CoRoT-5b	$0.09^{+0.09}_{-0.04}$	0.086±0.07	(<0.26)	P	0.488±0.032
CoRoT-6b	< 0.1	0.18±0.12	(<0.41)	P	2.92±0.30
CoRoT-9b	0.11±0.04	0.11±0.039	(<0.20)	E	0.839±0.070
CoRoT-10b	0.53±0.04	0.53±0.04	–	E	2.75±0.16
GJ-436b	0.150±0.012	0.153±0.017	–	E	0.069±0.006
GJ-1214b	< 0.27 (95%)	0.12±0.09	(<0.34)	P	0.020±0.003
HAT-P-1b	< 0.067 (99%)	0.048±0.021	(<0.087)	P	0.514±0.038
HAT-P-2b	0.517±0.003	0.517±0.003	–	E	8.76±0.45
HAT-P-3b	–	0.1±0.05	(<0.20)	P	0.58±0.17
HAT-P-4b	–	0.063±0.028	(<0.107)	P	0.677±0.049
HAT-P-5b	–	0.053±0.061	(<0.24)	P	1.09±0.11
HAT-P-6b	–	0.047±0.017	(<0.078)	P	1.031±0.053
HAT-P-7b	< 0.039 (99%)	0.014±0.01	(<0.037)	C	1.775±0.070
HAT-P-8b	–	0.011±0.019	(<0.064)	C	1.340±0.051
HAT-P-9b	–	0.157±0.099	(<0.40)	P	0.767±0.10
HAT-P-11b	0.198±0.046	0.28±0.32	(<0.80)	P	0.055±0.022
HAT-P-12b	–	0.071±0.053	(<0.22)	P	0.187±0.033
HAT-P-13b	$0.014^{+0.005}_{-0.004}$	0.014±0.005	(<0.022)	C	0.855±0.046
HAT-P-14b	0.107±0.013	0.11±0.04	(<0.18)	P	2.23±0.12
HAT-P-15b	0.190±0.019	0.19±0.019	–	E	1.949±0.077
HAT-P-16b	0.036±0.004	0.034±0.003	(<0.039)	ES	4.20±0.11
HD17156b	0.677±0.003	0.675±0.004	–	E	3.223±0.087
HD80606b	0.934±0.001	0.933±0.001	–	E	3.99±0.33
HD149026b	–	0.121±0.053	(<0.21)	P	0.354±0.031
HD189733b	$0.004^{+0.003}_{-0.002}$	0.004±0.003	(<0.0080)	C	1.139±0.035
HD209458b	0.014±0.009	0.014±0.009	(<0.042)	C	0.677±0.033
Kepler-4b	$0.25^{+0.11}_{-0.12}$ (< 0.43)	0.25±0.12	(<0.43)	P	0.077±0.028
Kepler-5b	$0.034^{+0.029}_{-0.018}$ (< 0.086)	0.034±0.029	(<0.086)	C	2.120±0.079
Kepler-6b	$0.056^{+0.044}_{-0.028}$ (< 0.13)	0.057±0.026	(<0.12)	P	0.659±0.038
Kepler-7b	$0.102^{+0.104}_{-0.047}$ (< 0.31)	0.065±0.045	(<0.19)	P	0.439±0.044
Kepler-8b	$0.35^{+0.15}_{-0.11}$ (< 0.59)	0.011±0.24	(<0.39)	P	0.57±0.11
TrES-1b	–	0.019±0.054	(<0.21)	P	0.757±0.061
TrES-2b	–	0.023±0.014	(<0.051)	C	1.195±0.063
TrES-3b	–	0.066±0.048	(<0.16)	P	1.86±0.12
TrES-4b	–	0.21±0.21	(<0.66)	P	0.93±0.17
WASP-1b	–	0.19±0.22	(<0.65)	P	0.89±0.15
WASP-2b	–	0.027±0.023	(<0.072)	C	0.852±0.080
WASP-3b	–	0.009±0.013	(<0.048)	C	1.99±0.13
WASP-4b	–	0.005±0.003	(<0.011)	C	1.205±0.044
WASP-5b	$0.038^{+0.026}_{-0.018}$	0.012±0.007	(<0.026)	C	1.571±0.063
WASP-6b	$0.054^{+0.018}_{-0.015}$	0.041±0.019	(<0.075)	C	0.480±0.038
WASP-7b	–	0.074±0.063	(<0.23)	P	1.07±0.16
WASP-10b	$0.057^{+0.014}_{-0.004}$	0.052±0.031	(<0.11)	P	3.15±0.12
WASP-11b	–	0.091±0.054	(<0.21)	P	0.470±0.035
WASP-12b	0.049 ± 0.015	0.018±0.018	(<0.05)	C	1.48±0.14
WASP-13b	–	0.14±0.1	(<0.32)	P	0.458±0.064
WASP-14b	0.091±0.004	0.088±0.003	(<0.090)	ES	7.26±0.59
WASP-15b	–	0.056±0.048	(<0.17)	P	0.548±0.059
WASP-16b	–	0.009±0.012	(<0.047)	C	0.846±0.072
WASP-17b	$0.129^{+0.106}_{-0.068}$	0.121±0.093	(<0.32)	P	0.487±0.062
WASP-18b	0.009 ± 0.001	0.007±0.005	(<0.018)	C	10.16±0.87
WASP-19b	0.02±0.01	0.011±0.013	(<0.047)	C	1.15±0.10
WASP-21b	–	0.048±0.024	(<0.11)	P	0.308±0.018
WASP-22b	0.023 ± 0.012	0.022±0.016	(<0.057)	C	0.56±0.13
WASP-26b	–	0.033±0.025	(<0.086)	C	1.018±0.034

Table 5.1: (Continued on the next page.)

Name	Eccentricity (literature)	Eccentricity *(this work)*	95% limit	E	$M_p(M_j)$ *(this work)*
XO-1b	–	0.042±0.088	(<0.30)	P	0.911±0.088
XO-2b	–	0.064±0.041	(<0.14)	P	0.652±0.032
XO-3b	0.287±0.005	0.287±0.005	–	E	11.81±0.53
XO-4b	–	0.28±0.15	(<0.50)	P	1.56±0.30
XO-5b	–	0.01±0.01	(<0.036)	C	1.065±0.036

Table 5.1: Table showing the objects which we considered in this study. We have included the fifth column to show if the object is on a circular orbit ("C", ie circular according to the BIC test and 95% limit on e is less that 0.1), "E", for objects that are on eccentric orbits (either determined to be eccentric using the BIC test, or the orbit is clearly eccentric from the radial velocity plot), or "P", for objects which we fail to place any useful constraints on the eccentricity (ie the 95% limit on e is larger than 0.1), or it is unclear from model selection whether the orbit is circular or eccentric.

study, unless otherwise noted. This means that we are accounting for the red noise in the same-night measurements, and for measurements that are taken further apart in time, this procedure reduces to the more familiar "jitter" term. The value of σ_r inferred at $\tau = 1.5$ d in some cases varies by a few percent depending on the model chosen, i.e. eccentric or circular, and varies across datasets, as discussed later.

We also investigated the effects of varying τ on our final results. For the same systems discussed above, we plotted the 95% upper limit on the eccentricity as obtained from each dataset separately. The results are shown in Figure 5.2, where it is clear that the choice of τ has no effect on the final result for $\tau \geq 1.5$ d. The only exception is WASP-2 (HARPS), where we only have 8 measurements and the phase coverage is not as complete as for the other objects (see Figure 5.10). Similarly, the derived parameters V_0 and K did not vary appreciably with τ.

5.3 Orbits that no longer qualify as eccentric

In a number of cases in the past, the derived eccentricity from an MCMC analysis deviated from zero by more than 1σ, for example CoRoT-5b, GJ436b, WASP-5b, WASP-6b, WASP-10b, WASP-12b, WASP-14b, WASP-17b and WASP-18b. In this Section, we discuss the cases of 7 planets, CoRoT-5b, WASP-6b, WASP-10b, WASP-12b, WASP-17b, WASP-18b and WASP-5b, that are shown to have orbital eccentricities that are compatible with zero.

CoRoT-5

CoRoT-5b is a 0.46 M_j planet on a 4.03 day orbit around a F9 star (V=14.0), first reported by Rauer et al. (2009). Using 6 SOPHIE measurements (one of which is during the spectroscopic transit, which we ignore in this study) and 13 HARPS measurements, the authors derived a value of eccentricity $e = 0.09^{+0.09}_{-0.04}$. In our study, we used the formal uncertainties quoted with the data without any additional noise treatment, since they resulted in a reduced χ^2 less than unity for both an eccentric and a circular orbit. We imposed the prior information from photometry $P = 4.0378962(19)$ and $T_{tr} = 2454400.19885(2)$ from the Rauer

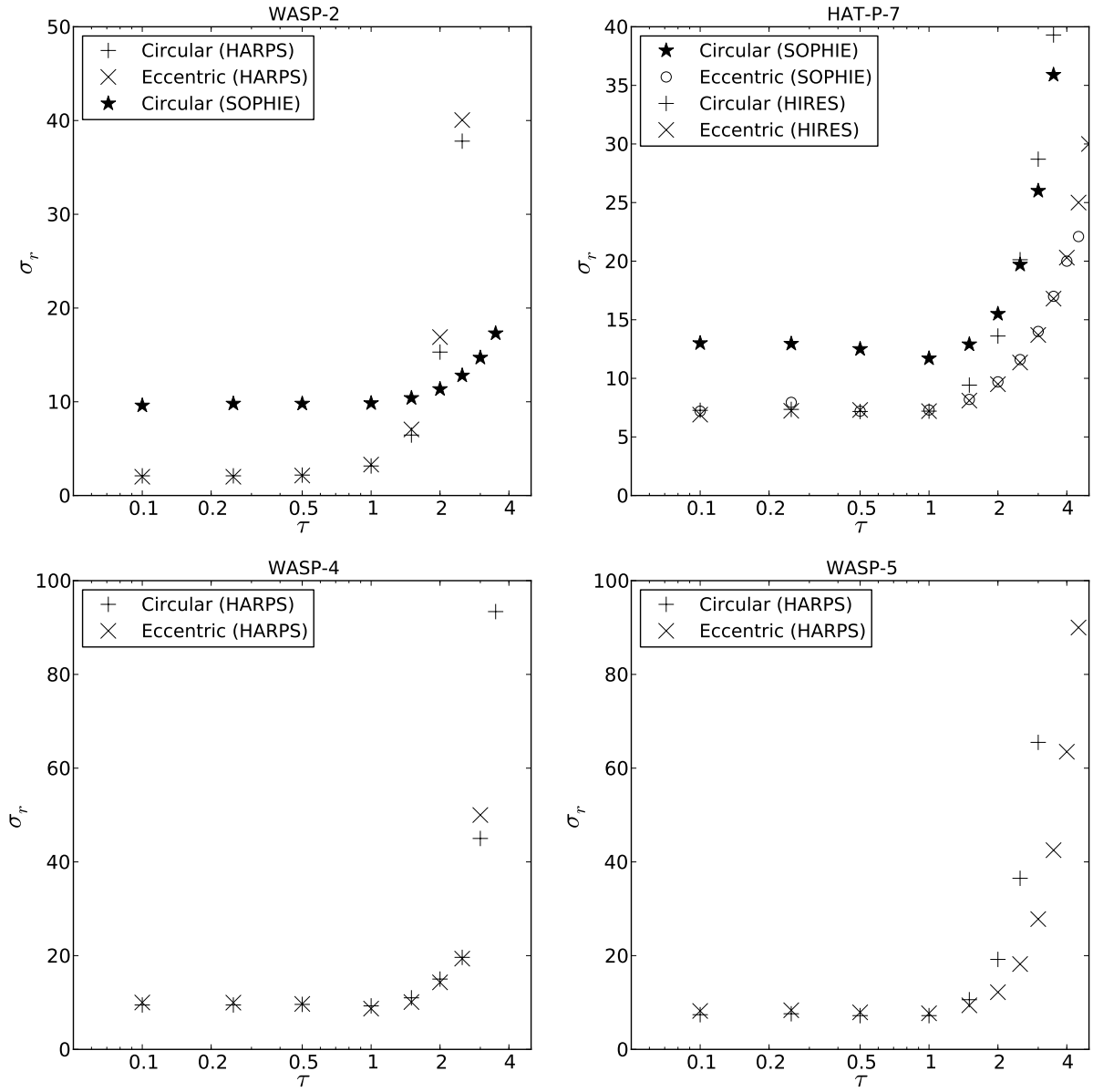

Figure 5.1: Plot showing the degeneracy between σ_r and τ for objects where the orbital parameters are well constrained (see Section 3.5) because a sufficient number of radial velocity measurements is available and provides sufficient phase coverage. The object being studied is shown in the title for each panel, and the instrument used for the measurements are shown in parenthesis. As can be seen on each plot, the optimal σ_r that gives a reduced χ^2 of unity for each dataset increases slowly with τ for $\tau < 1.5$ d, but increases faster after 1.5 d. This hints that the systematic effects occur on a timescale of 1.5 d, and could be related to the weather. Note the SOPHIE data for WASP-2 did not provide full phase coverage — the solution did not converge for an eccentric model and the knee at $\tau \sim 1.5$ d is less pronounced.

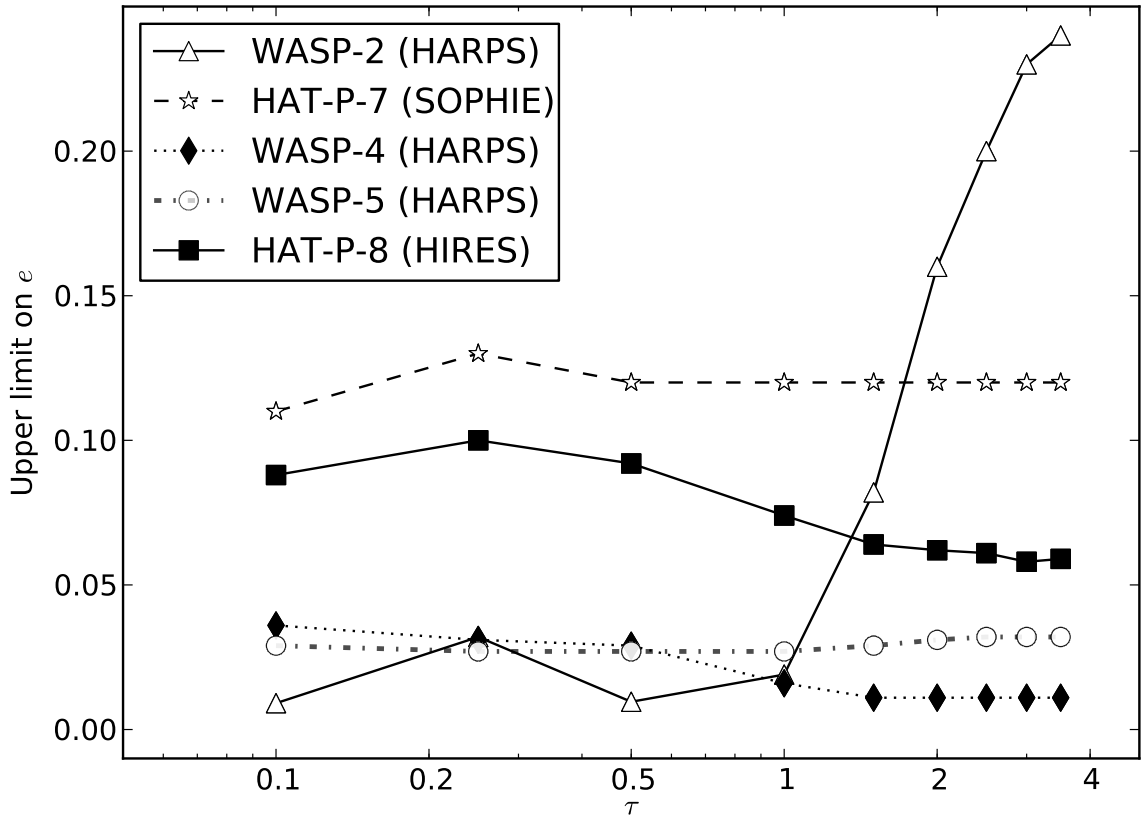

Figure 5.2: Plot showing the effect of varying τ on the 95% upper limit on the derived eccentricity for WASP-2, HAT-P-7, WASP-4 and WASP-5. Except for WASP-2, where the phase coverage of the HARPS data is incomplete (see Figure 5.10), varying τ has no effect on the 95% upper limit of the derived eccentricity for timescales of a few days, $\tau > 1.5$ d. Note: each line on this plot is made a single dataset.

et al. (2009) and obtained a value of $\chi^2_c = 15.97$ for the circular orbit and a value of $\chi^2_e = 13.50$ for the eccentric orbit ($e = 0.086^{+0.086}_{-0.054}$, $e < 0.26$). Using $N = 20$, $k = 3$ and $k = 5$ for the circular (two datasets, each with one V_0 and a single K) and eccentric orbits respectively, we obtained $\mathrm{BIC}_c = 151.05$ and $\mathrm{BIC}_e = 154.57$. A smaller value of BIC_c means the circular orbit cannot be excluded.

WASP-6

WASP-6b is a 0.50 M_j planet on a 3.36 day orbit around a G8 star (V=11.9), first reported by Gillon et al. (2009). Using 35 CORALIE measurements and 44 HARPS measurements (38 of which occur near or during a spectroscopic transit, which we ignore in this study), the authors derived a value of eccentricity $e = 0.054^{+0.018}_{-0.015}$. In our study, we used the 35 CORALIE measurements and the 6 HARPS measurements that were not taken in the single night where the spectroscopic transit was observed. We used $\sigma_r = 0$ m s^{-1} for CORALIE (the data produces a reduced $\chi^2 = 0.89$ when fitted with a circular orbit, indicating overfitting) but for HARPS we used $\tau = 1.5$ d and $\sigma_r = 4.15$ m s^{-1} to obtain a reduced χ^2 of unity for the circular orbit. We obtained a value of $\chi^2_c = 38.09$ for the circular orbit and a value of $\chi^2_e = 33.58$ for the eccentric orbit ($e = 0.041 \pm 0.019$, $e < 0.075$). Using $N = 43$ (41 RVs and two constraints from photometry), $k = 3$ and $k = 5$ for the circular (two datasets, each with one V_0 and a single K) and eccentric orbits respectively, we obtained $\mathrm{BIC}_c = 333.25$ and $\mathrm{BIC}_e = 336.27$. We repeated the calculations, using $\sigma_r = 0$ for CORALIE (the data produces a reduced $\chi^2 = 0.85$ when fitted with an eccentric orbit, indicating overfitting) but for HARPS we used $\tau = 1.5$ d and $\sigma_r = 3.59$ m s^{-1} to obtain a reduced χ^2 of unity for the eccentric orbit. We obtained a value of $\chi^2_c = 39.20$ for the circular orbit and a value of $\chi^2_e = 34.47$ for the eccentric orbit ($e = 0.043 \pm 0.019$, $e < 0.075$). Using $N = 43$, $k = 3$ and $k = 5$ for the circular and eccentric orbits respectively, we obtained $\mathrm{BIC}_c = 333.60$ and $\mathrm{BIC}_e = 336.39$. We therefore find that the circular orbital solution cannot be excluded, but the possibility that $e > 0.1$ is rejected.

WASP-10

WASP-10b is a 2.96 M_j planet on a 3.09 day orbit around a K5 star (V=12.7), first reported by Christian et al. (2009). Using 7 SOPHIE measurements and 7 FIES measurements, the authors derived a value of eccentricity $e = 0.059^{+0.014}_{-0.004}$. The FIES data yielded a reduced χ^2 less than unity with both eccentric and circular orbits, indicating overfitting, so we set $\sigma_r = 0$ m s^{-1}.

For the SOPHIE data, used $\tau = 1.5$ d, $\sigma_r = 54.5$ m s^{-1} to obtain a reduced χ^2 of unity for the circular orbit. We reanalysed all the radial velocity measurements, and applied the prior from photometry $P = 3.0927636(200)$ and $T_{tr} = 2454357.8581(4)$ from Christian et al. (2009). We obtained a value of $\chi^2_c = 13.49$ for the circular orbit and a value of $\chi^2_e = 7.47$ for the eccentric orbit ($e = 0.049 \pm 0.022$, less significant than the original claim). Using 14 measurements and two priors from photometry ($N = 16$), $k = 3$ and $k = 5$ for the circular (two datasets, each with one V_0 and a single K) and eccentric orbits respectively, we obtained $\mathrm{BIC}_c = 151.50$ and $\mathrm{BIC}_e = 151.01$. This now appears to show only a marginal support for an eccentric orbit.

We plotted the SOPHIE radial velocity data against time, as shown in Figure 5.3 and overplotted a circular orbit as well as an eccentric orbit. Due to the long time between the first two measurements and the last five, we plot them in

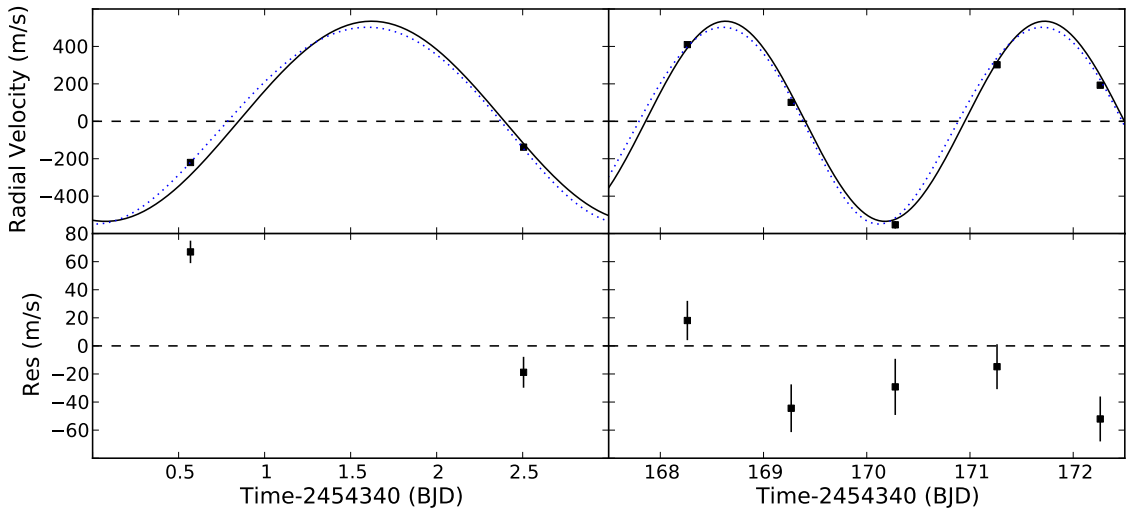

Figure 5.3: Plot showing SOPHIE radial velocity data from Christian et al. (2009) for WASP-10, plotted against time. The plot has been split along the time axis into two panels (left and right) to remove the 160 days without measurements, for clarity. A circular orbit (solid line) and an orbit with the best-fit eccentricity ($e = 0.048$) are overplotted. The residuals relative to the circular orbit are shown in the bottom panel.

separate panels, shown on the left and right respectively. It is clear that the first measurement is pulling the eccentricity upwards, and we suspect from experience that the long term drifts in the SOPHIE zero point in HE mode for faint targets could have affected the first two measurements. We therefore repeated our calculations using only the last five measurements from the SOPHIE dataset and the whole FIES dataset, and set $\sigma_r = 45.5$ m s^{-1} for SOPHIE. This time, we obtained a value of $\chi^2_c = 11.81$ for the circular orbit and a value of $\chi^2_e = 7.64$ for the eccentric orbit ($e = 0.043 \pm 0.035$). Using 12 measurements and two priors from photometry ($N = 14$), $k = 3$ and $k = 5$ for the circular (two datasets, each with one V_0 and a single K) and eccentric orbits respectively, we obtained $\mathrm{BIC}_c = 128.71$ and $\mathrm{BIC}_e = 129.83$, this time favouring the circular orbit. We repeated this calculation, and set $\sigma_r = 0$ m s^{-1} for both SOPHIE and FIES, as each dataset gave a reduced χ^2 of less than unity for the eccentric orbit (SOPHIE reduced $\chi^2 = 0.64$, FIES reduced $\chi^2 = 0.45$). This time, we obtained a value of $\chi^2_c = 19.30$ for the circular orbit and a value of $\chi^2_e = 10.65$ for the eccentric orbit ($e = 0.080 \pm 0.055$). Using 12 measurements and two priors from photometry ($N = 14$), $k = 3$ and $k = 5$ for the circular (two datasets, each with one V_0 and a single K) and eccentric orbits respectively, we obtained $\mathrm{BIC}_c = 128.33$ and $\mathrm{BIC}_e = 124.97$, this time favouring the eccentric orbit once again. It is therefore unclear to us whether or not the orbital eccentricity is non-zero as claimed in Christian et al. (2009).

Maciejewski et al. (2011), used transit timing variation analysis and reanalysed the radial velocity data, to obtain an eccentricity that is indistinguishable from zero ($e = 0.013 \pm 0.063$). They argued instead that the original detection of an eccentricity had been influenced by starspots. The difference between our value of eccentricity and that derived by Maciejewski et al. (2011) is probably due to the fact that the latter used a two planet model, which can reduce the derived eccentricity further — sparse sampling of the radial velocity from a two planet system can lead to an overestimated eccentricity.

WASP- 12
WASP- 12b is a 1.41 M_j planet on a 1.09 day orbit around a F9 star (V=11.7), first reported by Hebb et al. (2009). Using SOPHIE measurements, the original authors derived a value of eccentricity $e = 0.049 \pm 0.015$. As we showed in Chapter 4, new SOPHIE radial velocity measurements, as well as the original transit photometry from Hebb et al. (2009) and the secondary eclipse photometry from Campo et al. (2011) suggest that the eccentricity is in fact compatible with zero ($e = 0.017^{+0.015}_{-0.010}$) (Husnoo et al., 2011).

WASP-17
WASP-17b is a 0.50 M_j planet on a 3.74 day orbit around a F6 star (V=11.6), first reported by Anderson et al. (2010). Using 41 CORALIE measurements (three of which are during the spectroscopic transit, which we ignore in this study) and 3 HARPS measurements, the authors considered three cases: first imposing a prior on the mass M_* of the host star, secondly imposing a main-sequence prior on the stellar parameters and thirdly with a circular orbit. They derived values of eccentricity $e = 0.129^{+0.106}_{-0.068}$ and $e = 0.237^{+0.068}_{-0.069}$ for the first two cases respectively. We set $\sigma_r = 0$ for both HARPS and CORALIE since we obtained a reduced χ^2 of slightly less than unity for both eccentric and circular orbits for either dataset alone, indicating overfitting. We obtained a value of $\chi^2_c = 37.98$ for the circular orbit and a value of $\chi^2_e = 35.94$ for the eccentric orbit. Using 41 measurements and two priors from photometry ($N = 43$), $k = 3$ and $k = 5$ for the circular (two datasets, each with one V_0 and a single K) and eccentric orbits respectively, we obtained $\mathrm{BIC}_c = 399.31$ and $\mathrm{BIC}_e = 404.80$. We thus find that the circular orbit cannot be excluded, agreeing with the third case ($e = 0$, fixed) considered in Anderson et al. (2010) and rejecting the two derived values of eccentricity in that paper.

WASP-18
WASP-18b is a 10.3 M_j planet on a 0.94 day orbit around a F6 star (V=9.3), first reported by Hellier et al. (2009). Using 9 CORALIE measurements (we drop the third measurement in our final analysis, since it produces a 5-σ residual that is not improved by an eccentric orbit, suggesting that it is a genuine outlier), the authors derived a value of eccentricity $e = 0.0092 \pm 0.0028$. In our study, we set $\tau = 1.5$ d and $\sigma_r = 20.15$ m s^{-1} to obtain a reduced χ^2 of unity for the circular orbit. We obtained a value of $\chi^2_c = 8.17$ for the circular orbit and a value of $\chi^2_e = 6.64$ for the eccentric orbit ($e = 0.007 \pm 0.005$, $e < 0.018$). Using $N = 10$, $k = 2$ and $k = 4$ for the circular (one dataset, with one V_0 and a single K) and eccentric orbits respectively, we obtained $\mathrm{BIC}_c = 75.34$ and $\mathrm{BIC}_e = 78.41$. We repeated the calculations using $\sigma_r = 22.5$ m s^{-1} to obtain a reduced χ^2 of unity for the eccentric orbit. We obtained a value of $\chi^2_c = 7.14$ for the circular orbit and a value of $\chi^2_e = 6.00$ for the eccentric orbit ($e = 0.008 \pm 0.005$, $e < 0.019$). Using $N = 10$, $k = 2$ and $k = 4$ for the circular (one dataset, with one V_0 and a single K) and eccentric orbits respectively, we obtained $\mathrm{BIC}_c = 75.50$ and $\mathrm{BIC}_e = 78.97$. We thus find that the circular orbit cannot be excluded, in contrast to Hellier et al. (2009). The possibility that $e > 0.1$ is excluded.

WASP-5 (new HARPS data)
WASP-5b is a 1.6 M_j planet on a 1.63 day orbit around a G4 star (V=12.3), first

reported by Anderson et al. (2008). Gillon et al. (2009) used z-band transit photometry from the VLT to refine the eccentricity to $e = 0.038^{+0.026}_{-0.018}$, and the authors made a tentative claim for the detection of a small eccentricity. We analysed our 11 new HARPS measurements for WASP-5 and the 11 CORALIE RVs from Anderson et al. (2008) using the photometric constraints on the orbital period $P = 1.6284246(13)$ and mid-transit time $T_{tr} = 2454375.624956(24)$ from Southworth et al., 2009.

We use $\tau = 1.5$ d, $\sigma_r = 10.6$ m s^{-1} for HARPS and $\sigma_r = 4.3$ m s^{-1} for CORALIE to obtain a value of reduced χ^2 of unity for the circular orbit for each dataset separately. We ran the MCMC twice: the first time fitting for the systemic velocity v_0 and semi-amplitude K, and the second time adding two parameters $e\cos\omega$ and $e\sin\omega$ to allow for an eccentric orbit. The best fit result is shown in Figure 5.4. The residuals for a circular orbit are plotted, and a signal is clearly present in the residuals. The value of χ^2 for the circular orbit is 24.36 and that for an eccentric orbit is 20.57. This results in a value of BIC$_c$ = 169.40 for the circular orbit and BIC$_e$ = 171.97 for the eccentric orbit, given 22 measurements, 2 constraints from photometry and 3 and 5 free parameters respectively for each model.

We repeated the above analysis using $\tau = 1.5$ d, $\sigma_r = 9.4$ m s^{-1} for the HARPS dataset to obtain a value of reduced χ^2 of unity for the eccentric orbit and $\sigma_r = 0$ m s^{-1} for CORALIE (which resulted in a reduced χ^2 of 0.58). This time, we obtained a value of χ^2 for the circular orbit is 27.35 and that for an eccentric orbit is 23.00. This leads to a value of BIC$_c$ = 170.37 for the circular orbit and BIC$_e$ = 172.38 for the eccentric orbit. Once again, the circular orbit is favoured.

A keplerian model, circular or eccentric ($e = 0.012 \pm 0.007$) does not account for the scatter in the data the HARPS dataset as shown in Figure 5.4. We have therefore plotted the radial velocity measurements, the bisector span, the signal to noise at order 49, the contrast and full width at half maximum for the cross-correlation function against the same time axis. The trend in radial velocity residuals can be seen to be correlated with both the bisector span and the full width at half maximum of the cross correlation function. This suggests a line shape change that is related to either weather effects or instrumental systematics. The timescale of this variation is compatible with both scenarios. The bisector inverse span is generally directly correlated with the residuals, which weighs against a scenario involving stellar activity, but this is not so clear for the first three measurements — the drift could be due to stellar activity or an additional planetary or stellar companion.

We extended the model with a linear acceleration of the form described in Equation 4.1 and fitted the HARPS data alone using $t_0 = 2454768$ (to allow the MCMC to explore values of $\dot{\gamma}$ more efficiently) and reran the MCMC twice: once for a circular orbit and once for an eccentric orbit. Firstly, we used $\sigma_r = 10.6$ m s^{-1} for the HARPS dataset, and the linear trend for a circular orbit resulted in $\dot{\gamma} = -2.6 \pm 2.9$ m s^{-1} yr^{-1} and that for an eccentric orbit is $\dot{\gamma} = -2.0 \pm 2.9$ m s^{-1} yr^{-1}. The best fit result is shown in Figure 5.5 and the residuals for a circular orbit are plotted in the bottom panel. The value of χ^2 for the circular orbit is 10.24 and that for an eccentric orbit is 7.70. This results in a value of BIC$_{c,lin}$ = 71.91 for the circular orbit and BIC$_{e,lin}$ = 74.49 for the eccentric orbit, given 11 (N=13) measurements, 2 constraints from photometry and 3 and 5 free parameters respectively for each model. We repeated these calculations

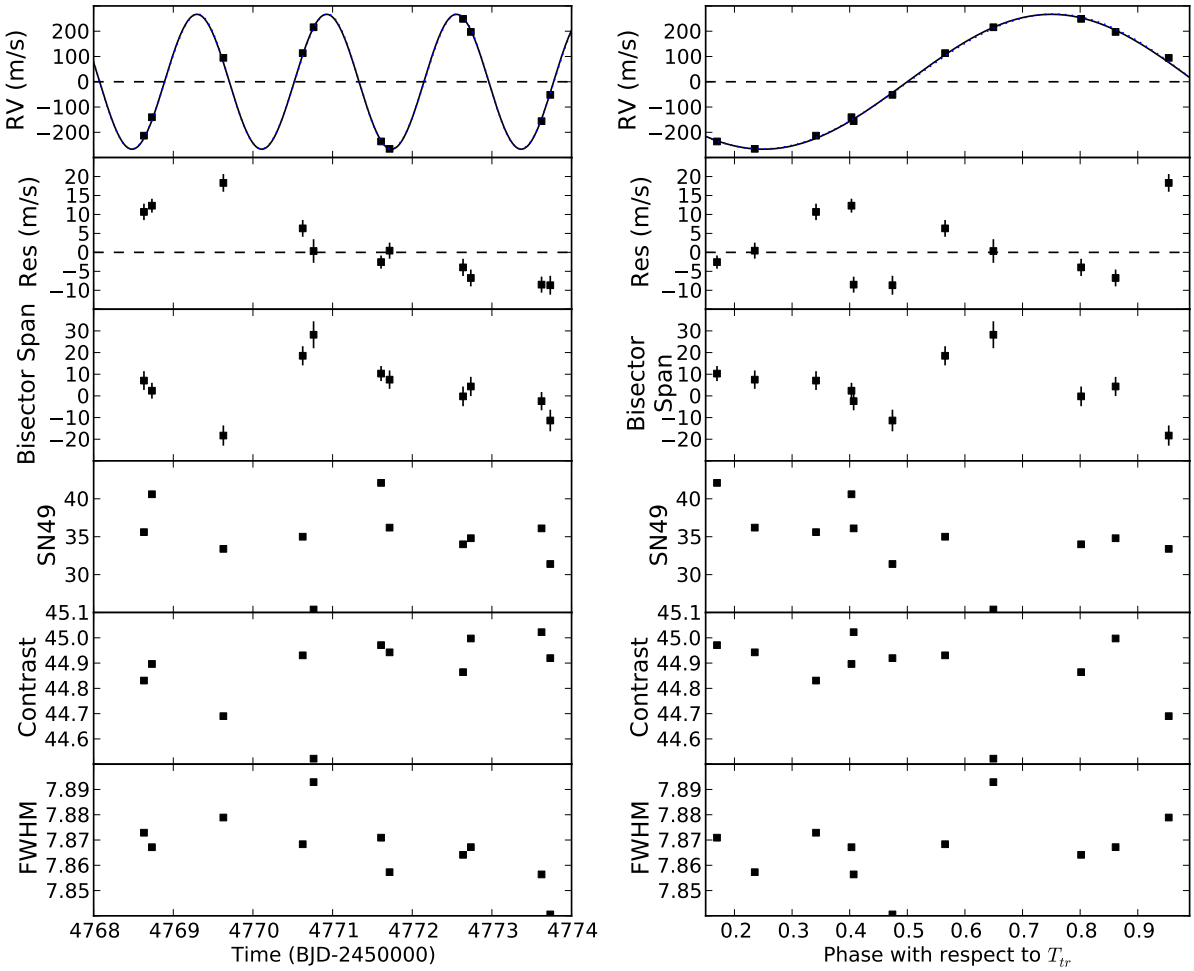

Figure 5.4: HARPS measurements of WASP-5 plotted against time (**left**) and phase with respect to the mid-transit time T_{tr} (**right**). In each case, a solid line is overplotted to represent a circular orbit and the residuals are plotted for this circular orbit. It is clear that a signal is present in the residuals (see text). An eccentric orbit with the best-fit value of $e = 0.012$ is overplotted in both panels with a dotted line, but it is indistinguishable from the circular solution at this scale. Note the trend that is apparent in the residuals (second panel from the top on both the time and phase plots). We correct for this using a linear acceleration term in our model (see Figure 5.5).

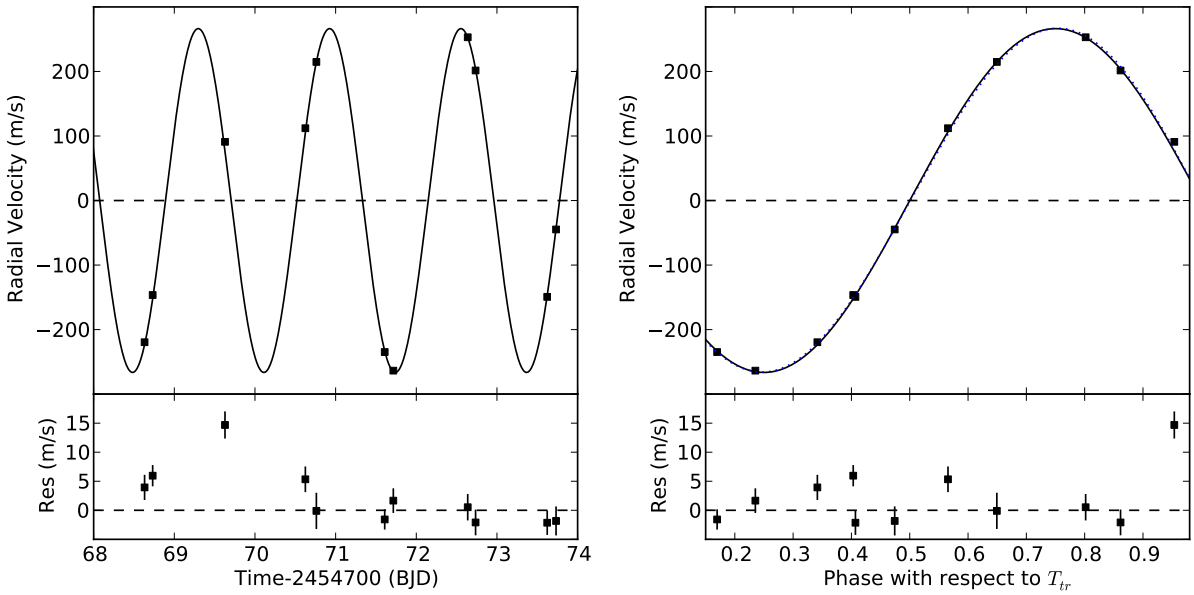

Figure 5.5: HARPS measurements of WASP-5 plotted against time (**left**) and phase with respect to the mid-transit time T_{tr} (**right**). In each case, a solid line is overplotted to represent a circular orbit and the residuals are plotted for this circular orbit. A model for an eccentric orbit with the best-fit value of $e = 0.013$ is overplotted in both panels with a dotted line, but it is indistinguishable from the circular solution at this scale. Both include the linear trend (see Section 5.4 and Figure 5.4).

using $\sigma_r = 9.4$ m s^{-1} for the HARPS dataset, and the linear trend for a circular orbit resulted in $\dot{\gamma} = -3.7 \pm 1.3$ m s^{-1} yr^{-1} and that for an eccentric orbit is $\dot{\gamma} = -3.3 \pm 1.3$ m s^{-1} yr^{-1}. The value of χ^2 for the circular orbit is 15.46 and that for an eccentric orbit is 13.50. This leads to a value of $\mathrm{BIC}_{c,lin} = 69.72$ for the circular orbit and $\mathrm{BIC}_{e,lin} = 72.89$ for the eccentric orbit. The circular orbit is not excluded, and the possibility that $e > 0.1$ is excluded. The results for both models, one including the linear trend but excluding the CORALIE data, and one including the CORALIE data but excluding the linear trend are shown in Table 5.2. In both cases, we give results for the case where σ_r is chosen to yield a reduced χ^2 of unity for the circular orbit. We attempted to repeat this using both the CORALIE and HARPS datasets, but we were unable to obtain a fit with the MCMC, because of the long time scale between the two datasets.

5.4 Planets on circular orbits

We establish that 20 planets have orbital eccentricities compatible with zero and the 95% upper limits are smaller than $e_{95} = 0.1$. In this Section, we describe the planets WASP-4b, HAT-P-7b, TrES-2 and WASP-2b, for which we introduce new RVs. We also establish that the 95% upper limits on the eccentricities of WASP-5b, WASP-12b and WASP-18b, which have been described in Section 5.3 above. In addition, we give the 95% upper limits on the eccentricities of CoRoT-1b, CoRoT-3b, HAT-P-8b, WASP-3b, WASP-16b, WASP-19b, WASP-22b, WASP-26b and XO-5b in Table 5.1. We discuss the evidence for circular orbits for HAT-P-13b, HD189733b, HD209458b and Kepler-5b at the end of this section.

Parameter	Anderson et al.	HARPS only *this work* (with linear trend)	HARPS & CORALIE *this work* (no linear trend)
Centre-of-mass velocity V_0 [m s^{-1}]	20010.5±3.4	20018±12	20009.9±7.4 (HARPS)
Orbital eccentricity e	0 (adopted)	0.013 ± 0.008 (< 0.029)	0.012 ± 0.007 (< 0.026)
Argument of periastron ω [^{o}]	0 (unconstrained)	0 (unconstrained)	0 (unconstrained)
$e \cos \omega$	–	0.002±0.003	0.003±0.003
$e \sin \omega$	–	0.012±0.010	0.011±0.009
Velocity semi-amplitude K [m s^{-1}]	277.8±7.8	266.4±1.3	266.9±1.3

Table 5.2: System parameters for WASP-5. Left: Anderson et al. (2008). Right: Results from our HARPS radial velocity data alone, and results from using both our HARPS data and the original CORALIE data in Anderson et al. (2008). Median values for V_0 and K are quoted for the circular orbits, as well as 68.3% confidence limits obtained from the eccentric solution (see section Analysis).

WASP-4 (new HARPS data)

WASP-4b is a 1.2 M_j planet on a 1.34 day orbit around a G7 star (V=12.5), first reported by Wilson et al. (2008). We analysed our 14 new HARPS measurements and the 14 CORALIE measurements from Wilson et al. (2008) for WASP-4 and used the photometric constraints on the orbital period $P = 1.33823214(71)$ and mid-transit time $T_{tr} = 2454697.797562(43)$ from Winn et al. (2009b).

We estimate $\tau = 1.5$ d, $\sigma_r = 11$ m s^{-1} for the HARPS dataset and $\sigma_r = 4.5$ m s^{-1} for the CORALIE dataset to obtain a reduced χ^2 of unity for a circular orbit for each dataset separately. We ran the MCMC twice: the first time fitting for the systemic velocity v_0 and semi-amplitude K only, ie. a circular orbit ($k = 2$), and the second time adding two parameters $e \cos \omega$ and $e \sin \omega$ to allow for an eccentric orbit ($k = 4$). The best fit result is shown in Figure 5.6. The residuals for a circular orbit are plotted, and a signal is clearly present in the residuals. The value of χ^2 for the circular orbit is 27.13 and that for an eccentric orbit is 24.32. This leads to a value of $\mathrm{BIC}_c = 208.62$ for the circular orbit and $\mathrm{BIC}_e = 212.55$ for the eccentric orbit, given 14 measurements, 2 constraints from photometry and 2 and 4 free parameters respectively for each model.

We repeated the calculations, estimating $\tau = 1.5$ d, $\sigma_r = 10.1$ m s^{-1} for the HARPS dataset and $\sigma_r = 7.1$ m s^{-1} for the CORALIE dataset to obtain a reduced χ^2 of unity for an eccentric orbit for each dataset separately. The value of χ^2 for the circular orbit is 27.29 and that for an eccentric orbit is 24.33. This leads to a value of $\mathrm{BIC}_c = 208.72$ for the circular orbit and $\mathrm{BIC}_e = 212.51$.

Note the trend that is apparent in the residuals in Figure 5.6. We have therefore plotted the radial velocity measurements, the bisector span, the signal to noise at order 49, the contrast and full width at half maximum for the cross-correlation function against the same time axis. For most measurements, the trend in radial velocity residuals can be seen to be correlated with both the bisector span and the full width at half maximum of the cross correlation function. This suggests a line shape change that is related to either stellar activity, weather effects or instrumental systematics. The timescale of this variation is compatible with all three scenarios.

We repeated the calculations for the HARPS dataset alone, and added a linear component to the radial velocity model in the same way we did for WASP-5 in Section 5.3 and we set $t_0 = 2454762$ (to allow the MCMC to explore values of $\dot{\gamma}$ more efficiently) and reran the MCMC twice: once for a circular orbit and once

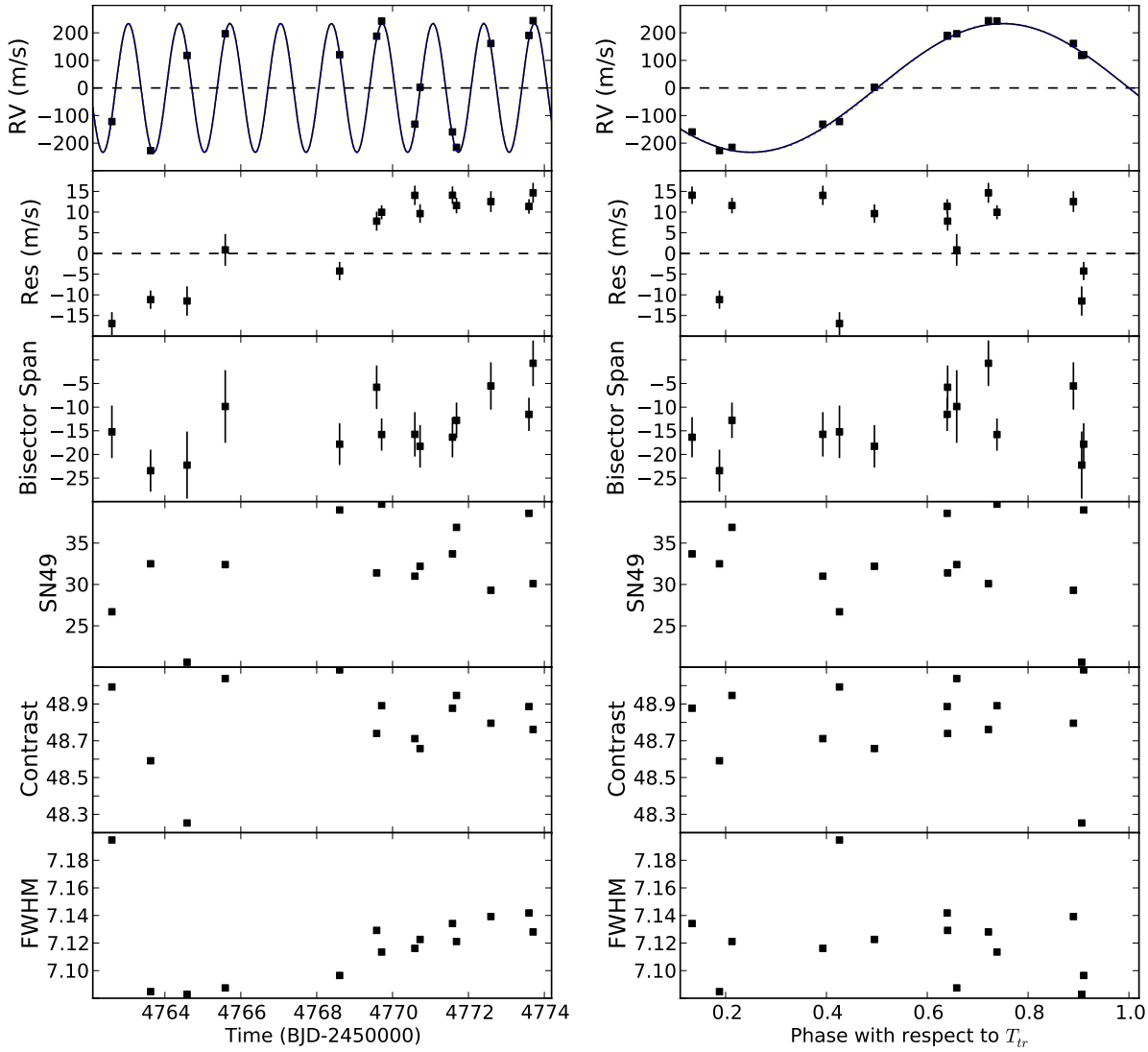

Figure 5.6: HARPS measurements of WASP-4 plotted against time (**left**) and phase with respect to the mid-transit time T_{tr} (**right**). In each case, a solid line is overplotted to represent a circular orbit and the residuals are plotted for this circular orbit. It is clear that a signal is present in the residuals (see text). An eccentric orbit with the best-fit value of $e = 0.005$ is overplotted in both panels with a dotted line, but it is indistinguishable from the circular solution at this scale. Note the trend that is apparent in the residuals (second panel from the top on both images). We attempt to correct for this by repeating our calculations with a linear acceleration term in the model (see Section 5.4 and Figure 5.7).

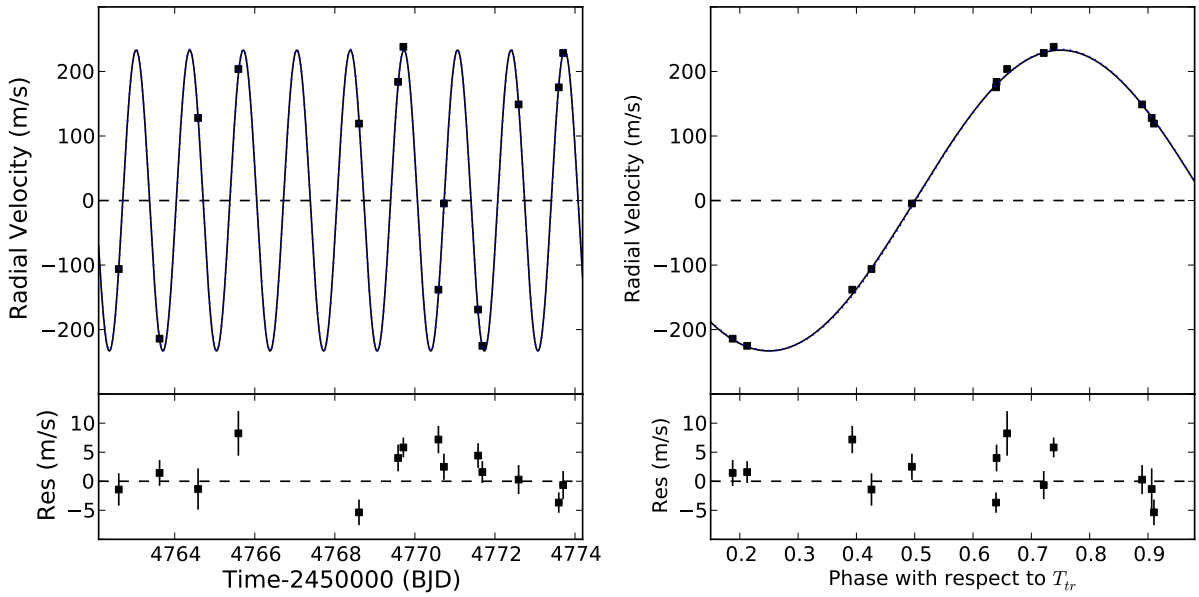

Figure 5.7: HARPS measurements of WASP-4 plotted against time (**left**) and phase with respect to the mid-transit time T_{tr} (**right**). In each case, a solid line is overplotted to represent a circular orbit and the residuals are plotted for this circular orbit. It is clear that a signal is present in the residuals (see text). An eccentric orbit with the best-fit value of $e = 0.004$ is overplotted in both panels with a dotted line, but it is indistinguishable from the circular solution at this scale. The linear trend from Figure 5.6 has now been included in the model.

for an eccentric orbit. We set $\tau = 1.5$ d and $\sigma_r = 11$ m s^{-1} for the HARPS dataset.

The best fit result is shown in Figure 5.7. The residuals for a circular orbit are plotted, and a signal is clearly present in the residuals. The linear trend for a circular orbit results in $\dot{\gamma} = 1023 \pm 490$ m s^{-1} yr^{-1} and that for an eccentric orbit is $\dot{\gamma} = 919 \pm 500$ m s^{-1} yr^{-1}.

The value of χ^2 for the circular orbit is 9.83 and that for an eccentric orbit is 7.51. This leads to a value of BIC$_c$ = 92.02 for the circular orbit and BIC$_e$ = 95.26 for the eccentric orbit, given 14 measurements, 2 constraints from photometry and 3 and 5 free parameters respectively for each model.

We repeated the calculations, setting $\tau = 1.5$ d, $\sigma_r = 10.05$ m s^{-1} for the HARPS dataset. The value of χ^2 for the circular orbit is 10.30 and that for an eccentric orbit is 8.07. This leads to a value of BIC$_c$ = 91.18 for the circular orbit and BIC$_e$ = 94.49. In all cases, the circular orbit is not excluded. The results for both models, one including the linear trend but excluding the CORALIE data, and one including the CORALIE data but excluding the linear trend are shown in Table 5.3. In both cases, we give results for the case where σ_r is chosen to yield a reduced χ^2 of unity for the circular orbit. We reject the possibility that $e > 0.1$.

HAT-P-7 (new SOPHIE data)

HAT-P-7b is a 1.8 M$_j$ planet on a 2.20 day orbit around an F6 star (V=10.5), first reported by Pál et al. (2008). We use 13 new SOPHIE radial velocity measurements and 16 out of the 17 HIRES measurements in Winn et al. (2009a) (we drop one in-transit measurement) to work out the orbital parameters of HAT-P-7b. We impose the period $P = 2.204733(10)$ d as given from photometry in Welsh et al. (2010) and mid-transit time $T_{tr} = 2454731.67929(43)$ BJD as given

Parameter	Wilson et al. (2008)	HARPS only *this work* (with linear trend)	HARPS & CORALIE *this work* (no linear trend)
Centre-of-mass velocity V_0 [m s^{-1}]	57733±2	57773±10	57790.8±5.7
Orbital eccentricity e	0 (adopted)	0.004 ± 0.003 (<0.011)	0.005 ± 0.003 (<0.011)
Argument of periastron ω [^{o}]	0 (unconstrained)	0 (unconstrained)	0 (unconstrained)
$e \cos \omega$	–	0.004±0.003	0.003±0.003
$e \sin \omega$	–	−0.002±0.004	−0.004±0.004
Velocity semi-amplitude K [m s^{-1}]	240±10	233.1±2.1	233.7±2.0

Table 5.3: System parameters for WASP-4. Left: Wilson et al. (2008). Right: Results from our HARPS radial velocity data alone, and results from using both our HARPS data and the original CORALIE data in Wilson et al. (2008). Median values for V_0 and K are quoted for the circular orbits, as well as 68.3% confidence limits obtained from the eccentric solution (see section Analysis).

Parameter	HIRES, Winn et al. (2009a)	HIRES+SOPHIE, *this work*
Centre-of-mass velocity V_0 [m s^{-1}]	−51.2±3.6	−49.96±6.0 (HIRES) −10510±10 (SOPHIE)
Orbital eccentricity e	$e_{99\%}$ <0.039	0.014±0.010 ($e < 0.038$)
Argument of periastron ω [^{o}]	–	0 (unconstrained)
$e \cos \omega$	−0.0019±0.0077	−0.007±0.004
$e \sin \omega$	0.0037±0.0124	−0.011±0.015
Velocity semi-amplitude K [m s^{-1}]	211.8±2.6	213.8±1.2
Constant radial acceleration $\dot{\gamma}$ [m s^{-1}yr^{-1}]	21.5±2.6	21.1±4.2

Table 5.4: System parameters for HAT-P-7. Left: Winn et al. (2009a). Right: Results from our SOPHIE radial velocity data. Median values for V_0 and K are quoted for the circular orbits, as well as 68.3% confidence limits obtained from the eccentric solution. The upper 95% limit is also given for the eccentricity from our analysis.

from photometry in Winn et al. (2009a). We set $\tau = 1.5$ d, $\sigma_r = 9.41$ m s^{-1} for HIRES and $\sigma_r = 12.9$ m s^{-1} for SOPHIE to obtain a reduced χ^2 of unity for the best-fit circular orbit for each dataset separately. We used 29 measurements in all, and count the two constraints from photometry as two additional data points to obtain $N = 31$, and used $k = 4$ for the circular orbit (two V_0, one for each dataset, the semi-amplitude K and a constant drift term $\dot{\gamma}$, since Winn et al. (2009a) found evidence for a distant companion in the system and we set $t_0 = 2454342$). We repeated this analysis with an eccentric orbit $k = 6$ (4 degrees of freedom for the circular orbit with two datasets and a linear acceleration, and 2 additional degrees of freedom for the eccentricity, $e \cos \omega$ and $e \sin \omega$). The orbital parameters are given in Table 5.4, and the radial velocity dataset is plotted in Figure 5.8, with residuals shown for a circular orbit. The Figure also shows models of a circular and an eccentric orbit (with $e = 0.014$), but they are almost undistinguishable. For the circular orbit, we obtained $\chi^2 = 26.94$, and a value of $\mathrm{BIC}_c = 222.81$ and for the eccentric orbit, we obtained $\chi^2 = 23.98$ and a value of $\mathrm{BIC}_e = 226.72$. We repeated the calculations and set $\tau = 1.5$ d, $\sigma_r = 8.2$ m s^{-1} for HIRES and $\sigma_r = 8.2$ m s^{-1} for SOPHIE to obtain a reduced χ^2 of unity for the best-fit eccentric orbit. For the circular orbit, we obtained $\chi^2 = 35.65$ and a value of $\mathrm{BIC}_c = 224.14$ and for the eccentric orbit, we obtained $\chi^2 = 31.89$ and a value of $\mathrm{BIC}_e = 227.25$. We therefore find that the circular orbit cannot be excluded for HAT-P-7b. Further, we exclude the possibility that $e > 0.1$.

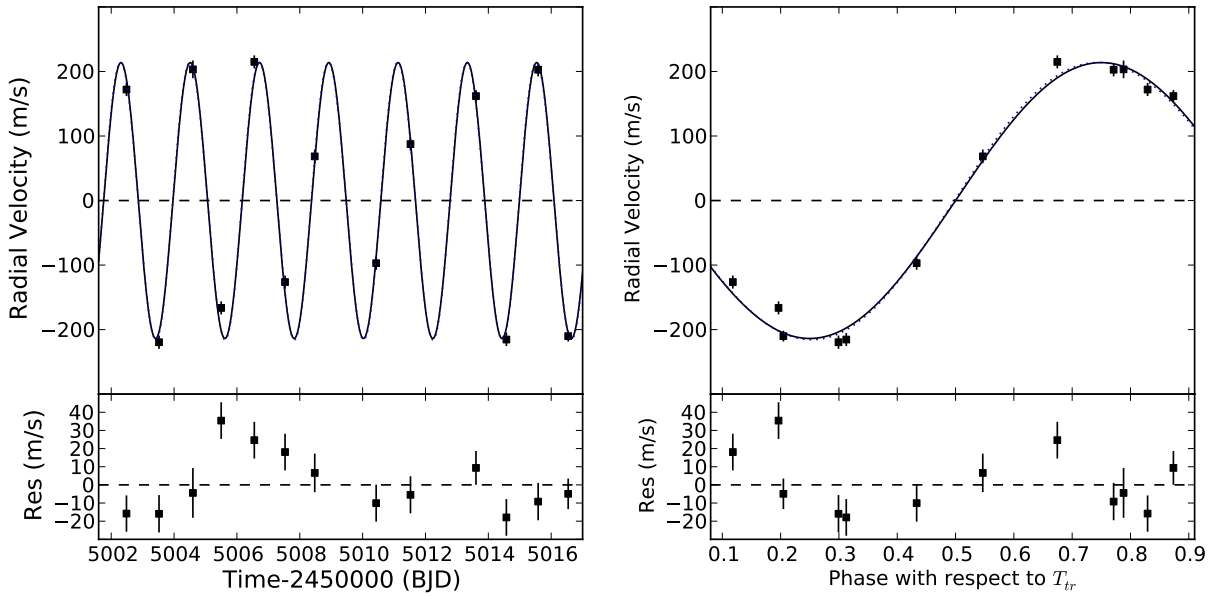

Figure 5.8: Plot showing our new SOPHIE radial velocity data for HAT-P-7, plotted against time (left), and orbital phase (right) with respect to T_{tr}. A circular orbit (solid line) and an orbit with the best-fit eccentricity (dotted line, but almost undistinguishable from the circular solution since $e = 0.014$) are overplotted. The residuals relative to the circular orbit are shown in the bottom panels.

TrES-2 (new SOPHIE data)

TrES-2b is a 1.3 M_j planet on a 2.47 day orbit around a G0 star (V=11.4), first reported by O'Donovan et al. (2006). We use 10 new SOPHIE radial velocity measurements and the 11 HIRES measurements in O'Donovan et al. (2006) to work out the orbital parameters of TrES-2b. We impose the period $P = 2.470614(1)$ d and mid-transit time $T_{tr} = 2453957.63492(13)$ BJD as given from photometry in Raetz et al. (2009).

We set $\tau = 1.5$ d and $\sigma_r = 6.8$ m s^{-1} for SOPHIE to obtain a reduced χ^2 of unity for the best-fit circular orbit (using the SOPHIE data alone), and set $\sigma_r = 0$m s^{-1} for the HIRES data since a circular orbit for that dataset alone yields a reduced χ^2 of 0.72, indicating over-fitting. We used 21 measurements in all, and count the two constraints from photometry as two additional datapoints to obtain $N = 23$, and used $k = 3$ for the circular orbit (two V_0, one for each dataset, and the semi-amplitude K). We repeated this analysis with an eccentric orbit $k = 5$ (three degrees of freedom for the circular orbit, and two additional degrees of freedom for the eccentricity, $e\cos\omega$ and $e\sin\omega$). The orbital parameters are given in Table 5.5, and the radial velocity dataset is plotted in Figure 5.9, with residuals shown for a circular orbit. The Figure also shows models of a circular and an eccentric orbit (with $e = 0.023$), but they are almost undistinguishable. For the circular orbit, we obtained $\chi^2 = 18.00$, yielding a value of $\mathrm{BIC}_c = 160.30$ and for the eccentric orbit, we obtained $\chi^2 = 15.91$ and a value of $\mathrm{BIC}_e = 164.48$. We repeated the calculations and set $\sigma_r = 8.45$ m s^{-1} for SOPHIE to obtain a reduced χ^2 of unity for the best-fit circular orbit (using the SOPHIE data alone), while we set $\sigma_r = 0$m s^{-1} for the HIRES data since an eccentric orbit for that dataset alone yields a reduced χ^2 of 0.56, indicating over-fitting. For a circular orbit, we obtained $\chi^2 = 15.97$, resulting in a value of $\mathrm{BIC}_c = 159.38$ and for an eccentric

Parameter	HIRES, O'Donovan et al. (2006)	HIRES, SOPHIE, *this work*
Centre-of-mass velocity V_0 [m s^{-1}]	–	-29.8 ± 2.4 (HIRES) -315.5 ± 5.0 (SOPHIE)
Orbital eccentricity e	0 (adopted)	0.023 ± 0.014, $e < 0.051$
Argument of periastron ω [^{o}]	0 (unconstrained)	0 (unconstrained)
$e \cos\omega$	–	0.002 ± 0.009
$e \sin\omega$	–	-0.022 ± 0.016
Velocity semi-amplitude K [m s^{-1}]	181.3 ± 2.6	181.1 ± 2.5

Table 5.5: System parameters for TrES-2. Left: O'Donovan et al. (2006). Right: Results from our HARPS radial velocity data. Median values for V_0 and K are quoted for the circular orbits, as well as 68.3% confidence limits obtained from the eccentric solution. The 95% limit on the eccentricity is also given.

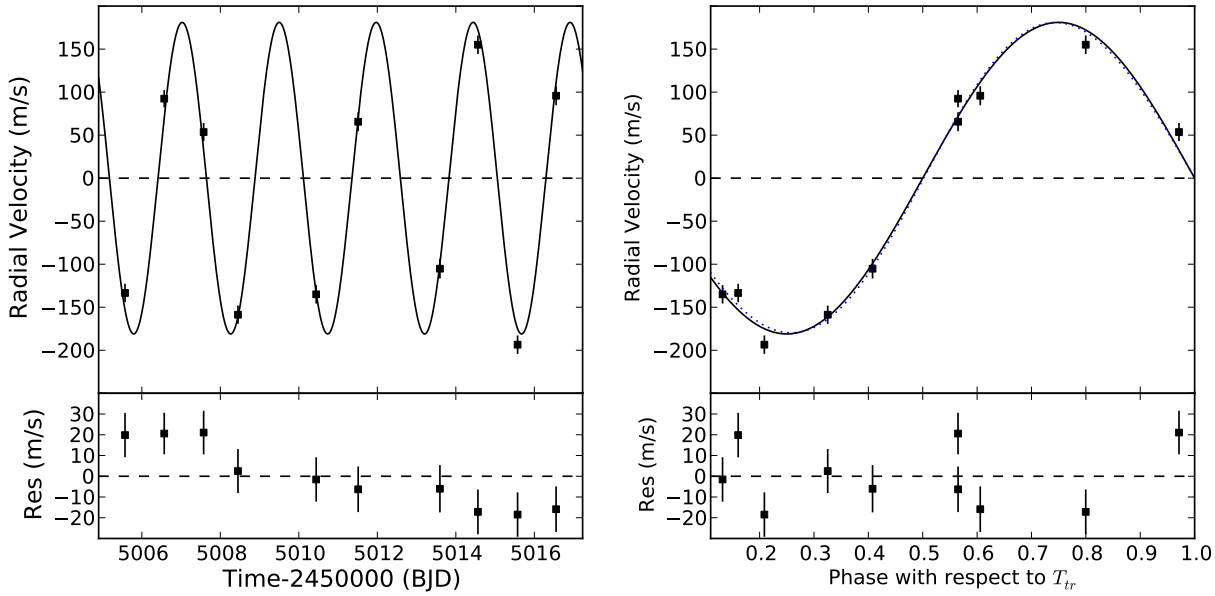

Figure 5.9: Plot showing our new SOPHIE radial velocity data for TrES-2, plotted against time (left) and orbital phase with respect to T_{tr} (right). A circular orbit (solid line) and an orbit with the best-fit eccentricity (dotted line, but almost undistinguishable from the circular solution since $e = 0.023$) are overplotted. The residuals relative to the circular orbit are shown in the bottom panel.

orbit, we obtained $\chi^2 = 13.88$ and a value of $\mathrm{BIC}_e = 163.56$. We therefore find that the circular orbit cannot be excluded for TrES-2b. Furthermore, we exclude the possibility that $e > 0.1$.

WASP-2 (new HARPS data)

WASP-2b is a 0.85 M_j planet on a 2.15 day orbit around a K1 star (V=12), first reported by Collier Cameron et al. (2007). We use 8 new HARPS radial velocity measurements and 7 of the original 9 SOPHIE measurements (we drop the first measurement, which has an uncertainty about 15 times larger than the rest, and the fifth, which shows a 3-σ deviation at a phase close to the transit) in Collier Cameron et al. (2007) to work out the orbital parameters of WASP-2b. We impose the period $P = 2.15222144(39)$ d and mid-transit time $T_{tr} = 2453991.51455(17)$ BJD as given from photometry in Southworth et al. (2010). We used 15 measurements in all, and count the two constraints from photometry as two additional datapoints ($N = 17$) and used $k = 3$ for the circular orbit (two V_0, one for each

Parameter	SOPHIE, Collier Cameron et al. (2007)	SOPHIE and HARPS, *this work*
Centre-of-mass velocity V_0 [m s^{-1}]	−27863±7	−27862±7.4 (SOPHIE) −27739.81±4.1 (HARPS)
Orbital eccentricity e	0 (adopted)	0.027±0.023 (<0.072)
Argument of periastron ω [^{o}]	0 (unconstrained)	0 (unconstrained)
$e\cos\omega$	–	−0.003±0.003
$e\sin\omega$	–	−0.027±0.027
Velocity semi-amplitude K [m s^{-1}]	155±7	156.3±2.1

Table 5.6: System parameters for WASP-2. Left: Collier Cameron et al. (2007). Right: Results from our HARPS radial velocity data. Median values for V_0 and K are quoted for the circular orbits, as well as 68.3% confidence limits obtained from the eccentric solution (see section Analysis) and 95% limit on eccentricity.

dataset, and the semi-amplitude K).

We estimated the timescale of correlated noise for both the HARPS and SOPHIE data to be $\tau = 1.5$ d, and we estimated $\sigma_r = 10.4$ m s^{-1} for the SOPHIE data and $\sigma_r = 6.45$ m s^{-1} for the HARPS data to obtain a reduced χ^2 of unity for the circular orbit. We repeated this analysis with an eccentric orbit $k = 5$ (3 degrees of freedom for the circular orbit, and 2 additional degrees of freedom for the eccentricity, $e\cos\omega$ and $e\sin\omega$). The orbital parameters are given in Table 5.6, and the radial velocity dataset is plotted in Figure 5.10, with residuals shown for a circular orbit. The Figure also shows models of a circular and an eccentric orbit (with $e = 0.027$), but they are almost undistinguishable. For the circular orbit, we obtained $\chi^2 = 15.60$, giving a value of BIC$_c$ = 115.08 and for the eccentric orbit, we obtained $\chi^2 = 13.88$ giving a value of BIC$_e$ = 119.02. We repeated these calculations to obtain a reduced χ^2 of unity for the eccentric orbit and estimated $\sigma_r = 10.4$ m s^{-1} for the SOPHIE data (the SOPHIE dataset did not allow the MCMC to converge and yield a reduced χ^2 of unity with an eccentric orbit) and $\sigma_r = 7.05$ m s^{-1} for the HARPS data. For the circular orbit, we obtained $\chi^2 = 15.16$, and a value of BIC$_c$ = 115.47 and for the eccentric orbit, we obtained $\chi^2 = 13.49$ and a value of BIC$_e$ = 119.47. We therefore find that the circular orbit cannot be excluded for WASP-2. Furthermore, we exclude the possibility that $e > 0.1$.

5.5 Planets on eccentric orbits

In contrast to Section 5.3, in this Section, we confirm the eccentricities of 10 planets. We verify the eccentricities of CoRoT-9b, GJ-436b and HAT-P-2b as a test for our procedures and we also confirm the eccentricities of HAT-P-16b and WASP-14b, with the former being the planet on a short period orbit with the smallest confirmed eccentricity, and the latter being the planet with the shortest period orbit having a confirmed eccentricity. Finally we note the confirmed orbital eccentricities of CoRoT-10b, HAT-P-15b, HD17156b, HD80606b and XO-3b.

CoRoT-9

CoRoT-9b is a 0.84 M$_j$ planet on a 95.3 day orbit around a G3 star (V=13.5), first reported by Deeg et al. (2010), who found an eccentricity of $e = 0.11 \pm 0.04$. We used the 14 HARPS measurements from Deeg et al. (2010), setting $\tau = 1.5$ d and $\sigma_r = 3.7$ m s^{-1} to obtain a value of reduced χ^2 of unity for the circular

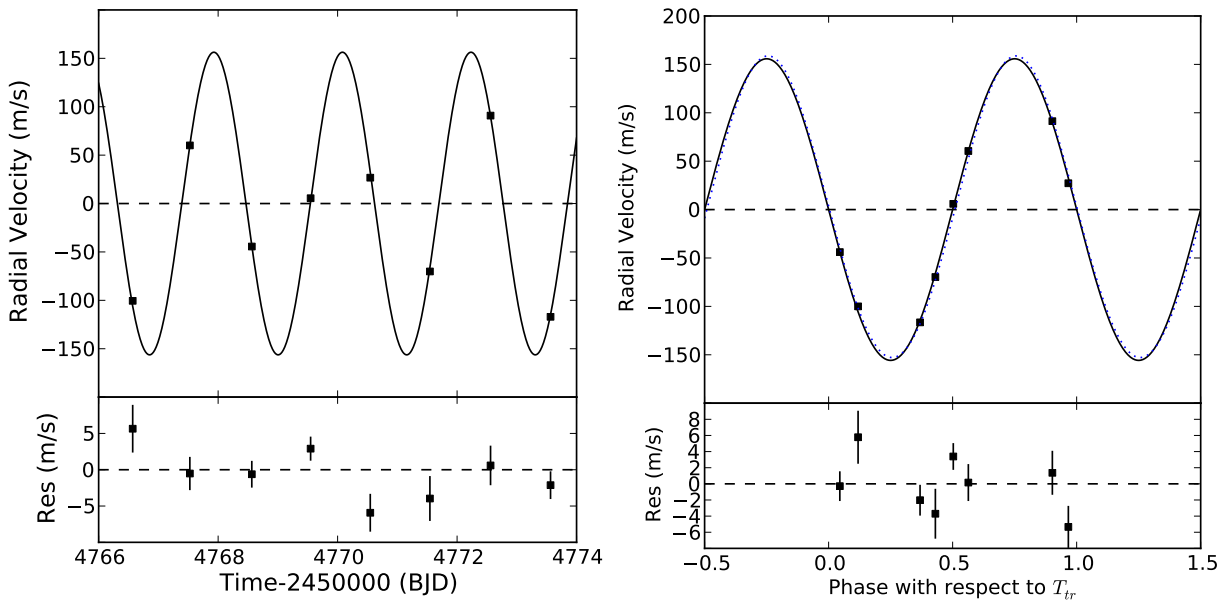

Figure 5.10: Plot showing our new HARPS radial velocity data for WASP-2, plotted against time (left) and orbital phase with respect to T_{tr} (right). A circular orbit (solid line) and an orbit with the best-fit eccentricity (dotted line, but almost undistinguishable from the circular solution since $e = 0.027$) are overplotted. The residuals relative to the circular orbit are shown in the bottom panel.

orbit. We imposed the prior information from photometry $P = 95.2738(14)$ and $T_{tr} = 2454603.3447(1)$ from Deeg et al. (2010) and obtained a value of $\chi^2_c = 14.05$ and $\chi^2_e = 7.90$. Using $N = 16$, $k_c = 2$ and $k_e = 4$, we obtain $\mathrm{BIC}_c = 106.17$ and $\mathrm{BIC}_e = 105.57$, which provides marginal support for an eccentric orbit at $e = 0.111 \pm 0.046$, with the 95% limit at $e < 0.20$. We repeated the caculations, setting $\sigma_r = 0$ m s^{-1} since this results in a reduced χ^2 of less than unity for the eccentric orbit. This time, we obtained a value of $\chi^2_c = 16.65$ and $\chi^2_e = 9.63$. Using $N = 16$, $k_c = 2$ and $k_e = 4$, we obtain $\mathrm{BIC}_c = 105.66$ and $\mathrm{BIC}_e = 104.18$, which supports an eccentric orbit at $e = 0.111 \pm 0.039$.

GJ-436

GJ-436b is a 0.071 M_j planet on a 2.64 day eccentric orbit around a M2.5 star (V=10.7), first reported by Butler et al. (2004). Deming et al. (2007) detected the secondary eclipse using Spitzer, placing a constraint on the secondary eclipse phase $\phi_{\mathrm{occ}} = 0.587 \pm 0.005$. This translates into $e \cos \omega = 0.1367 \pm 0.0012$, which we apply as a Bayesian prior in the calculation of our merit function.

We used the 59 HIRES measurements from Maness et al. (2007), setting $\tau = 1.5$ d and $\sigma_r = 5.5$ m s^{-1} to obtain a value of reduced χ^2 of unity for the circular orbit. We imposed the prior information from photometry $P = 2.64385(9)$ from Maness et al. (2007)and $T_{tr} = 2454280.78149(16)$ from Deming et al. (2007) and obtained a value of $\chi^2_c = 59.74$ and $\chi^2_e = 38.86$. Using $N = 61$ (59 measurements and 2 priors from photometry) and $k_c = 2$ for the circular orbit, we obtain $\mathrm{BIC}_c = 371.38$. Using $N = 62$ (59 measurements and 3 priors from photometry) and $k_e = 3$ (V_0, K, $e \sin \omega$) for the eccentric orbit, we obtain $\mathrm{BIC}_e = 354.67$, which supports an eccentric orbit at $e = 0.157 \pm 0.024$, with the 95% limit at $e < 0.21$. We repeated the caculations, setting $\sigma_r = 3.95$ m s^{-1} to obtain a reduced χ^2 of unity for the eccentric orbit. This time, we obtained a value of $\chi^2_c = 88.20$

and $\chi^2_e = 59.39$. This time, we obtain $\mathrm{BIC}_c = 372.67$ and $\mathrm{BIC}_e = 348.03$, which supports an eccentric orbit at $e = 0.153 \pm 0.017$, which is in agreement with Deming et al. (2007), who reported $e = 0.150 \pm 0.012$.

HAT-P-16

HAT-P-16b is a 4.19 M_j planet on a 2.78 day orbit around a F8 star (V=10.7), first reported by Buchhave et al. (2010). The original authors found an eccentricity of $e = 0.036 \pm 0.004$. We re-analysed the 7 high resolution FIES measurements, 14 medium resolution FIES measurements and 6 HIRES measurements, with two priors from photometry on the period and mid-transit time. We set $\tau = 1.5$ d for all instruments and set $\sigma_r = 115$, 185, and 28 m s^{-1} respectively for the three instruments to obtain a reduced χ^2 of unity for each individually. We then analysed them together using both a circular ($\chi^2 = 28.83$) and an eccentric orbit ($\chi^2 = 3.81$). Using $N = 29$, $k_c = 4$ and $k_e = 6$, we obtain $\mathrm{BIC}_c = 314.74$ and $\mathrm{BIC}_e = 296.45$, which supports an eccentric orbit at $e = 0.034 \pm 0.010$. Figure 5.11 (left) shows the data from Buchhave et al. (2010), with a circular orbit overplotted with a solid line and an eccentric orbit with the dotted line. The residuals are plotted for the circular solution and they show a clear periodic signal.

We repeated the analysis, this time setting $\sigma_r = 0$ (reduced $\chi^2 = 0.62$, indicating over-fitting), 16 (reduced $\chi^2 = 33$), and 4.7 m s^{-1} respectively and separately for the three datasets (i.e. aiming for a reduced χ^2 of unity for each dataset individually, with an eccentric orbit). We then analysed them together using both a circular ($\chi^2 = 347.86$) and an eccentric orbit ($\chi^2 = 44.62$). Using $N = 29$, $k_c = 4$ and $k_e = 6$, we obtain $\mathrm{BIC}_c = 541.64$ and $\mathrm{BIC}_e = 245.14$, which supports an eccentric orbit at $e = 0.034 \pm 0.003$. We thus confirm the eccentricity of HAT-P-16b, which means this is the planet with the smallest eccentricity that is reliably measured. This is in part helped by the fact that HAT-P-16b is a very massive planet, making the radial velocity signal for an eccentric orbit very clear. Figure 5.11 (right) shows the data from Buchhave et al. (2010) again, with an eccentric orbit overplotted with the dotted line.

WASP-14

WASP-14b is a 7.3 M_j planet on a 2.24 day orbit around a F5 star (V=9.8), first reported by Joshi et al. (2009), who found an eccentricity of $e = 0.091 \pm 0.003$. Husnoo et al. (2011) confirmed the eccentricity of the orbit and updated the precise value to $e = 0.088 \pm 0.003$. This makes WASP-14b the planet that is closest to its host star but still has an eccentric orbit, taking the place of WASP-12b.

CoRoT-10, HAT-P-2, HAT-P-15, HD17156, HD80606 and XO-3

The orbits of the planets CoRoT-10b ($e = 0.110 \pm 0.039$), HAT-P-2b ($e = 0.517 \pm 0.003$), HAT-P-15b ($e = 0.190 \pm 0.019$), HD17156b ($e = 0.677 \pm 0.003$), HD80606b ($e = 0.934 \pm 0.001$) and XO-3b ($e = 0.287 \pm 0.005$) are clearly eccentric from existing literature — see Bonomo et al., 2010; Hébrard et al., 2008, 2010; Kovács et al., 2010; Loeillet et al., 2008; Nutzman et al., 2011, respectively.

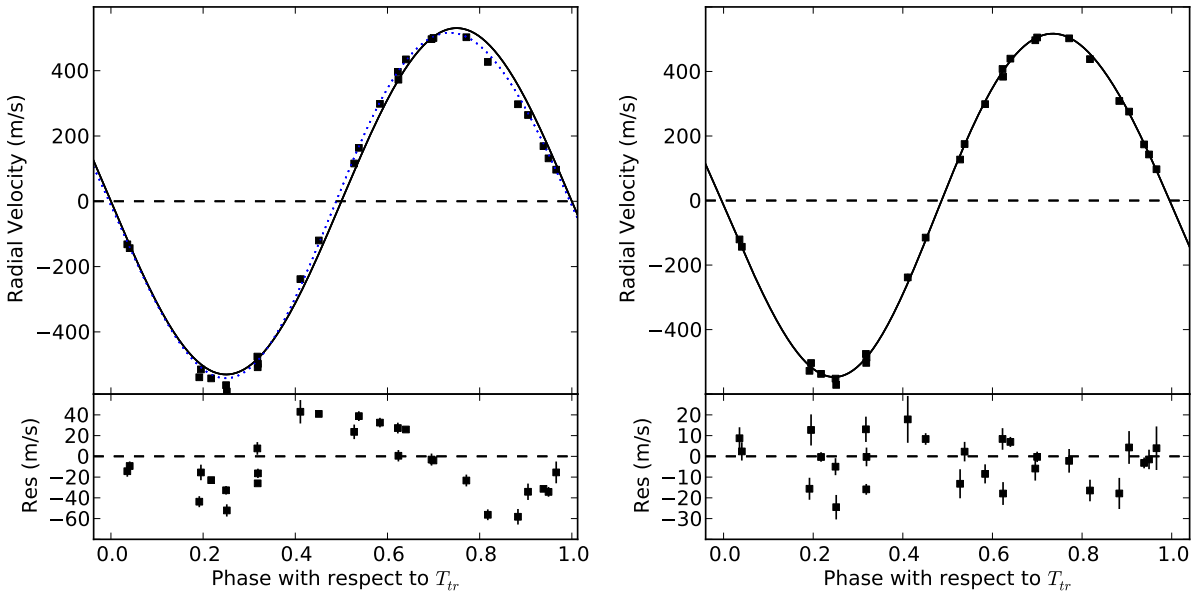

Figure 5.11: Plot showing radial velocity data from Buchhave et al. (2010) for HAT-P-16, plotted against orbital phase with respect to T_{tr}. **Left:** A circular orbit is overplotted with a solid line and an eccentric orbit ($e = 0.034$) is plotted with a dotted line. The bottom panel shows the residuals for a circular orbit: these show a clear periodic signal, indicating the possibility of an eccentric orbit. **Right:** An eccentric orbit ($e = 0.034$) is plotted with a solid line. The residuals are shown for the eccentric orbit.

5.6 Poorly constrained eccentricities

For 26 of the transiting planets that we attempted to place upper limits on their eccentricities, we obtained limits that were larger than 0.1. We considered these eccentricities to be poorly determined. We discuss the cases of HAT-P-4b, WASP-7, XO-2b and Kepler-4b below.

HAT-P-4 (new SOPHIE data)
HAT-P-4b is a 0.68 M_j planet on a 3.06 day orbit around an F star (V=11.2), first reported by Kovacs et al. (2007). We use 13 new SOPHIE radial velocity measurements and the 9 HIRES measurements in Kovacs et al. (2007) to work out the orbital parameters of HAT-P-4b. We impose the period $P = 3.056536(57)$ d and mid-transit time $T_{tr} = 2454248.8716(6)$ BJD as given from photometry in Kovacs et al. (2007). We set $\tau = 1.5$ d and $\sigma_r = 3.35$ m s^{-1} for SOPHIE and $\sigma_r = 3.75$m s^{-1} for HIRES, to obtain a reduced χ^2 of unity for each dataset separately for the best-fit circular orbit. We used 22 measurements in all, and count the two constraints from photometry as two additional datapoints (N=24), and used $k = 3$ for the circular orbit (two V_0, one for each dataset, and the semi-amplitude K). We repeated this analysis with an eccentric orbit $k = 5$ (three degrees of freedom for the circular orbit, and two additional degrees of freedom for the eccentricity, $e\cos\omega$ and $e\sin\omega$). The orbital parameters are given in Table 5.7, and the radial velocity dataset is plotted in Figure 5.12, with residuals shown for a circular orbit. The Figure also shows models of a circular and an eccentric orbit (with $e = 0.064$). For the circular orbit, we obtained $\chi^2 = 22.05$, giving a value of $\mathrm{BIC}_c = 161.96$ and for the eccentric orbit, we obtained $\chi^2 = 16.77$ giving

Parameter	HIRES, Kovacs et al. (2007)	HIRES+SOPHIE *this work*
Centre-of-mass velocity V_0 [m s^{-1}]	12.1±0.9	20.3 ± 2.6 (HIRES) −1402.0 ±4.0 (SOPHIE)
Orbital eccentricity e	0 (adopted)	0.064±0.028, $e < 0.11$
Argument of periastron ω [^{o}]	0 (unconstrained)	0 (unconstrained)
$e \cos \omega$	–	−0.018±0.012
$e \sin \omega$	–	−0.061±0.027
Velocity semi-amplitude K [m s^{-1}]	81.1±1.9	81.3±2.6

Table 5.7: System parameters for HAT-P-4. Left: Kovacs et al. (2007). Right: Results from our new SOPHIE radial velocity data and the original HIRES data. Median values for V_0 and K are quoted for the circular orbits, as well as 68.3% confidence limits obtained from the eccentric solution. The 95% upper limit on eccentricity is also given.

a value of BIC$_e$ = 163.04. We repeated these calculations by setting $\tau = 1.5d$, σ_r = 1.81 m s^{-1} for HIRES, and kept σ_r = 3.35 m s^{-1} for SOPHIE, since we were unable to determine a value of σ_r that would allow the MCMC chain to converge and lead to a χ^2 of unity for an eccentric orbit. This time, we obtained χ^2 = 25.88 for the circular orbit, giving a value of BIC$_c$ = 161.96 and for the eccentric orbit, we obtained χ^2 = 20.05 giving a value of BIC$_e$ = 162.49. We find that the circular orbit cannot be excluded for HAT-P-4b, but because the eccentricity is $e = 0.064 \pm 0.028$ with an upper limit of $e < 0.11$, which is above 0.1, we classify HAT-P-4b as having a poorly constrained eccentricity.

WASP-7 (new HARPS data)

WASP-7b is a 1.0 M$_j$ planet on a 4.95 day orbit around a F5 star (V=9.5), first reported by Hellier et al. (2009). We analysed our 11 new HARPS measurements for WASP-7 as well as 11 measurements from Hellier et al. (2009) using CORALIE, and used the photometric constraints on the orbital period $P = 4.954658(55)$ and mid-transit time $T_{tr} = 2453985.0149(12)$ from the same paper. For both instruments, we set τ = 1.5 d and for CORALIE, we set σ_r = 28.3 m s^{-1} while for HARPS, we set σ_r = 210 m s^{-1} in order to get a value of reduced χ^2 equal to unity for the circular orbit. We performed the MCMC analysis twice: the first time fitting for the systemic velocity v_0 and semi-amplitude K, and the second time adding two parameters $e \cos \omega$ and $e \sin \omega$ to allow for an eccentric orbit. The best-fit parameters are given in Table 5.8). We plot the radial velocity data against time (Figure 5.13, left) and phase (Figure 5.13, right). When the residuals for a circular orbit are plotted, and a scatter of about 30 m s^{-1} is clearly seen, which is much larger than the median uncertainties of σ = 2.21 m s^{-1} on the radial velocity measurements. This is similar to that found by Hellier et al. (2009) from their CORALIE data. An eccentric orbit does not reduce the scatter. The value of χ^2 for the circular orbit is 22.37 and that for an eccentric orbit is 18.11. This leads to a value of BIC$_c$ = 250.62 and BIC$_e$ = 252.72, respectively, for 22 measurements, 2 constraints from photometry and 3 and 5 free parameters respectively (Keplerian orbits, but with two V_0 to account for a possible offset between the two instruments). This shows that the circular orbit is still preferred, and an eccentric orbit does not explain the scatter. We repeated this using σ_r = 33.8 m s^{-1} for CORALIE while for HARPS, we set σ_r = 158.5 m s^{-1} in order to get a value of reduced χ^2 equal to unity for the eccentric or-

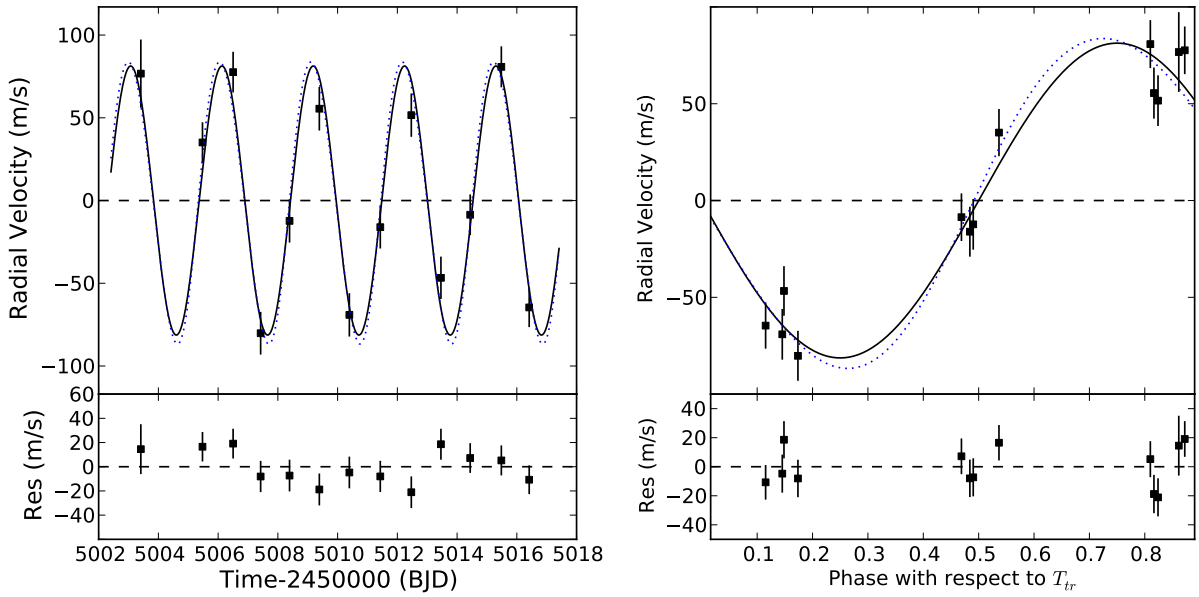

Figure 5.12: Plot showing our new HARPS radial velocity data for HAT-P-4, plotted against time (**left**) and orbital phase with respect to T_{tr} (**right**). A circular orbit (solid line) and an orbit with the best-fit eccentricity (dotted line, $e = 0.064$) are overplotted. The residuals relative to the circular orbit are shown in the bottom panel.

bit. We performed the MCMC analysis both for a circular and eccentric orbit. The value of χ^2 for the circular orbit is 146.95 and that for an eccentric orbit is 146.86. This leads to a value of $\mathrm{BIC}_c = 367.47$ and $\mathrm{BIC}_e = 373.91$, respectively, for 22 measurements, 2 constraints from photometry and 3 and 5 free parameters respectively (Keplerian orbits, but with two V_0 to account for a possible offset between the two instruments). This shows that the circular orbit is still preferred, and an eccentric orbit does not explain the scatter. WASP-7 is an F5V star, with a temperature of $T_{\mathrm{eff}} = 6400 \pm 100$ K. Despite the result of the original paper that WASP-7 is not chromospherically active above the 0.02 mag level, Lagrange et al. (2009) found evidence for other F5V stars showing radial velocity variability with a scatter at this level, for example HD 111998, HD 197692 or HD 205289, with scatters of 40 m s^{-1} 30 m s^{-1} and 29 m s^{-1} respectively. Our derived value of eccentricity is $e = 0.103 \pm 0.061$, with the 95% upper limit is at $e < 0.25$. We therefore classify the eccentricity of the orbit of WASP-7b as poorly constrained

In Figure 5.13, we have also plotted the bisector span, the signal to noise at order 49, the contrast and full width at half maximum for the cross-correlation function against the same time axis. The large scatter in radial velocity residuals can be seen to be correlated with both the bisector span and the full width at half maximum of the cross correlation function.

XO-2 (new SOPHIE data)

XO-2 is a 0.6 M_j planet on a 2.62 day orbit around a K0 star (V=11.2), first reported by Burke et al. (2007). We use 9 new SOPHIE radial velocity measurements and the 10 HJS measurements in Burke et al. (2007) to work out the orbital parameters of XO-2. We impose the period $P = 2.6158640(21)$ d and mid-transit time $T_{tr} = 2454466.88467(17)$ BJD as given from photometry in Fernandez et al.

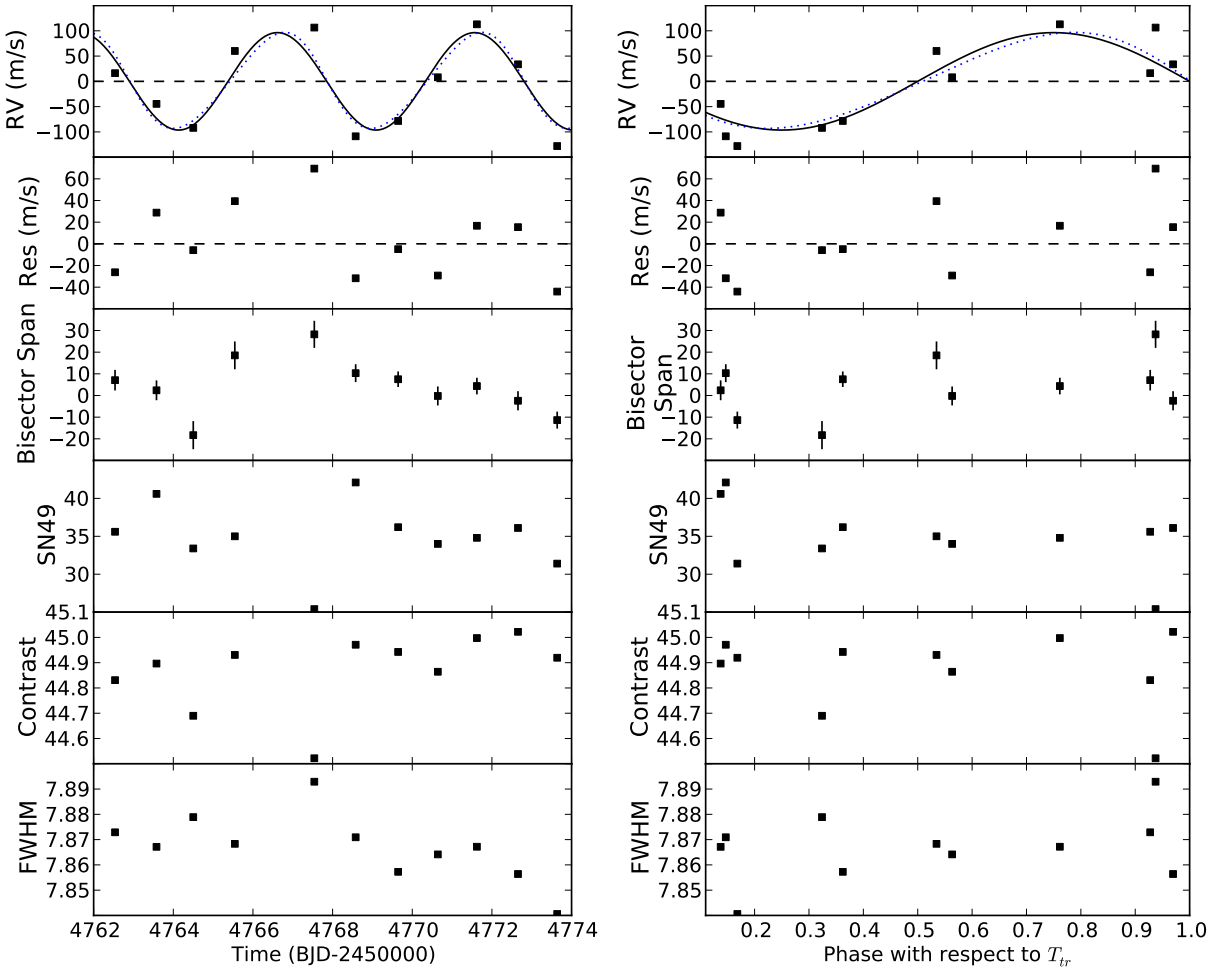

Figure 5.13: HARPS measurements of WASP-7 plotted against time (**left**) and phase with respect to the mid-transit time T_{tr} (**right**). In each case, a solid line is overplotted to represent a circular orbit and the residuals are plotted for this circular orbit. It is clear that a signal is present in the residuals (see text). An eccentric orbit with the best-fit value of $e = 0.103$ is overplotted in both panels with a dotted line, but it is almost indistinguishable from the circular solution at this scale.

Parameter	Hellier et al. (2009)	HARPS, *this work*
Centre-of-mass velocity V_0 [m s^{-1}]	-29850.6 ± 1.7	-29455 ± 103
Orbital eccentricity e	0 (adopted)	0.103 ± 0.061 (<0.25)
Argument of periastron ω [^{o}]	0 (unconstrained)	0 (unconstrained)
$e \cos \omega$	–	0.021 ± 0.068
$e \sin \omega$	–	0.101 ± 0.074
Velocity semi-amplitude K [m s^{-1}]	97 ± 13	96 ± 14

Table 5.8: System parameters for WASP-7. Left: Hellier et al. (2009). Right: Results from our HARPS radial velocity data. Median values for V_0 and K are quoted for the circular orbits, as well as 68.3% confidence limits obtained from the eccentric solution (see section Analysis).

Parameter	HJS, Burke et al. (2007)	HJS, SOPHIE, *this work*
Centre-of-mass velocity V_0 [m s^{-1}]	–	-1.3 ± 6.3 (HJS), 46860.1±4.1 (SOPHIE)
Orbital eccentricity e	0 (adopted)	0.064±0.041 ($e < 0.14$)
Argument of periastron ω [^{o}]	0 (unconstrained)	0 (unconstrained)
$e \cos \omega$	–	0.007±0.017
$e \sin \omega$	–	−0.063±0.047
Velocity semi-amplitude K [m s^{-1}]	85±8	98.0±4.0

Table 5.9: System parameters for XO-2. Left: Burke et al. (2007). Right: Results from our SOPHIE radial velocity data. Median values for V_0 and K are quoted for the circular orbits, as well as 68.3% confidence limits obtained from the eccentric solution. The 95% upper limit on eccentricity is also given.

(2009). We set $\tau = 1.5$ d and $\sigma_r = 5.3$ m s^{-1} for SOPHIE and $\sigma_r = 0$ m s^{-1} for HJS (because the HJS data alone, with a circular orbit, yield a reduced χ^2 of 0.78, indicating overfitting) to obtain a reduced χ^2 of unity for the best-fit circular orbit. We used 19 measurements in all, and count the two constraints from photometry as two additional datapoints ($N = 21$), and used $k = 3$ for the circular orbit (two V_0, one for each dataset, and the semi-amplitude K). We repeated this analysis with an eccentric orbit $k = 5$ (two degrees of freedom for the circular orbit, and two additional degrees of freedom for the eccentricity, $e \cos \omega$ and $e \sin \omega$). The orbital parameters are given in Table 5.9, and the radial velocity dataset is plotted in Figure 5.14, with residuals shown for a circular orbit. The Figure also shows models of a circular and an eccentric orbit (with $e = 0.064$). For the circular orbit, we obtained $\chi^2 = 19.65$, giving a value of $\mathrm{BIC}_c = 165.55$ and for the eccentric orbit, we obtained $\chi^2 = 17.57$ giving a value of $\mathrm{BIC}_e = 169.55$. We repeated the calculations using $\sigma_r = 7.05$ m s^{-1} for SOPHIE and $\sigma_r = 0$ m s^{-1} for HJS (because the HJS data alone, with an eccentric orbit, yield a reduced χ^2 of 0.56, indicating overfitting) to obtain a reduced χ^2 of unity for the best-fit eccentric orbit. For the circular orbit, we obtained $\chi^2 = 18.02$, giving a value of $\mathrm{BIC}_c = 165.21$ and for the eccentric orbit, we obtained $\chi^2 = 16.01$ giving a value of $\mathrm{BIC}_e = 169.29$. In both cases, i.e. using the optimal value of σ_r for a circular orbit and using the optimal value of σ_r for an eccentric orbit, a circular orbit is favoured. The 95% upper limit is $e < 0.14$, which is above 0.1, so we classify the orbital eccentricity of XO-2 as poorly constrained.

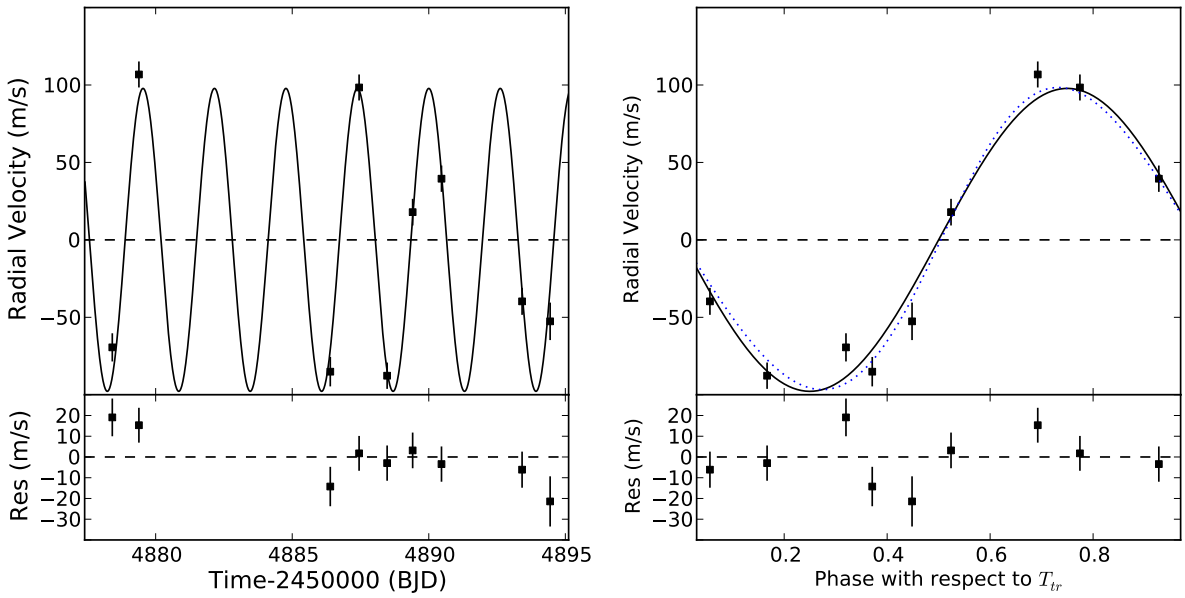

Figure 5.14: Plot showing our new SOPHIE radial velocity data for XO-2, plotted against orbital phase with respect to T_{tr}. A circular orbit (solid line) and an orbit with the best-fit eccentricity (dotted line, but almost undistinguishable from the circular solution since $e = nnnn$) are overplotted. The residuals relative to the circular orbit are shown in the bottom panel.

Kepler-4
Kepler-4b has a derived eccentricity of $e = 0.25^{+0.11}_{-0.12}$, with a 95% upper limit of $e < 0.43$ Kipping and Bakos (2011), so we classify it as "poorly constrained eccentricity".

Other planets

For the 8 objects CoRoT-6, HAT-P-1, HAT-P-3, HAT-P-6, HD149026, Kepler-6, WASP-10 and WASP-21, we found the BIC_e for an eccentric orbit was smaller than the BIC_c for a circular orbit if we assume a σ_r that yields a reduced χ^2 of unity for an eccentric orbit, whereas the BIC_c for a circular orbit was smaller than the BIC_e for an eccentric orbit if we assume a σ_r that yields a reduced χ^2 of unity for a circular orbit. This suggests that the current RV datasets do not constrain the orbit enough for us to detect a finite eccentricity. We have already discussed the case of WASP-10b in Section 5.3 above.

HD189733b and HD209458b are both on orbits that are compatible with a circular model: Laughlin et al. (2005) reported the 95% limits on eccentricity for HD 209458b ($e < 0.042$) and we estimate the upper limit for HD189733b from Triaud et al. (2009) assuming a Gaussian probability distribution, $e < 0.008$). In both cases, the eccentricity is strongly constrained by the timing of the secondary eclipse. No radial velocity data was found for Kepler-5 in the literature or online, but we include the results of Kipping and Bakos (2011) in this study: Kepler-5b has an eccentricity of $e = 0.034^{+0.029}_{-0.018}$, with a 95% upper limit of $e < 0.086$. We therefore classify Kepler-5b as having a circular orbit. We also omitted an analysis of the two-planet system HAT-P-13, choosing to estimate the 95% limits on the orbital eccentricity of HAT-P-13b from the literature ($e < 0.022$) and classify this orbit as circular.

5.7 Additional planetary systems

We now extend our sample with critical review of new literature measurements since this study was performed. In addition to the 64 planets considered so far, we included 17 objects in the original papers (Husnoo et al., 2012; Pont et al., 2011). Three objects had eccentric orbits, 11 had orbits where $e > 0.1$ is excluded at the 95% level and two were brown dwarves. The additional planets on eccentric orbits were HAT-P-17b (Howard et al., 2012, $e = 0.346 \pm 0.007$), HAT-P-21b Bakos et al., 2011a, $e = 0.228 \pm 0.016$ and HAT-P-31b (Kipping et al., 2011, $e = 0.245 \pm 0.005$).

The additional planets on orbits that are consistent with circular were:
CoRoT-18b ($e < 0.08$ at 3-σ, Hébrard et al., 2011),
HAT-P-20b ($e < 0.023$, estimated from Bakos et al., 2011a),
HAT-P-22b ($e < 0.031$, estimated from Bakos et al., 2011a),
HAT-P-25b ($e < 0.068$, estimated from Quinn et al., 2012),
HAT-P-30b ($e < 0.074$, estimated from Johnson et al., 2011),
WASP-23b ($e < 0.062$ at 3-σ, Triaud et al., 2011),
WASP-34b ($e < 0.058$, estimated from Smalley et al., 2011),
WASP-43b ($e < 0.04$ at 3-σ, Hellier et al., 2011),
WASP-45b ($e < 0.095$, Anderson et al., 2012),

WASP-46b ($e < 0.065$, Anderson et al., 2012) and
τ Boötis b ($e < 0.045$, estimated from Butler et al., 2006).

The two brown dwarves were OGLE-TR-122b (Pont et al., 2005a, $e = 0.205 \pm 0.008$) and OGLE-TR-123b (Pont et al., 2005b, $e = 0$). In addition to the above, we also considered the case of WASP-38 (Barros et al., 2011), which has an eccentricity of $e = 0.031 \pm 0.005$, indicating it is in the process of circularisation, just like WASP-14 and HAT-P-16.

New objects since the publication of our papers

In this thesis, we now include objects that have been announced in the meantime: the four planets CoRoT-20b ($e = 0.562 \pm 0.013$, Deleuil et al., 2012), CoRoT-23b ($e = 0.16 \pm 0.02$, Rouan et al., 2012), HAT-P-34b ($e = 0.441 \pm 0.032$, Bakos et al., 2012) and Kepler-39 ($e = 0.12 \pm 0.02$, Bouchy et al., 2011) are all on eccentric orbits.

On the other hand, the planets CoRoT-14b (Tingley et al., 2011), HAT-P-22b (Bakos et al., 2011b), Kepler-14b (Buchhave et al., 2011), WASP-29b (Hellier et al., 2010), WASP-32b (Maxted et al., 2010), WASP-50b (Gillon et al., 2011), WASP-52b (Hébrard et al., 2013), WASP-60b (Hébrard et al., 2013) and WASP-80 (Triaud et al., 2013) are all on orbits consistent with circular.

Conclusion

In this chapter, we have looked at the evidence for eccentric orbits for a large sample of exoplanets. We have added new measurements to improve the estimate for several objects, and we reanalysed existing data for several other objects. In the next chapter, we discuss the relevance of tidal evolution in these systems we have covered here.

Chapter 6

Orbital evolution of hot Jupiters

In the previous chapters, we looked at the orbital eccentricity of individual objects. In this chapter, we look at the global picture. The empirical distributions of orbital eccentricities, projected spin-orbit angles, semi-major axes and stellar spins show a clear preference for a migration mechanism that involves dynamical and tidal evolution of the orbits.

6.1 The Mass-Period plane

The mass-period plane is a useful diagnostic tool for studying the effects of tidal interactions for various regimes. Figure 6.1 shows a plot of the mass ratio M_p/M_* against orbital period for transiting planets with orbital period $P < 20$ days. The empty symbols represent orbits that are consistent with circular, and the black symbols represent eccentric orbits, whereas grey symbols represent objects with small ($e < 0.1$), but significant eccentricities. The circles represent the G dwarfs and the squares represent F dwarfs.

As described in Chapter 2, the strength of tidal interactions between a planet and the host star decreases with increasing semi-major axis (i.e. towards the right in Figure 6.1). Furthermore, the tide raised on the star is larger for a heavier planet, whereas the tide raised on the planet by the star is stronger for a lighter planet. Hence, the planets on the lower left and upper left of the Figure tend to be on circular orbits, whereas those in the middle of the plot tend to be on eccentric orbits. The larger number of low mass objects on circular orbits than heavier objects can be explained as follows.

Lighter planets are mostly circularised by tides raised in the planet by the star, and hence the low mass planets are easier to circularise. An intriguing feature was first pointed out by Mazeh, Zucker, and Pont (2005), who plotted the mass of the first six exoplanets against the period, and drew a straight line (with a negative gradient) through the measurements. In Figure 6.1, it can be seen that the new measurements mean that the mass-period relation of Mazeh, Zucker, and Pont (2005) is no longer a straight line, but a conglomeration in a particular region of the mass-period plane, i.e. the lower left. We therefore conclude that the low mass hot Jupiters on orbits that are consistent with circular around G dwarfs are able to migrate inwards until they stop at a minimum period for a given mass.

The heavier planets tend to raise tides on the star, but they are also harder to circularise because of their larger inertia. In this case, the heavier planets can move in further before they are stopped. Planets heavier than about 1.2 M_j

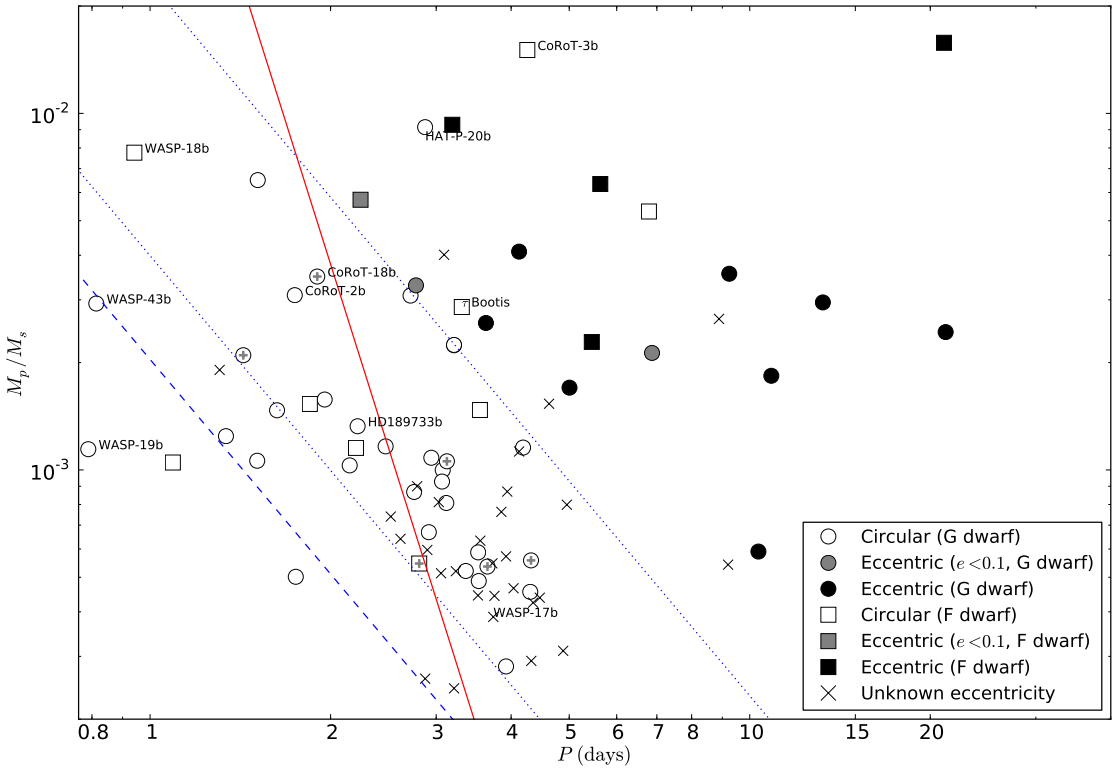

Figure 6.1: Mass ratio versus period plane, for transiting planets with orbital period $P < 20$ days.The labelled symbols (except for WASP-18b) represent objects on orbits that are consistent with circular where the host star rotation is significantly faster than expected, as discussed in Section 6.3. Five objects have been marked with a + symbol to mark objects with upper limits greater than $e < 0.05$ that are described in Section 5.7. The dashed line represents $\alpha = 2$ for $R_p = 1.2R_j$, while the dotted lines represent a value in the range $\alpha = 2.5$–4.5 in the equation $a = \alpha a_R$, where a is the semi-major axis, and a_R is the semi-major axis at the Roche limit (see text). The solid line represents a circularisation isochrone at 1 Gyr for tides in the planet alone.

can migrate inwards and raise tides on the star, leading to a spin-up of the host star, and even synchronisation in some cases where enough angular momentum can be transferred from the orbital motion into the stellar rotation. Only the heaviest planets manage to raise strong enough tides on the star to circularise their orbits without catastrophic decay of their orbits (Pont, 2009). In cases where the planetary angular momentum is insufficient, the process can lead to a run-away migration until the planet is destroyed inside the star.

The Roche limit for a planet is defined by $R_p = 0.462 a_R (M_p/M_*)^{-3}$. If we write the stopping distance as $a = \alpha a_R$, Ford and Rasio, 2006 argued that slow migration on quasi-circular orbits would result in a value of $\alpha = 1$, with the only surviving planets being those that stop at their Roche limit. On the other hand, if the planets were brought in on an eccentric orbit (e.g. dynamical interactions within a system or capture from interstellar space), and then circularised by tidal interaction, the value of α should be two. In Figure 6.1, the dashed line shows this case, with $\alpha = 2$. This does not appear to be a very good fit for the hot Jupiters that are on orbits consistent with circular. The dotted lines show the range $\alpha = 2.5$–4.5. As mentioned in Pont et al. (2011), this larger value of α could indicate the planets had larger radii at the time their orbits were circularised. Subsequent thermal evolution of the planets would have shrunk them (e.g. Baraffe et al., 2004), leaving them stranded further out from their current Roche limits.

6.2 Circularisation

The process of tidal circularisation, spin-orbit alignment and synchronisation are expected to occur roughly in this order, and over a similar timescale. For close-in systems, this timescale is expected to be small compared to the lifetime of the system. If we assume that the principal mechanism for tidal interaction is the dissipation of the equilibrium tide, we can use the equations in Section 2.3.2 to estimate a timescale for circularisation to take place.

We consider two limits, firstly the case where only the tides in the planet dominate, and then the case where only tides in the star dominate. When tides in the planet dominate, $K_* \sim 0$ in Equation 2.7, we can obtain a timescale

$$\tau_p = -\left(\frac{1}{e}\frac{\mathrm{d}e}{\mathrm{d}t}\right)^{-1} = \frac{2}{21G}\frac{1}{k_{2,p}\Delta t_p}\frac{M_p}{M_*^2}\frac{a^8}{R_p^5} \tag{6.1}$$

where we have assumed that $\Omega_e = N_e \approx 1$, i.e. the equation is valid to lowest order in e; $\omega_p/n \sim 1$, i.e. synchronisation of the planetary rotation with the orbit and $x_p \sim 1$, i.e. the planet's equator coincides with the orbital plane.

A similar equation can be written for tides in the star, even though ω_*/n is not typically unity. As long as $\omega_*/n < 18/11$, for small e, the effect of tides in the star will lead to a decrease in orbital eccentricity. We can therefore write,

$$\tau_* = -\left(\frac{1}{e}\frac{\mathrm{d}e}{\mathrm{d}t}\right)^{-1} = \frac{2}{21G}\frac{1}{k_{2,*}\Delta t_*}\frac{M_*}{M_p^2}\frac{a^8}{R_*^5} \tag{6.2}$$

Of course, as explained by Jackson, Greenberg, and Barnes (2008a), the radial and eccentricity evolution equations are coupled, and such a timescale may not represent an accurate story of the orbital evolution of any single system. It simply gives us a first estimate that allows us to rank objects according an average

of the strength of the interaction. We take some typical values of $k_{2,p}\Delta t_p \sim 0.01$ s and $k_{2,*}\Delta t_s \sim 1$ s, which would correspond to tidal quality factors (Goldreich and Soter, 1966) of about 10^6 and 10^4 respectively, in the constant-Q model (in contrast to the constant Δt model that we consider here) for an orbital period of about 5 d.

We expect planets that are further out to be only weakly affected by tides, whereas close-in planets will experience strong tides. Some of these close-in planets will be heavy enough and close enough to exert their own influence on the star by raising stellar tides. This can be seen in Figure 6.2, where we have plotted the timescale of circularisation assuming tides inside the star alone against the timescale of circularisation assuming tides in the planet alone.

The open symbols represent orbits that are consistent with circular, and the black symbols represent eccentric orbits, whereas the grey symbols represent objects with small ($e < 0.1$), but significant eccentricities. The dashed lines represent lines of constant circularisation timescale, at 1 Myr, 10 Myr, 100 Myr, 1 Gyr and 10 Gyr. For the G dwarfs (circles), orbits that are consistent with circular and eccentric orbits are cleanly segregated by the 10 Gyr isochrone, with HAT-P-16b ($e = 0.034 \pm 0.003$) caught in the process of circularisation. The only apparent exception to this rule is GJ-436, which is an M-dwarf instead of a G-dwarf. In this work, do not investigate this difference further.

For the F dwarfs (squares) with planets in non-circular orbits (open symbols), WASP-14b ($T_{\rm eff} = 6475 \pm 100$ K) has a small eccentricity $e = 0.008 \pm 0.003$ and XO-3b ($T_{\rm eff} = 6429 \pm 100$ K) has an eccentricity of 0.287 ± 0.005, whereas CoRoT-3b ($T_{\rm eff} = 6740 \pm 140$ K) is on an orbit that is consistent with circular. This suggests that in the dissipation factor in hotter stars may vary in an unknown fashion, although the small eccentricity of WASP-14b and the moderately small eccentricity of XO-3, together with the short timescale for stellar tides indicate that tides in the star are clearly important even in these cases.

Since our papers (Husnoo et al., 2012, 2011; Pont et al., 2011) were published, new objects have been discovered as described in Section 5.7. We indicate these as diamonds in Figure 6.2, where it can be seen that they follow the same pattern described here.

Hot Neptunes

GJ-436b is a planet on an eccentric orbit ($e = 0.153 \pm 0.017$) in a region of the mass-scale plane where tidal effects on the planet are expected to be significant. The planet is a hot Neptune so it is likely that the structure is different enough that the tidal quality factor Q is very much higher (Goldreich and Soter, 1966), leading to a longer circularisation timescale. In this case, GJ-436b would simply not have had enough time to circularise its orbit.Another possibility that was initially suggested by Maness et al. (2007), is that a second companion may be present in the system and is pumping up the eccentricity of GJ-436b by secular interactions. Further measurements with radial velocity (Ribas et al., 2009) and photometry (Ballard et al., 2010) appear to rule this possibility out.

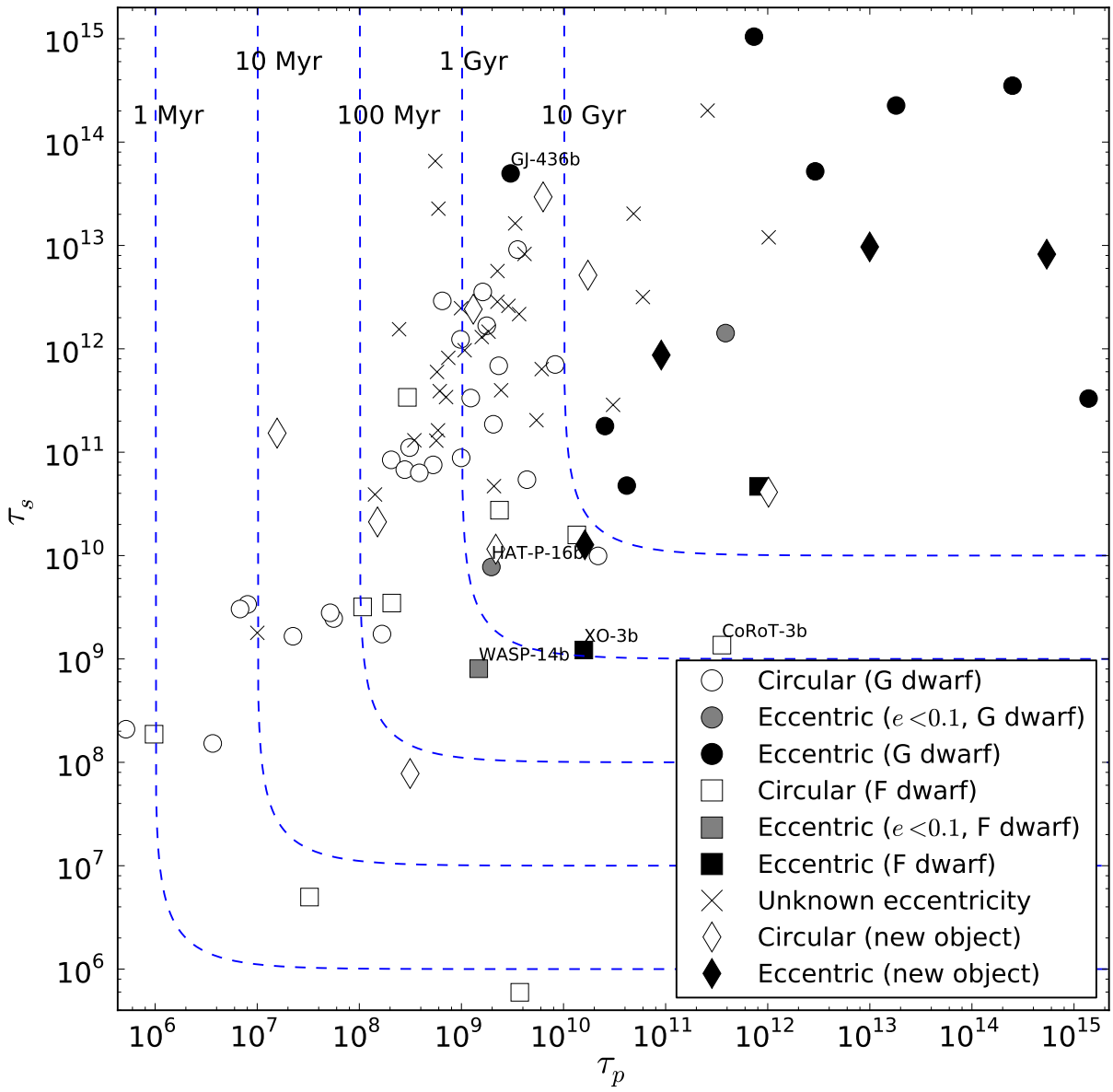

Figure 6.2: Timescale of circularisation assuming tides inside the star alone (vertical axis) against the timescale of circularisation assuming tides in the planet alone (horizontal axis). The dotted lines represent lines of constant circularisation timescale. The diamond symbols represent objects newly announced since our original papers, and they follow the same pattern (see Section 6.2).

Name	$P_{\rm rot}$ (d)	Expected $P_{\rm rot}$ (d)
CoRoT-2	4.52±0.02	36
CoRoT-18	6.3±0.9	49
HAT-P-20	11.3±2.2	57
HD 189733	12.95±0.01	57
WASP-19	10.5±0.2	42
WASP-43	7.6±0.7	57

Table 6.1: Table showing the systems with excess rotation in the left panel of Figure 6.3. $P_{\rm rot}$ is the stellar rotation period today, and 'Expected $P_{\rm rot}$' is the expected rotation period of the star as estimated from the rotation isochrones of Strassmeier & Hall (1988).

6.3 Synchronisation

Tidal dissipation in the host star exerts a torque on the star, causing an exchange of angular momentum between the stellar spin and the orbit. If the host star is a slow rotator, it can be spun up by the tidal interaction. This would occur on a similar timescale as circularisation. Figure 6.3 shows the same axes as Figure 6.2, but on the left panel, the star symbols represent objects with excess stellar rotation. In the case of CoRoT-3b and τ Boötis b, the rotation of the host star has been synchronised with the orbital period.

Pont (2009) also pointed out that HD 189733 and CoRoT-2b were rotating faster than expected from the isochrones of Strassmeier & Hall (1988), even if the stellar rotations were not synchronised. We can now confirm that four more objects are clearly in this regime: CoRoT-18, HAT-P-20, WASP-19 and WASP-43. The rotation periods of these stars and the expected rotation periods are shown in Table 6.1.

From Figure 6.3, we note that the estimated timescale for orbital circularisation due to tidal effects in the star alone is less than 5 Gyr for the objects WASP-19, WASP-43, CoRoT-2, CoRoT-18 and CoRoT-3. This means that tidal dissipation in the star could lead to the excess rotation well within the lifetime of these stars. On the other hand, the two objects τ Boötis b and HAT-P-20 have timescales $\tau_* \sim 10$ Gyr, while HD 189733b has $\tau_* \sim 80$ Gyr. It should be noted that the biggest uncertainty in the tidal model, even after we include the higher order terms in the tidal equations in Chapter 2, is the tidal quality factor, whose estimates can vary by up to two orders of magnitude Leconte et al. (2010). In this case, the timescales we derive should be considered to provide a useful ranking system for the order in which the objects would evolve. In the case of HD 189733, the tidal dissipation strength would need to be stronger by a single order of magnitude for the tidal evolution to match the observations. Indeed, since HD 198733 is not synchronised with the orbit of the planet, the required variation in dissipation factor is even less. In contrast, orbital circularisation in many of these cases may well have occurred due to dissipation in the planet instead.

Planets that are unable to spin-up their parent stars to synchronisation may be doomed to destruction. Hellier et al. (2009) pointed out that the existence of WASP-18 at its current position in the mass-period plane suggests that either the tidal dissipation in the system is several orders of magnitude smaller than expected, or that the system is caught at a very special time while it is in the last

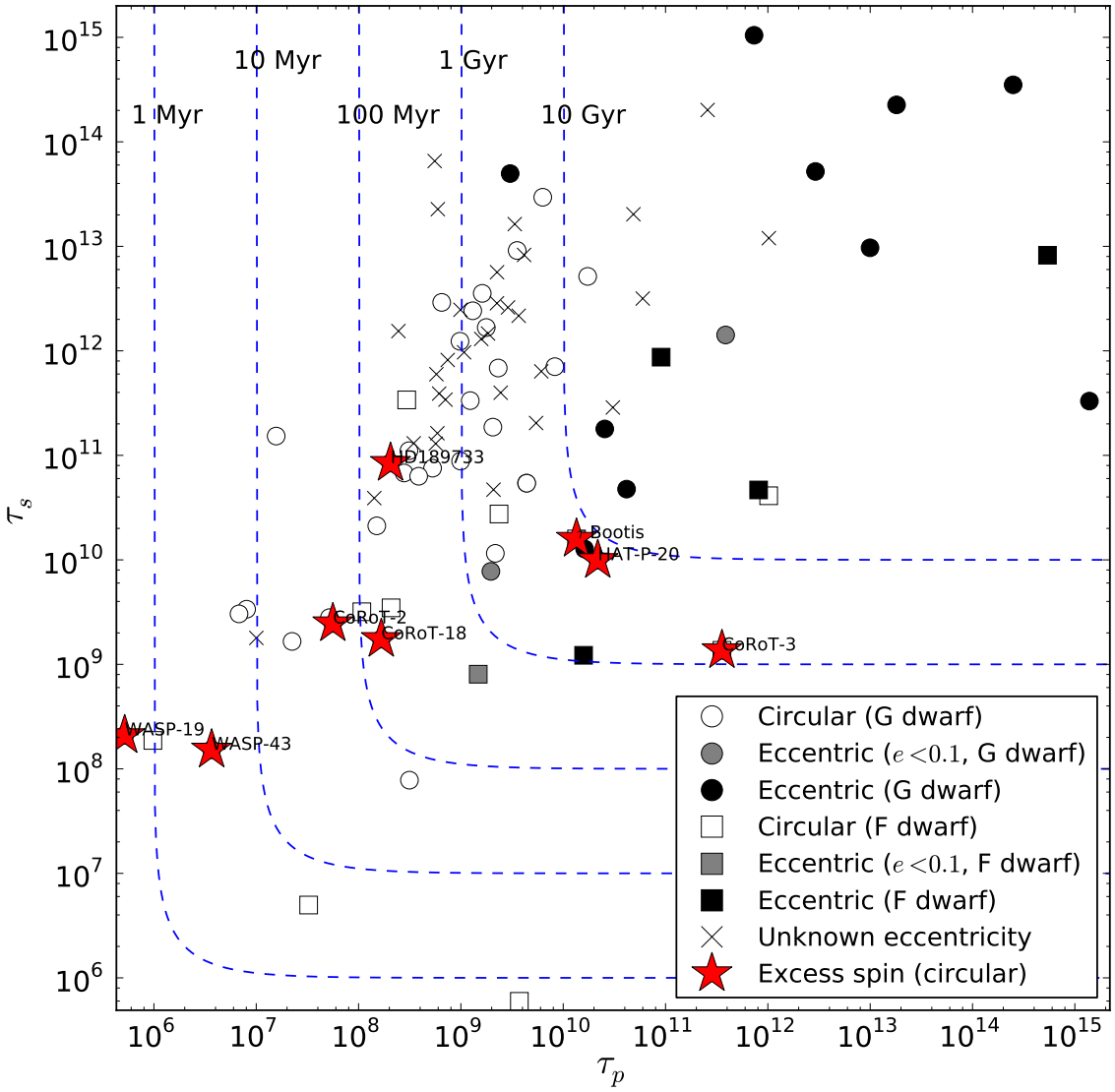

Figure 6.3: The axes are the same as Figure 6.2. The star symbols represent objects where there is evidence of spin-up. These are stars that rotate faster than predicted by the isochrones of Strassmeier & Hall (1988). In the case of the two hot stars CoRoT-3 and τ Boötis b, the stellar rotation have even become synchronised with the orbital period. No objects with a stellar tidal dissipation timescale larger than about $\tau_* > 10^{11}$ years show any evidence of excess rotation, supporting the case for tidal involvement in the objects with excess rotation.

10^{-4} of the estimated lifetime of the system. The latter possibility sounds more plausible, considering the striking paucity of heavy planets at short period.

6.4 Spin-orbit alignment

Figure 6.4 shows the same axes as before (timescales), and the circles represent G stars and the squares represent F stars. The empty symbols now represent aligned systems ($\lambda < 30^\circ$), and the filled symbols represent misaligned systems ($\lambda > 30^\circ$). In this case, the G dwarfs are aligned, except for CoRoT-1($T_{\rm eff} = 5950 \pm 150$ K), WASP-1 ($T_{\rm eff} = 6110 \pm 245$ K) and HAT-P-32 ($T_{\rm eff} = 6207 \pm 88$ K), which are actually hot stars, and WASP-8 is outside the region of strong tides in the star.

CoRoT-1, WASP-1 and the F dwarfs, display a spread in terms of aligned and misaligned, even in cases of strong tides. Winn et al. (2010) found a link between the presence of a convective core and spin-orbit alignment by tidal effects. Thus, exoplanets could migrate inwards by planet-planet scattering, giving rise to orbits with a range of eccentricities and spin-orbit angles. Planets in orbit around cooler stars ($T_{\rm eff} < 6250$ K, where the stellar convective region is significant), can have their orbital angular momentum aligned with the stellar rotation, while planets in orbit around hot stars ($T_{\rm eff} > 6250$ K, where the extent of the convective region is negligible) manage to keep their initial misalignment.

Conclusion

In this chapter, we reviewed the observational constraints on the migration of hot Jupiters. We showed that the eccentricity distribution was consistent with tidal interactions and removed the need for extra sources of eccentricity excitation. Similarly, the projected spin-orbit angle distribution matches the scenario of Winn et al. and the evidence for excess rotation for several objects, including stellar spin-orbit synchronisation, matches expectations from significant tidal interactions.

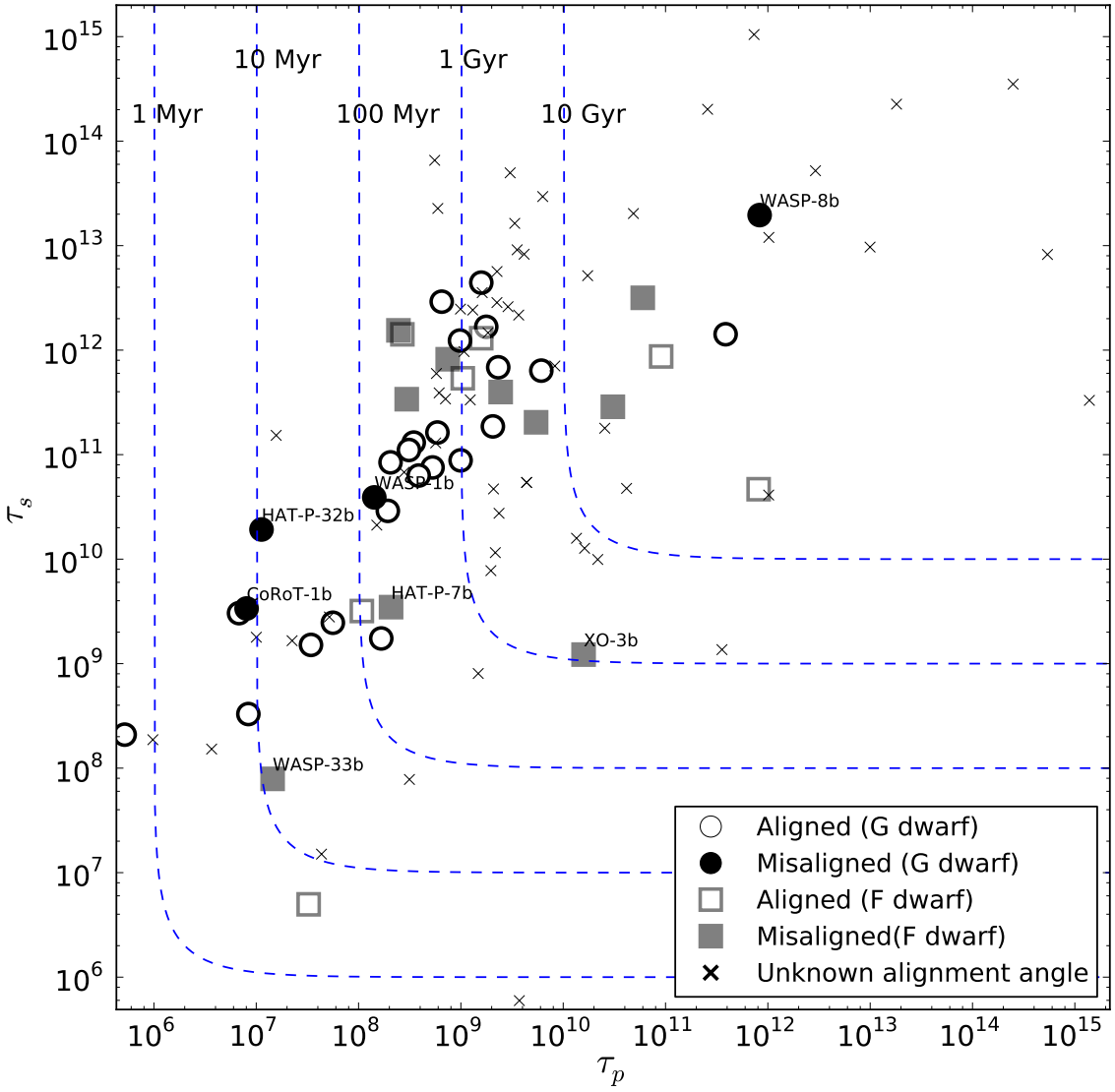

Figure 6.4: The circles indicate aligned systems ($\lambda < 30°$), whereas the star symbols represent misaligned systems ($\lambda > 30°$). In this case, the G dwarfs are aligned (CoRoT-1 and WASP-1 are actually hot stars, and WASP-8 is outside the region of strong tides in the star). The F dwarfs, on the other hand, display a spread in terms of aligned and misaligned, even in cases of strong tides, in agreement with Winn et al. (2010).

Chapter 7

Conclusions and future work

The discovery of exoplanets with mass and composition comparable to Jupiter, and yet located on short period orbits was an unexpected development for the then fledging exoplanet field (Section 1.3). Two major mechanisms were suggested by different groups to explain the necessary migration, namely the disk-migration scenario (Section 1.4) and the dynamical scattering scenario (Sections 1.5, 1.6 and 1.7). One thing that researchers agreed on was that tidal interactions would be strong in these hot Jupiter systems (Section 1.8), and thus the short period orbits were expected to be circular. Although the initial discoveries suggested that this was indeed the case, later discoveries appeared to show several objects on eccentric orbits at very short periods (Section 1.8). This clashed with the theoretical expectations, leading to extensive speculations of additional interactions with undetected companions, and a tidal explanation for the additional energy source for inflated hot Jupiters.

In this thesis, we have used new radial velocity measurements, as well as existing measurements in the literature to recalculate the orbital parameters of a large sample of transiting exoplanets. We have shown that the apparent "exceptions" in the literature, i.e. objects with significant eccentricities at very short periods, have orbits that are consistent with circular after all. Using the timescales for circularisation, synchronisation and alignment, we show that the ensemble of transiting planets is consistent with a history initially involving dynamical interactions followed by tidal interactions that lead to orbital circularisation, spin-orbit alignment and synchronisation in some cases.

7.1 Main achievements

7.1.1 Modified analysis

In Sections 3.5, 3.8, 4.3.1 and 5.2, we describe how we modify the conventional approach to parameter estimation of orbital elements in the field of exoplanets. In particular, we take into account the presence of correlated noise by including an extra term in the uncertainty in Section 4.3.1 and using a correlation matrix with a correlation timescale in Section 5.2. In each case, we modify the "merit function" of the MCMC to include this term. Previous work that ignored the correlation in the noise of radial velocity measurements had led to spurious detection of a finite eccentricity in several systems (Section 5.3).

The second key part of our procedure is the systematic application of a Bayesian model selection step, where we compare the evidence for an eccentric

orbit against that for a circular orbit (Section 3.10). This application of Occam's razor was well known in the study of binary stars, where the Lucy & Sweeney F-test was used for the same purpose. The reason this step is important is because of the positive definite nature of the derived orbital eccentricity — any noise will only push the eccentricity up in the MCMC chain, as the eccentricity cannot be negative. This effect has been demonstrated to be relevant in the field of exoplanets by other researchers by using both simulated data and radial velocity measurements for known planets (Section 1.9).

7.1.2 Analysis of new data and reanalysis of existing data

We carried out a literature search for the existing radial velocity measurements of 54 objects, and added 158 new measurements for 12 of these objects (Sections 4.2 and 5.1). We augmented this list with another 40 systems by critically considering the quality of the measurements (numerous measurements, large signal to noise, widespread phase coverage — Sections 5.1 and 5.7). We also included any photometric constraints available on period, mid-transit time and secondary eclipse phase.

We used the techniques described above to analyse these measurements, and obtained updated estimates for the orbital parameters of 54 of the objects in the sample of transiting objects. Several objects were previously believed to be on eccentric orbits, but we showed that the available data suggested these orbits were consistent with circular (Sections 4.3.3 and 5.3). These objects are CoRoT-5b, WASP-6b, WASP-10b, WASP-12b, WASP-17b, WASP-18b and WASP-5b. In all these cases, it is likely that the uncertainties in the original measurements had been underestimated. In the case of WASP-12b, we showed that new measurements made the uncertainty on the derived eccentricity grow, instead of obtaining a more precise and significant eccentricity.

7.1.3 The story from the ensemble of transiting planets

Given that several objects that were previously tagged as "exceptions" having a significant eccentricity at very short period in the previous literature were actually not exceptions at all, we compared the ensemble of eccentricity measurements with theoretical timescale for eccentricity damping (Section 6.2).

We revisited the work of F. Pont (Section 6.3) where it was originally shown that the stars HD 189733 and CoRoT-2 were rotating faster than expected for stars with their estimated masses and ages. In this work, we confirm that the stars CoRoT-18, HAT-P-20, WASP-19 and WASP-43 are also rotating faster than expected by comparing them to isochrones. This is a key signature of tidal evolution, as angular momentum can be taken out of the orbit and dumped into the stellar spin.

We also revisited the scenario suggested by the team of J. Winn, where planets in orbit around hot stars maintain their initial obliquities whereas planets in orbit around cool stars undergo tidal interactions to damp their obliquities (Section 6.4). We plot the projected spin-orbit measurements on the same timescales as we did for circularisation, and show that objects around cool stars and experiencing strong tidal interactions are all aligned, whereas objects that undergo weak interactions maintain their obliquities. This is consistent with the work by Winn's team.

7.2 Outlook

The overall theme of this thesis has been to demonstrate that the present data on close-in exoplanets support the case for a prominent role for tidal interactions between the planet and the host star in the orbital evolution of hot Jupiters.

It would be interesting to see how this picture merges with heavier companion objects: a number of transiting brown dwarfs have been announced in recent years (e.g. Anderson et al., 2011; Bouchy et al., 2011; Díaz et al., 2013), and over the next few years, it may be possible to plot a full picture with everything from hot Jupiter systems to stellar binary systems, as the dichotomy between "tides in the star" and "tides in the companion" would disappear. Another avenue of research may be the recent light curves from the Kepler mission (Batalha et al., 2013), which can provide the rotation periods of a large sample of objects, and thus offer additional evidence for excess rotation in tidally interacting systems.

Appendix A

Radial velocity measurements

In this Appendix, we include the radial velocity measurements we referred to in Chapters 4 and 5. The spectra were obtained and reduced by the co-authors, while I performed the analysis described in this thesis.

Time [BJD-2450000]	RV [km s^{-1}]	σ_{RV} [km s^{-1}]
4849.41844	19.2172	0.0119
4849.42764	19.2028	0.0112
4849.43654	19.1811	0.0111
4849.44552	19.1807	0.0111
4849.45469	19.1678	0.0108
4849.46419	19.1685	0.0106
4849.47405	19.1444	0.0106
4849.48469	19.1353	0.0108
4849.49611	19.0984	0.0118
4849.50751	19.0857	0.0121
4849.51895	19.0812	0.0123
4849.53036	19.0532	0.0123
4849.54177	19.0163	0.0121
4849.55319	19.0076	0.0129
4849.56461	19.0083	0.0119
4849.57603	18.9966	0.0132
4889.37950	19.1295	0.0040
4890.44193	19.0795	0.0047
4912.37616	19.1793	0.0085
4914.36671	18.9750	0.0044
4926.34294	18.9295	0.0043
4935.32914	19.2684	0.0118
4936.31657	19.1644	0.0068
5269.37102	19.3050	0.0038
5271.33688	19.0719	0.0039
5272.38229	19.0430	0.0039
5273.33965	18.8919	0.0039
5282.31904	19.1749	0.0045
5283.35164	19.1109	0.0049

Table A.1: SOPHIE radial velocity measurements for WASP-12 (errors include random component only). For RVs for t=2454849, we find $V_0 = 19.113 \pm 0.014$ kms^{-1}. This data is published in Husnoo et al. (2011)

Time [BJD-2450000]	RV [km s^{-1}]	σ_{RV} [km s^{-1}]
4885.65165	-5.5847	0.0107
4886.57106	-4.7678	0.0111
4886.68397	-4.4453	0.0106
4888.61655	-5.3910	0.0104
4888.68715	-5.1660	0.0107
4889.65818	-4.4914	0.0107
4890.66568	-5.8442	0.0106
4911.59331	-4.0451	0.0116
4912.55658	-5.5238	0.0114
4913.57244	-4.5271	0.0061
4915.57681	-5.2325	0.0122

Table A.2: SOPHIE radial velocity measurements for WASP-14 (errors include random component only). This data is published in Husnoo et al. (2011)

Time [BJD-2450000]	RV [km s^{-1}]	σ_{RV} [km s^{-1}]
4385.86631	23.4168	0.0190
4386.83809	23.6726	0.0139
4387.80863	23.3155	0.0149
4419.81749	23.5811	0.0123
4420.80300	23.3290	0.0118
4421.81461	23.6586	0.0113
4446.77797	23.3936	0.0145
4447.75517	23.4562	0.0130
4448.77217	23.6982	0.0126
4479.67146	23.3161	0.0123
4480.65370	23.6836	0.0140
4481.63818	23.5129	0.0173
4525.59523	23.6451	0.0116
4529.56406	23.3324	0.0127
4530.58002	23.5743	0.0105
4549.58179	23.5793	0.0280
4553.49391	23.3652	0.0124
4554.57636	23.6696	0.0157
4768.77120	23.7041	0.0092
4769.76601	23.4802	0.0104
4770.80872	23.3613	0.0108
4771.76514	23.6955	0.0102
4772.76824	23.4379	0.0109
4773.76896	23.3980	0.0095

Table A.3: HARPS radial velocity measurements for CoRoT-1 (errors include random component only). This data is published in Husnoo et al. (2012)

Time [BJD-2450000]	RV [km s^{-1}]	σ_{RV} [km s^{-1}]
4768.52895	-56.5039	0.0036
4769.51404	-58.1970	0.0038
4770.51329	-56.1017	0.0046
4772.52655	-55.9171	0.0047
4773.52957	-58.2227	0.0042

Table A.4: HARPS radial velocity measurements for CoRoT-3 (errors include random component only). This data is published in Husnoo et al. (2012)

Time [BJD-2450000]	RV [km s^{-1}]	σ_{RV} [km s^{-1}]
4766.56990	-27.8402	0.0033
4767.52666	-27.6797	0.0023
4768.56373	-27.7842	0.0018
4769.54823	-27.7343	0.0017
4770.54665	-27.7131	0.0026
4771.54501	-27.8099	0.0031
4772.56012	-27.6489	0.0027
4773.56432	-27.8568	0.0019

Table A.5: HARPS radial velocity measurements for WASP-2 (errors include random component only). This data is published in Husnoo et al. (2012)

Time [BJD-2450000]	RV [km s^{-1}]	σ_{RV} [km s^{-1}]
4762.60256	57.6687	0.0028
4763.62220	57.5637	0.0022
4764.58386	57.9085	0.0035
4765.59031	57.9871	0.0038
4768.60378	57.9109	0.0022
4769.58081	57.9784	0.0023
4769.71186	58.0331	0.0017
4770.58784	57.6591	0.0024
4770.72474	57.7930	0.0023
4771.57892	57.6311	0.0021
4771.68481	57.5752	0.0019
4772.59125	57.9518	0.0025
4773.59429	57.9811	0.0018
4773.70377	58.0346	0.0024

Table A.6: HARPS radial velocity measurements for WASP-4 (errors include random component only). This data is published in Husnoo et al. (2012)

Time [BJD-2450000]	RV [km s^{-1}]	σ_{RV} [km s^{-1}]
4768.63152	19.7967	0.0022
4768.73169	19.8696	0.0018
4769.62838	20.1047	0.0023
4770.62473	20.1231	0.0022
4770.76117	20.2255	0.0031
4771.60846	19.7737	0.0017
4771.71520	19.7446	0.0021
4772.63762	20.2588	0.0023
4772.73505	20.2071	0.0022
4773.62311	19.8540	0.0021
4773.73277	19.9582	0.0025

Table A.7: HARPS radial velocity measurements for WASP-5 (errors include random component only). This data is published in Husnoo et al. (2012)

Time [BJD-2450000]	RV [km s^{-1}]	σ_{RV} [km s^{-1}]
4762.53711	-29.4388	0.0024
4763.57798	-29.4994	0.0023
4764.50127	-29.5469	0.0032
4765.54456	-29.3948	0.0032
4767.54077	-29.3485	0.0031
4768.57924	-29.5636	0.0021
4769.64528	-29.5332	0.0018
4770.64161	-29.4468	0.0022
4771.62297	-29.3421	0.0019
4772.65474	-29.4212	0.0022
4773.63924	-29.5829	0.0020

Table A.8: HARPS radial velocity measurements for WASP-7 (errors include random component only). This data is published in Husnoo et al. (2012)

Time [BJD-2450000]	RV [km s^{-1}]	σ_{RV} [km s^{-1}]
5003.41234	-1.3253	0.0206
5005.47636	-1.3669	0.0122
5006.50185	-1.3244	0.0123
5007.42327	-1.4822	0.0129
5008.39084	-1.4143	0.0131
5009.38832	-1.3465	0.0132
5010.39331	-1.4711	0.0131
5011.42884	-1.4181	0.0129
5012.46735	-1.3504	0.0131
5013.45923	-1.4487	0.0128
5014.43881	-1.4106	0.0123
5015.48148	-1.3212	0.0124
5016.41444	-1.4666	0.0119

Table A.9: SOPHIE Radial velocity measurements for HAT-P-4 (uncertainties include random component only). This data is published in Husnoo et al. (2012)

Time [BJD-2450000]	RV [km s^{-1}]	σ_{RV} [km s^{-1}]
5002.48517	-10.2995	0.0100
5003.52118	-10.6910	0.0103
5004.59910	-10.2681	0.0137
5005.49926	-10.6377	0.0101
5006.55335	-10.2564	0.0101
5007.53107	-10.5975	0.0101
5008.47624	-10.4027	0.0106
5010.43095	-10.5681	0.0102
5011.52259	-10.3835	0.0102
5013.60648	-10.3090	0.0093
5014.57426	-10.6862	0.0101
5015.58518	-10.2680	0.0103
5016.54123	-10.6808	0.0084

Table A.10: SOPHIE radial velocity measurements for HAT-P-7 (uncertainties include random component only). This data is published in Husnoo et al. (2012)

Time [BJD-2450000]	RV [km s^{-1}]	σ_{RV} [km s^{-1}]
5005.57207	-0.4489	0.0107
5006.57091	-0.2231	0.0100
5007.57482	-0.2619	0.0105
5008.44948	-0.4742	0.0106
5010.44234	-0.4505	0.0107
5011.51233	-0.2499	0.0110
5013.59448	-0.4207	0.0114
5014.56301	-0.1604	0.0108
5015.57356	-0.5090	0.0107
5016.55442	-0.2197	0.0110

Table A.11: SOPHIE radial velocity measurements for TrES-2 (uncertainties include random component only). This data is published in Husnoo et al. (2012)

Time [BJD-2450000]	RV [km s^{-1}]	σ_{RV} [km s^{-1}]
4878.41245	46.7905	0.0091
4879.38681	46.9667	0.0084
4886.39349	46.7748	0.0095
4887.44867	46.9583	0.0084
4888.47514	46.7722	0.0085
4889.40965	46.8778	0.0086
4890.46546	46.8994	0.0085
4893.41643	46.8202	0.0087
4894.44335	46.8073	0.0121

Table A.12: SOPHIE radial velocity measurements for XO-2 (uncertainties include random component only). This data is published in Husnoo et al. (2012)

Bibliography

[1] F. C. Adams and G. Laughlin. "Migration and dynamical relaxation in crowded systems of giant planets". In: *Icarus* 163 (June 2003), pp. 290–306. DOI: 10.1016/S0019-1035(03)00081-2. eprint: arXiv:astro-ph/0301561.

[2] A. E. P. Alapini-Odunlade. "Transiting exoplanets: characterisation in the presence of stellar activity". PhD thesis. University of Exeter, 2010.

[3] S. Albrecht et al. "Obliquities of Hot Jupiter host stars: Evidence for tidal interactions and primordial misalignments". In: *ArXiv e-prints* (June 2012). arXiv:1206.6105 [astro-ph.SR].

[4] M. E. Alexander. "The Weak Friction Approximation and Tidal Evolution in Close Binary Systems". In: *Ap & SS* 23 (Aug. 1973), pp. 459–510. DOI: 10.1007/BF00645172.

[5] R. Alonso et al. "The secondary eclipse of CoRoT-1b". In: *A & A* 506 (Oct. 2009), pp. 353–358. DOI: 10.1051/0004-6361/200912102. arXiv:0907.1653.

[6] R. Alonso et al. "The secondary eclipse of the transiting exoplanet CoRoT-2b". In: *A & A* 501 (July 2009), pp. L23–L26. DOI: 10.1051/0004-6361/200912505. arXiv:0906.2814.

[7] R. Alonso et al. "TrES-1: The Transiting Planet of a Bright K0 V Star". In: *ApJL* 613 (Oct. 2004), pp. L153–L156. DOI: 10.1086/425256.

[8] D. R. Anderson et al. "Wasp-17b: An Ultra-Low Density Planet in a Probable Retrograde Orbit". In: *ApJ* 709 (Jan. 2010), pp. 159–167. DOI: 10.1088/0004-637X/709/1/159. arXiv:0908.1553.

[9] D. R. Anderson et al. "WASP-30b: A 61ăM Jup Brown Dwarf Transiting a V = 12, F8 Star". In: *The Astrophysical Journal Letters* 726.2 (2011), p. L19. URL: http://stacks.iop.org/2041-8205/726/i=2/a=L19.

[10] D. R. Anderson et al. "WASP-31b: a low-density planet transiting a metal-poor, late-F-type dwarf star". In: *A & A* 531, A60 (July 2011), A60. DOI: 10.1051/0004-6361/201016208. arXiv:1011.5882 [astro-ph.EP].

[11] D. R. Anderson et al. "WASP-44b, WASP-45b and WASP-46b: three short-period, transiting extrasolar planets". In: *MNRAS* 422 (May 2012), pp. 1988–1998. DOI: 10.1111/j.1365-2966.2012.20635.x. arXiv:1105.3179 [astro-ph.EP].

[12] D. R. Anderson et al. "WASP-5b: a dense, very hot Jupiter transiting a 12th-mag Southern-hemisphere star". In: *MNRAS* 387 (June 2008), pp. L4–L7. DOI: 10.1111/j.1745-3933.2008.00465.x. arXiv:0801.1685.

[13] A. Aparicio and C. Gallart. "IAC-STAR: A Code for Synthetic Color-Magnitude Diagram Computation". In: *AJ* 128 (Sept. 2004), pp. 1465–1477. DOI: 10.1086/382836. eprint: arXiv:astro-ph/0407589.

[14] P. J. Armitage. "Massive Planet Migration: Theoretical Predictions and Comparison with Observations". In: *ApJ* 665 (Aug. 2007), pp. 1381–1390. DOI: 10.1086/519921. arXiv:0705.3039.

[15] E. Atukeren. "The relationship between the F-test and the Schwarz criterion: Implications for Granger-causality tests". In: *Economics Bulletin* 30 (2010), pp. 494–499.

[16] G. Á. Bakos et al. "HAT-P-20b-HAT-P-23b: Four Massive Transiting Extrasolar Planets". In: *ApJ* 742, 116 (Dec. 2011), p. 116. DOI: 10.1088/0004-637X/742/2/116. arXiv:1008.3388 [astro-ph.EP].

[17] G. Á. Bakos et al. "HAT-P-20b-HAT-P-23b: Four Massive Transiting Extrasolar Planets". In: *ApJ* 742, 116 (Dec. 2011), p. 116. DOI: 10.1088/0004-637X/742/2/116. arXiv:1008.3388 [astro-ph.EP].

[18] G. Á. Bakos et al. "HAT-P-34b-HAT-P-37b: Four Transiting Planets More Massive than Jupiter Orbiting Moderately Bright Stars". In: *AJ* 144, 19 (July 2012), p. 19. DOI: 10.1088/0004-6256/144/1/19. arXiv:1201.0659 [astro-ph.EP].

[19] G. Á. Bakos et al. "HD 147506b: A Supermassive Planet in an Eccentric Orbit Transiting a Bright Star". In: *ApJ* 670 (Nov. 2007), pp. 826–832. DOI: 10.1086/521866. arXiv:0705.0126.

[20] S. Ballard et al. "A Search for Additional Planets in the NASA EPOXI Observations of the Exoplanet System GJ 436". In: *ApJ* 716 (June 2010), pp. 1047–1059. DOI: 10.1088/0004-637X/716/2/1047. arXiv:0909.2875 [astro-ph.EP].

[21] I. Baraffe et al. "The effect of evaporation on the evolution of close-in giant planets". In: *A & A* 419 (May 2004), pp. L13–L16. DOI: 10.1051/0004-6361:20040129. eprint: arXiv:astro-ph/0404101.

[22] A. Baranne et al. "ELODIE: A spectrograph for accurate radial velocity measurements." In: *A&AS* 119 (Oct. 1996), pp. 373–390.

[23] M. Barbieri et al. "HD 17156b: a transiting planet with a 21.2-day period and an eccentric orbit". In: *A & A* 476 (Dec. 2007), pp. L13–L16. DOI: 10.1051/0004-6361:20078787. arXiv:0710.0898.

[24] A. J. Barker and G. I. Ogilvie. "On internal wave breaking and tidal dissipation near the centre of a solar-type star". In: *MNRAS* 404 (June 2010), pp. 1849–1868. DOI: 10.1111/j.1365-2966.2010.16400.x. arXiv:1001.4009 [astro-ph.EP].

[25] A. J. Barker and G. I. Ogilvie. "On the tidal evolution of Hot Jupiters on inclined orbits". In: *MNRAS* 395 (June 2009), pp. 2268–2287. DOI: 10.1111/j.1365-2966.2009.14694.x. arXiv:0902.4563.

[26] S. C. C. Barros et al. "WASP-38b: a transiting exoplanet in an eccentric, 6.87d period orbit". In: *A & A* 525 (Jan. 2011), A54+. DOI: 10.1051/0004-6361/201015800. arXiv:1010.0849 [astro-ph.EP].

[27] S. S. Barshay and J. S. Lewis. "Chemistry of primitive solar material". In: *Annu. Rev. Astron. Astrophys.* 14 (1976), pp. 81–94. DOI: 10.1146/annurev.aa.14.090176.000501.

[28] C. Baruteau and F. Masset. "Recent developments in planet migration theory". In: *Tidal effects in Astronomy and Astrophysics*. Lecture Notes in Physics. Springer, Mar. 2012. arXiv:1203.3294 [astro-ph.EP].

[29] N. M. Batalha et al. "Planetary Candidates Observed by Kepler. III. Analysis of the First 16 Months of Data". In: *ApJS* 204, 24 (Feb. 2013), p. 24. DOI: 10.1088/0067-0049/204/2/24. arXiv:1202.5852 [astro-ph.EP].

[30] I. M. Beerer et al. "Secondary Eclipse Photometry of WASP-4b with Warm Spitzer". In: *ApJ* 727, 23 (Jan. 2011), p. 23. DOI: 10.1088/0004-637X/727/1/23. arXiv:1011.4066 [astro-ph.EP].

[31] P. Bodenheimer, G. Laughlin, and D. N. C. Lin. "On the Radii of Extrasolar Giant Planets". In: *ApJ* 592 (July 2003), pp. 555–563. DOI: 10.1086/375565. eprint: arXiv:astro-ph/0303541.

[32] P. Bodenheimer, D. N. C. Lin, and R. A. Mardling. "On the Tidal Inflation of Short-Period Extrasolar Planets". In: *ApJ* 548 (Feb. 2001), pp. 466–472. DOI: 10.1086/318667.

[33] A. C. Boley. "The Two Modes of Gas Giant Planet Formation". In: *ApJL* 695 (Apr. 2009), pp. L53–L57. DOI: 10.1088/0004-637X/695/1/L53. arXiv:0902.3999 [astro-ph.EP].

[34] E. Bolmont et al. "Effect of the stellar spin history on the tidal evolution of close-in planets". In: *A & A* 544, A124 (Aug. 2012), A124. DOI: 10.1051/0004-6361/201219645. arXiv:1207.2127 [astro-ph.EP].

[35] A. S. Bonomo et al. "Transiting exoplanets from the CoRoT space mission. X. CoRoT-10b: a giant planet in a 13.24 day eccentric orbit". In: *A & A* 520 (Sept. 2010), A65+. DOI: 10.1051/0004-6361/201014943.

[36] A. P. Boss. "Giant planet formation by gravitational instability." In: *Science* 276 (1997), pp. 1836–1839. DOI: 10.1126/science.276.5320.1836.

[37] F. Bouchy and The Sophie Team. "SOPHIE: the successor of the spectrograph ELODIE for extrasolar planet search and characterization". In: *Tenth Anniversary of 51 Peg-b: Status of and prospects for hot Jupiter studies*. Ed. by L. Arnold, F. Bouchy, & C. Moutou. Feb. 2006, pp. 319–325.

[38] F. Bouchy et al. *Charge Transfer Inefficiency effect for high-precision radial velocity measurements*. Ed. by P. Kern. Vol. 37. EAS Publications Series. EDP Sciences, 2009, pp. 247–253. DOI: 10.1051/eas/0937031.

[39] F. Bouchy et al. "ELODIE metallicity-biased search for transiting Hot Jupiters. II. A very hot Jupiter transiting the bright K star HD 189733". In: *A & A* 444 (Dec. 2005), pp. L15–L19. DOI: 10.1051/0004-6361:200500201.

[40] F. Bouchy et al. "SOPHIE velocimetry of Kepler transit candidates. III. KOI-423b: an 18 M_{Jup} transiting companion around an F7IV star". In: *A & A* 533, A83 (Sept. 2011), A83. DOI: 10.1051/0004-6361/201117095. arXiv:1106.3225 [astro-ph.EP].

[41] F. Bouchy et al. "The SOPHIE search for northern extrasolar planets . I. A companion around HD 16760 with mass close to the planet/brown-dwarf transition". In: *AAP* 505 (Oct. 2009), pp. 853–858. DOI: 10.1051/0004-6361/200912427.

[42] L. A. Buchhave et al. "HAT-P-16b: A 4 M $_J$ Planet Transiting a Bright Star on an Eccentric Orbit". In: *ApJ* 720 (Sept. 2010), pp. 1118–1125. DOI: 10.1088/0004-637X/720/2/1118. arXiv:1005.2009 [astro-ph.EP].

[43] L. A. Buchhave et al. "Kepler-14b: A Massive Hot Jupiter Transiting an F Star in a Close Visual Binary". In: *ApJS* 197, 3 (Nov. 2011), p. 3. DOI: 10.1088/0067-0049/197/1/3. arXiv:1106.5510 [astro-ph.EP].

[44] C. J. Burke et al. "XO-2b: Transiting Hot Jupiter in a Metal-rich Common Proper Motion Binary". In: *APJ* 671 (Dec. 2007), pp. 2115–2128. DOI: 10.1086/523087. arXiv:0705.0003.

[45] R. P. Butler et al. "A Neptune-Mass Planet Orbiting the Nearby M Dwarf GJ 436". In: *ApJ* 617 (Dec. 2004), pp. 580–588. DOI: 10.1086/425173. eprint: arXiv:astro-ph/0408587.

[46] R. P. Butler et al. "Catalog of Nearby Exoplanets". In: *ApJ* 646 (July 2006), pp. 505–522. DOI: 10.1086/504701. eprint: arXiv:astro-ph/0607493.

[47] C. J. Campo et al. "On the Orbit of Exoplanet WASP-12b". In: *ApJ* 727 (Feb. 2011), pp. 125–+. DOI: 10.1088/0004-637X/727/2/125. arXiv:1003.2763 [astro-ph.EP].

[48] L. Carone and M. Pätzold. "Constraints on the tidal dissipation factor of a main sequence star: The case of OGLE-TR-56b". In: *Planet. Space Sci.* 55 (Apr. 2007), pp. 643–650. DOI: 10.1016/j.pss.2006.05.044.

[49] D. Charbonneau et al. "Detection of Planetary Transits Across a Sun-like Star". In: *The Astrophysical Journal Letters* 529.1 (2000), pp. L45–L48. URL: http://stacks.iop.org/1538-4357/529/L45.

[50] S. Chatterjee et al. "Dynamical Outcomes of Planet-Planet Scattering". In: *ApJ* 686 (Oct. 2008), pp. 580–602. DOI: 10.1086/590227. eprint: arXiv:astro-ph/0703166.

[51] S. Chib and E. Greenberg. "Understanding the Metropolis-Hastings Algorithm". In: *The American Statistician* 49.4 (1995), pp. 327–335. DOI: 10.2307/2684568. URL: http://dx.doi.org/10.2307/2684568.

[52] D. J. Christian et al. "WASP-10b: a 3M$_J$, gas-giant planet transiting a late-type K star". In: *MNRAS* 392 (Feb. 2009), pp. 1585–1590. DOI: 10.1111/j.1365-2966.2008.14164.x. arXiv:0806.1482.

[53] A. Claret. "A new non-linear limb-darkening law for LTE stellar atmosphere models". In: *AAP* 428 (Dec. 2004), pp. 1001–1005. DOI: 10.1051/0004-6361:20041673. URL: http://vizier.cfa.harvard.edu/viz-bin/VizieR?-source=J/A+A/428/1001.

[54] A. Claret. "Non-linear limb-darkening law for LTE models. III. (Claret, 2004)". In: *VizieR Online Data Catalog* 342 (Oct. 2004), p. 81001. URL: http://vizier.cfa.harvard.edu/viz-bin/VizieR?-source=J/A+A/428/1001.

[55] W. D. Cochran et al. "The Discovery of a Planetary Companion to 16 Cygni B". In: *ApJ* 483 (July 1997), p. 457. DOI: 10.1086/304245. eprint: arXiv:astro-ph/9611230.

[56] A. Collier Cameron et al. "WASP-1b and WASP-2b: two new transiting exoplanets detected with SuperWASP and SOPHIE". In: *MNRAS* 375 (Mar. 2007), pp. 951–957. DOI: 10.1111/j.1365-2966.2006.11350.x. eprint: arXiv:astro-ph/0609688.

[57] N. Copernicus. *De revolutionibus orbium coelestium / Nicolaus Copernicus*. Johnson Reprint Corporation, New York, 1965, First Published: 1543.

[58] T. G. Cowling. "The non-radial oscillations of polytropic stars". In: *MNRAS* 101 (1941), p. 367.

[59] P. Cresswell et al. "On the evolution of eccentric and inclined protoplanets embedded in protoplanetary disks". In: *A&A* 473.1 (2007), pp. 329–342. DOI: 10.1051/0004-6361:20077666. URL: http://dx.doi.org/10.1051/0004-6361:20077666.

[60] G. H. Darwin. "A tidal theory of the evolution of satellites". In: *The Observatory* 3 (July 1879), pp. 79–84.

[61] G. H. Darwin. "On the Harmonic Analysis of Tidal Observations of High and Low Water". In: *Proceedings of the Royal Society of London* 48 (1890), pp. 278–340.

[62] G. H. Darwin. "On the Secular Changes in the Elements of the Orbit of a Satellite Revolving About a Planet Distorted by Tides". In: *Nature* 21 (Jan. 1880), pp. 235–237. DOI: 10.1038/021235a0.

[63] H. J. Deeg et al. "A transiting giant planet with a temperature between 250K and 430K". In: *Nature* 464 (Mar. 2010), pp. 384–387. DOI: 10.1038/nature08856.

[64] M. Deleuil et al. "Transiting exoplanets from the CoRoT space mission. XX. CoRoT-20b: A very high density, high eccentricity transiting giant planet". In: *A & A* 538, A145 (Feb. 2012), A145. DOI: 10.1051/0004-6361/201117681.

[65] D. Deming et al. "Spitzer Transit and Secondary Eclipse Photometry of GJ 436b". In: *ApJL* 667 (Oct. 2007), pp. L199–L202. DOI: 10.1086/522496. arXiv:0707.2778.

[66] S. Desidera and M. Barbieri. "Properties of planets in binary systems. The role of binary separation". In: *A & A* 462 (Jan. 2007), pp. 345–353. DOI: 10.1051/0004-6361:20066319. eprint: arXiv:astro-ph/0610623.

[67] R. F. Díaz et al. "SOPHIE velocimetry of Kepler transit candidates. VIII. KOI-205 b: a brown-dwarf companion to a K-type dwarf". In: *A & A* 551, L9 (Mar. 2013), p. L9. DOI: 10.1051/0004-6361/201321124. arXiv:1302.2628 [astro-ph.EP].

[68] I. Dobbs-Dixon et al. "Spin-Orbit Evolution of Short-Period Planets". In: *The Astrophysical Journal* 610.1 (2004), pp. 464–476. URL: http://stacks.iop.org/0004-637X/610/464.

[69] J. Eastman, B. S. Gaudi, and E. Agol. "EXOFAST: A Fast Exoplanetary Fitting Suite in IDL". In: *PASP* 125 (Jan. 2013), pp. 83–112. DOI: 10.1086/669497. arXiv:1206.5798 [astro-ph.IM].

[70] M. Efroimsky and J. G. Williams. "Tidal torques: a critical review of some techniques". In: *Celestial Mechanics and Dynamical Astronomy* 104 (July 2009), pp. 257–289. DOI: 10.1007/s10569-009-9204-7. arXiv:0803.3299.

[71] P. P. Eggleton, L. G. Kiseleva, and P. Hut. "The Equilibrium Tide Model for Tidal Friction". In: *ApJ* 499 (May 1998), pp. 853–+. DOI: 10.1086/305670. eprint: arXiv:astro-ph/9801246.

[72] P. P. Eggleton and L. Kisseleva-Eggleton. "A Mechanism for Producing Short-Period Binaries". In: *Ap & SS* 304 (Aug. 2006), pp. 75–79. DOI: 10.1007/s10509-006-9078-z.

[73] B. Enoch et al. "WASP-25b: a 0.6 M_J planet in the Southern hemisphere". In: *MNRAS* 410 (Jan. 2011), pp. 1631–1636. DOI: 10.1111/j.1365-2966.2010.17550.x. arXiv:1009.5917 [astro-ph.EP].

[74] J. A. Faber, F. A. Rasio, and B. Willems. "Tidal interactions and disruptions of giant planets on highly eccentric orbits". In: *Icarus* 175 (May 2005), pp. 248–262. DOI: 10.1016/j.icarus.2004.10.021. eprint: arXiv:astro-ph/0407318.

[75] D. Fabrycky and S. Tremaine. "Shrinking Binary and Planetary Orbits by Kozai Cycles with Tidal Friction". In: *ApJ* 669 (Nov. 2007), pp. 1298–1315. DOI: 10.1086/521702. arXiv:0705.4285.

[76] D. C. Fabrycky and J. N. Winn. "Exoplanetary Spin-Orbit Alignment: Results from the Ensemble of Rossiter-McLaughlin Observations". In: *ApJ* 696 (May 2009), pp. 1230–1240. DOI: 10.1088/0004-637X/696/2/1230. arXiv:0902.0737 [astro-ph.EP].

[77] J. M. Fernandez et al. "The Transit Light Curve Project. XII. Six Transits of the Exoplanet XO-2b". In: *AJ* 137 (June 2009), pp. 4911–4916. DOI: 10.1088/0004-6256/137/6/4911. arXiv:0903.2687.

[78] S. Ferraz-Mello, A. Rodríguez, and H. Hussmann. "Tidal friction in close-in satellites and exoplanets: The Darwin theory re-visited". In: *Celestial Mechanics and Dynamical Astronomy* 101 (May 2008), pp. 171–201. DOI: 10.1007/s10569-008-9133-x. arXiv:0712.1156.

[79] E. B. Ford. "Improving the Efficiency of Markov Chain Monte Carlo for Analyzing the Orbits of Extrasolar Planets". In: *ApJ* 642 (May 2006), pp. 505–522. DOI: 10.1086/500802. eprint: arXiv:astro-ph/0512634.

[80] E. B. Ford, M. Havlickova, and F. A. Rasio. "Dynamical Instabilities in Extrasolar Planetary Systems Containing Two Giant Planets". In: *Icarus* 150 (Apr. 2001), pp. 303–313. DOI: 10.1006/icar.2001.6588. eprint: arXiv:astro-ph/0010178.

[81] E. B. Ford, B. Kozinsky, and F. A. Rasio. "Secular Evolution of Hierarchical Triple Star Systems". In: *ApJ* 535 (May 2000), pp. 385–401. DOI: 10.1086/308815.

[82] E. B. Ford and F. A. Rasio. "On the Relation between Hot Jupiters and the Roche Limit". In: *ApJL* 638 (Feb. 2006), pp. L45–L48. DOI: 10.1086/500734. eprint: arXiv:astro-ph/0512632.

[83] E. B. Ford and F. A. Rasio. "Origins of Eccentric Extrasolar Planets: Testing the Planet-Planet Scattering Model". In: *ApJ* 686 (Oct. 2008), pp. 621–636. DOI: 10.1086/590926. eprint: arXiv:astro-ph/0703163.

[84] E. B. Ford, F. A. Rasio, and K. Yu. "Dynamical Instabilities in Extrasolar Planetary Systems". In: *Scientific Frontiers in Research on Extrasolar Planets*. Ed. by D. Deming and S. Seager. Vol. 294. Astronomical Society of the Pacific Conference Series. 2003, pp. 181–188. eprint: arXiv:astro-ph/0210275.

[85] L. Fossati et al. "A Detailed Spectropolarimetric Analysis of the Planet-hosting Star WASP-12". In: *ApJ* 720 (Sept. 2010), pp. 872–886. DOI: 10.1088/0004-637X/720/1/872.

[86] L. Fossati et al. "Metals in the Exosphere of the Highly Irradiated Planet WASP-12b". In: *ApJL* 714 (May 2010), pp. L222–L227. DOI: 10.1088/2041-8205/714/2/L222. arXiv:1005.3656 [astro-ph.SR].

[87] S. V. Gavrilov and V. N. Zharkov. "Love numbers of the giant planets". In: *Icarus* 32 (Dec. 1977), pp. 443–449. DOI: 10.1016/0019-1035(77)90015-X.

[88] M. Gillon et al. "Discovery and characterization of WASP-6b, an inflated sub-Jupiter mass planet transiting a solar-type star". In: *A & A* 501 (July 2009), pp. 785–792. DOI: 10.1051/0004-6361/200911749. arXiv:0901.4705.

[89] M. Gillon et al. "Improved parameters for the transiting hot Jupiters WASP-4b and WASP-5b". In: *Astronomy and Astrophysics* 496 (2009), pp. 259–267.

[90] M. Gillon et al. "WASP-50 b: a hot Jupiter transiting a moderately active solar-type star". In: *A & A* 533, A88 (Sept. 2011), A88. DOI: 10.1051/0004-6361/201117198. arXiv:1108.2641 [astro-ph.EP].

[91] A. Giménez. "Equations for the Analysis of the Rossiter-McLaughlin Effect in Extrasolar Planetary Transits". In: *ApJ* 650 (Oct. 2006), pp. 408–413. DOI: 10.1086/507021.

[92] L. Girardi et al. "Theoretical isochrones in several photometric systems. I. Johnson-Cousins-Glass, HST/WFPC2, HST/NICMOS, Washington, and ESO Imaging Survey filter sets". In: *A & A* 391 (Aug. 2002), pp. 195–212. DOI: 10.1051/0004-6361:20020612. eprint: arXiv:astro-ph/0205080.

[93] P. Goldreich. "On the eccentricity of satellite orbits in the solar system". In: *MNRAS* 126 (1963), pp. 257–+.

[94] P. Goldreich and P. D. Nicholson. "Tidal friction in early-type stars". In: *ApJ* 342 (July 1989), pp. 1079–1084. DOI: 10.1086/167665.

[95] P. Goldreich and S. Soter. "Q in the Solar System". In: *Icarus* 5 (1966), pp. 375–389. DOI: 10.1016/0019-1035(66)90051-0.

[96] P. Goldreich and S. Tremaine. "Disk-satellite interactions". In: *ApJ* 241 (Oct. 1980), pp. 425–441. DOI: 10.1086/158356.

[97] J. Goodman and E. S. Dickson. "Dynamical Tide in Solar-Type Binaries". In: *ApJ* 507 (Nov. 1998), pp. 938–944. DOI: 10.1086/306348. eprint: arXiv:astro-ph/9801289.

[98] R. Greenberg. "Frequency Dependence of Tidal q". In: *ApJL* 698 (June 2009), pp. L42–L45. DOI: 10.1088/0004-637X/698/1/L42.

[99] P. Gregory. *Bayesian Logical Data Analysis for the Physical Sciences*. Cambridge University Press, 2005.

[100] T. Guillot et al. *The interior of Jupiter*. Ed. by F. Bagenal, T. E. Dowling, and W. B. McKinnon. 2004, pp. 35–57.

[101] J. L. Halbwachs, M. Mayor, and S. Udry. "Statistical properties of exoplanets. IV. The period-eccentricity relations of exoplanets and of binary stars". In: *A & A* 431 (Mar. 2005), pp. 1129–1137. DOI: 10.1051/0004-6361:20041219. eprint: arXiv:astro-ph/0410732.

[102] B. M. S. Hansen. "Calibration of Equilibrium Tide Theory for Extrasolar Planet Systems". In: *ApJ* 723 (Nov. 2010), pp. 285–299. DOI: 10.1088/0004-637X/723/1/285. arXiv:1009.3027 [astro-ph.SR].

[103] B. M. S. Hansen. "Calibration of Equilibrium Tide Theory for Extrasolar Planet Systems. II". In: *ApJ* 757, 6 (Sept. 2012), p. 6. DOI: 10.1088/0004-637X/757/1/6. arXiv:1204.3903 [astro-ph.EP].

[104] C. A. Haswell et al. "Near-ultraviolet Absorption, Chromospheric Activity, and Star-Planet Interactions in the WASP-12 system". In: *ApJ* 760, 79 (Nov. 2012), p. 79. DOI: 10.1088/0004-637X/760/1/79. arXiv:1301.1860 [astro-ph.EP].

[105] L. Hebb et al. "WASP-12b: THE HOTTEST TRANSITING EXTRASOLAR PLANET YET DISCOVERED". In: *The Astrophysical Journal* 693.2 (2009), pp. 1920–1928. URL: http://stacks.iop.org/0004-637X/693/1920.

[106] L. Hebb et al. "WASP-19b: The Shortest Period Transiting Exoplanet Yet Discovered". In: *ApJ* 708 (Jan. 2010), pp. 224–231. DOI: 10.1088/0004-637X/708/1/224. arXiv:1001.0403.

[107] G. Hébrard et al. "Misaligned spin-orbit in the XO-3 planetary system?" In: *A & A* 488 (Sept. 2008), pp. 763–770. DOI: 10.1051/0004-6361:200810056. arXiv:0806.0719.

[108] G. Hébrard et al. "Observation of the full 12-hour-long transit of the exoplanet HD 80606b. Warm-Spitzer photometry and SOPHIE spectroscopy". In: *A & A* 516, A95 (June 2010), A95. DOI: 10.1051/0004-6361/201014327. arXiv:1004.0790 [astro-ph.EP].

[109] G. Hébrard et al. "Transiting exoplanets from the CoRoT space mission. XVIII. CoRoT-18b: a massive hot Jupiter on a prograde, nearly aligned orbit". In: *A & A* 533, A130 (Sept. 2011), A130. DOI: 10.1051/0004-6361/201117192. arXiv:1107.2032 [astro-ph.EP].

[110] G. Hébrard et al. "WASP-52b, WASP-58b, WASP-59b, and WASP-60b: Four new transiting close-in giant planets". In: *A & A* 549, A134 (Jan. 2013), A134. DOI: 10.1051/0004-6361/201220363. arXiv:1211.0810 [astro-ph.EP].

[111] C. Hellier et al. "An orbital period of 0.94days for the hot-Jupiter planet WASP-18b". In: *Nature* 460 (Aug. 2009), pp. 1098–1100. DOI: 10.1038/nature08245.

[112] C. Hellier et al. "WASP-29b: A Saturn-sized Transiting Exoplanet". In: *ApJL* 723 (Nov. 2010), pp. L60–L63. DOI: 10.1088/2041-8205/723/1/L60. arXiv:1009.5318 [astro-ph.EP].

[113] C. Hellier et al. "WASP-43b: the closest-orbiting hot Jupiter". In: *A & A* 535, L7 (Nov. 2011), p. L7. DOI: 10.1051/0004-6361/201117081. arXiv:1104.2823 [astro-ph.EP].

[114] C. Hellier et al. "WASP-7: A BRIGHT TRANSITING-EXOPLANET SYSTEM IN THE SOUTHERN HEMISPHERE". In: *The Astrophysical Journal Letters* 690.1 (2009), pp. L89–L91. URL: http://stacks.iop.org/1538-4357/690/L89.

[115] M. Holman, J. Touma, and S. Tremaine. "Chaotic variations in the eccentricity of the planet orbiting 16 Cygni B". In: *Nature* 386 (Mar. 1997), pp. 254–256. DOI: 10.1038/386254a0.

[116] M. J. Holman and P. A. Wiegert. "Long-Term Stability of Planets in Binary Systems". In: *AJ* 117 (Jan. 1999), pp. 621–628. DOI: 10.1086/300695. eprint: arXiv:astro-ph/9809315.

[117] M. J. Holman et al. "The Transit Light Curve Project. I. Four Consecutive Transits of the Exoplanet XO-1b". In: *ApJ* 652 (Dec. 2006), pp. 1715–1723. DOI: 10.1086/508155. eprint: arXiv:astro-ph/0607571.

[118] A. W. Howard et al. "HAT-P-17b,c: A Transiting, Eccentric, Hot Saturn and a Long-period, Cold Jupiter". In: *ApJ* 749, 134 (Apr. 2012), p. 134. DOI: 10.1088/0004-637X/749/2/134. arXiv:1008.3898 [astro-ph.EP].

[119] N. Husnoo et al. "Observational constraints on tidal effects using orbital eccentricities". In: *MNRAS* 422 (June 2012), pp. 3151–3177. DOI: 10.1111/j.1365-2966.2012.20839.x. arXiv:1202.6379 [astro-ph.EP].

[120] N. Husnoo et al. "Orbital eccentricity of WASP-12 and WASP-14 from new radial velocity monitoring with SOPHIE". In: *MNRAS* 413 (June 2011), pp. 2500–2508. DOI: 10.1111/j.1365-2966.2011.18322.x. arXiv:1004.1809 [astro-ph.EP].

[121] P. Hut. "Stability of tidal equilibrium". In: *A & A* 92 (Dec. 1980), pp. 167–170.

[122] P. Hut. "Tidal evolution in close binary systems". In: *A & A* 99 (June 1981), pp. 126–140.

[123] L. Ibgui, A. Burrows, and D. S. Spiegel. "Tidal Heating Models for the Radii of the Inflated Transiting Giant Planets WASP-4b, WASP-6b, WASP-12b, WASP-15b, and TrES-4". In: *ApJ* 713 (Apr. 2010), pp. 751–763. DOI: 10.1088/0004-637X/713/2/751. arXiv:0910.4394 [astro-ph.EP].

[124] S. Ida and D. N. C. Lin. "Toward a Deterministic Model of Planetary Formation. I. A Desert in the Mass and Semimajor Axis Distributions of Extrasolar Planets". In: *ApJ* 604 (Mar. 2004), pp. 388–413. DOI: 10.1086/381724. eprint: arXiv:astro-ph/0312144.

[125] International Astronomical Union. *Definition of a Planet in the Solar System*. 2006. URL: http://www.iau.org/administration/resolutions/general_assemblies/.

[126] P. B. Ivanov and J. C. B. Papaloizou. "On equilibrium tides in fully convective planets and stars". In: *MNRAS* 353 (Oct. 2004), pp. 1161–1175. DOI: 10.1111/j.1365-2966.2004.08136.x. eprint: arXiv:astro-ph/0312593.

[127] B. Jackson, R. Greenberg, and R. Barnes. "Tidal Evolution of Close-in Extrasolar Planets". In: *Apj* 678 (May 2008), pp. 1396–1406. DOI: 10.1086/529187. arXiv:0802.1543.

[128] B. Jackson, R. Greenberg, and R. Barnes. "Tidal Heating of Extrasolar Planets". In: *ApJ* 681 (July 2008), pp. 1631–1638. DOI: 10.1086/587641. arXiv:0803.0026.

[129] J. H. Jeans; *Astronomy and cosmogony*. Cambridge University Press, 1929.

[130] J. A. Johnson et al. "A Third Exoplanetary System with Misaligned Orbital and Stellar Spin Axes". In: *Publications of the Astronomical Society of the Pacific* 121.884 (2009), pp. 1104–1111. DOI: 10.1086/644604. eprint: http://www.journals.uchicago.edu/doi/pdf/10.1086/644604. URL: http://www.journals.uchicago.edu/doi/abs/10.1086/644604.

[131] J. A. Johnson et al. "HAT-P-30b: A Transiting Hot Jupiter on a Highly Oblique Orbit". In: *ApJ* 735 (July 2011), pp. 24–+. DOI: 10.1088/0004-637X/735/1/24. arXiv:1103.3825 [astro-ph.EP].

[132] Y. C. Joshi et al. "WASP-14b: 7.3 M_J transiting planet in an eccentric orbit". In: *MNRAS* 392 (Feb. 2009), pp. 1532–1538. DOI: 10.1111/j.1365-2966.2008.14178.x. arXiv:0806.1478.

[133] M. Jurić and S. Tremaine. "Dynamical Origin of Extrasolar Planet Eccentricity Distribution". In: *ApJ* 686 (Oct. 2008), pp. 603–620. DOI: 10.1086/590047. eprint: arXiv:astro-ph/0703160.

[134] R. E. Kass and A. E. Raftery. "Bayes Factors". English. In: *Journal of the American Statistical Association* 90.430 (1995), pp. 773–795. ISSN: 01621459. URL: http://www.jstor.org/stable/2291091.

[135] D. Kipping and G. Bakos. "An Independent Analysis of Kepler-4b Through Kepler-8b". In: *ApJ* 730 (Mar. 2011), pp. 50–+. DOI: 10.1088/0004-637X/730/1/50. arXiv:1004.3538 [astro-ph.EP].

[136] D. M. Kipping et al. "HAT-P-31b,c: A Transiting, Eccentric, Hot Jupiter and a Long-period, Massive Third Body". In: *AJ* 142, 95 (Sept. 2011), p. 95. DOI: 10.1088/0004-6256/142/3/95. arXiv:1106.1169 [astro-ph.EP].

[137] L. G. Kiseleva, P. P. Eggleton, and S. Mikkola. "Tidal friction in triple stars". In: *MNRAS* 300 (Oct. 1998), pp. 292–302. DOI: 10.1046/j.1365-8711.1998.01903.x.

[138] W. Kley, J. Peitz, and G. Bryden. "Evolution of planetary systems in resonance". In: *A & A* 414 (Feb. 2004), pp. 735–747. DOI: 10.1051/0004-6361:20031589. eprint: arXiv:astro-ph/0310321.

[139] G. Kovács et al. "HAT-P-15b: A 10.9 Day Extrasolar Planet Transiting a Solar-type Star". In: *ApJ* 724 (Dec. 2010), pp. 866–877. DOI: 10.1088/0004-637X/724/2/866. arXiv:1005.5300 [astro-ph.EP].

[140] G. Kovacs et al. "HAT-P-4b: A Metal-rich Low-Density Transiting Hot Jupiter". In: *The Astrophysical Journal Letters* 670.1 (2007), pp. L41–L44. URL: http://stacks.iop.org/1538-4357/670/L41.

[141] Y. Kozai. "Secular perturbations of asteroids with high inclination and eccentricity". In: *AJ* 67 (Nov. 1962), p. 591. DOI: 10.1086/108790.

[142] A.-M. Lagrange et al. "Extrasolar planets and brown dwarfs around A-F type stars. VI. High precision RV survey of early type dwarfs with HARPS". In: *A & A* 495 (Feb. 2009), pp. 335–352. DOI: 10.1051/0004-6361:200810105. arXiv:0809.4636.

[143] D. Lai. "Tidal dissipation in planet-hosting stars: damping of spin-orbit misalignment and survival of hot Jupiters". In: *MNRAS* 423 (June 2012), pp. 486–492. DOI: 10.1111/j.1365-2966.2012.20893.x. arXiv:1109.4703 [astro-ph.EP].

[144] G. Laughlin et al. "On the Eccentricity of HD 209458b". In: *The Astrophysical Journal Letters* 629.2 (2005), p. L121. URL: http://stacks.iop.org/1538-4357/629/i=2/a=L121.

[145] M. Lecar, J. C. Wheeler, and C. F. McKee. "Tidal circularization of the binary X-ray sources Hercules X-1 and Centaurus X-3". In: *ApJ* 205 (Apr. 1976), pp. 556–562. DOI: 10.1086/154311.

[146] J. Leconte et al. "Is tidal heating sufficient to explain bloated exoplanets? Consistent calculations accounting for finite initial eccentricity". In: *A & A* 516 (June 2010), A64+. DOI: 10.1051/0004-6361/201014337. arXiv:1004.0463 [astro-ph.EP].

[147] M. H. Lee and S. J. Peale. "Dynamics and Origin of the 2:1 Orbital Resonances of the GJ 876 Planets". In: *ApJ* 567 (Mar. 2002), pp. 596–609. DOI: 10.1086/338504.

[148] H. F. Levison, J. J. Lissauer, and M. J. Duncan. "Modeling the Diversity of Outer Planetary Systems". In: *AJ* 116 (Oct. 1998), pp. 1998–2014. DOI: 10.1086/300557.

[149] S.-L. Li et al. "WASP-12b as a prolate, inflated and disrupting planet from tidal dissipation". In: *Nature* 463 (Feb. 2010), pp. 1054–1056. DOI: 10.1038/nature08715. arXiv:1002.4608 [astro-ph.EP].

[150] M. L. Lidov. "The evolution of orbits of artificial satellites of planets under the action of gravitational perturbations of external bodies". In: *Planet. Space Sci.* 9 (Oct. 1962), pp. 719–759. DOI: 10.1016/0032-0633(62)90129-0.

[151] D. N. C. Lin, P. Bodenheimer, and D. C. Richardson. "Orbital migration of the planetary companion of 51 Pegasi to its present location". In: *Nature* 380 (Apr. 1996), pp. 606–607. DOI: 10.1038/380606a0.

[152] D. N. C. Lin and J. Papaloizou. "On the tidal interaction between protoplanets and the protoplanetary disk. III - Orbital migration of protoplanets". In: *ApJ* 309 (Oct. 1986), pp. 846–857. DOI: 10.1086/164653.

[153] J. J. Lissauer. "Planet formation". In: *Annu. Rev. Astron. Astrophys.* 31 (1993), pp. 129–174. DOI: 10.1146/annurev.aa.31.090193.001021.

[154] B. Loeillet et al. "Refined parameters and spectroscopic transit of the super-massive planet HD 147506b". In: *AAP* 481 (Apr. 2008), pp. 529–533. DOI: 10.1051/0004-6361:20078167. arXiv:0707.0679.

[155] M. López-Morales et al. "Day-side z'-band Emission and Eccentricity of WASP-12b". In: *ApJL* 716 (June 2010), pp. L36–L40. DOI: 10.1088/2041-8205/716/1/L36. arXiv:0912.2359 [astro-ph.EP].

[156] S. H. Lubow and G. I. Ogilvie. "Secular Interactions between Inclined Planets and a Gaseous Disk". In: *ApJ* 560 (Oct. 2001), pp. 997–1009. DOI: 10.1086/322493. eprint: arXiv:astro-ph/0106453.

[157] L. B. Lucy and M. A. Sweeney. "Spectroscopic binaries with circular orbits." In: *AJ* 76 (Aug. 1971), pp. 544–556. DOI: 10.1086/111159.

[158] G. J. F. MacDonald. "Tidal Friction". In: *Reviews of Geophysics and Space Physics* 2 (1964), pp. 467–541. DOI: 10.1029/RG002i003p00467.

[159] G. Maciejewski et al. "Transit timing variation and activity in the WASP-10 planetary system". In: *MNRAS* 411 (Feb. 2011), pp. 1204–1212. DOI: 10.1111/j.1365-2966.2010.17753.x. arXiv:1009.4567 [astro-ph.EP].

[160] D. Malmberg, M. B. Davies, and J. E. Chambers. "The instability of planetary systems in binaries: how the Kozai mechanism leads to strong planet-planet interactions". In: *MNRAS* 377 (Apr. 2007), pp. L1–L4. DOI: 10.1111/j.1745-3933.2007.00291.x. eprint: arXiv:astro-ph/0612041.

[161] K. Mandel and E. Agol. "Analytic Light Curves for Planetary Transit Searches". In: *ApJL* 580 (Dec. 2002), pp. L171–L175. DOI: 10.1086/345520. eprint: arXiv:astro-ph/0210099.

[162] H. L. Maness et al. "The M Dwarf GJ 436 and its Neptune-Mass Planet". In: *PASP* 119 (Jan. 2007), pp. 90–101. DOI: 10.1086/510689. eprint: arXiv:astro-ph/0608260.

[163] G. Marcy et al. "Observed Properties of Exoplanets: Masses, Orbits, and Metallicities". In: *Progress of Theoretical Physics Supplement* 158 (2005), pp. 24–42. DOI: 10.1143/PTPS.158.24. eprint: arXiv:astro-ph/0505003.

[164] G. W. Marcy et al. "Exoplanet properties from Lick, Keck and AAT". In: *Physica Scripta Volume T* 130.1 (Aug. 2008), p. 014001. DOI: 10.1088/0031-8949/2008/T130/014001.

[165] F. Marzari and S. J. Weidenschilling. "Eccentric Extrasolar Planets: The Jumping Jupiter Model". In: *Icarus* 156 (Apr. 2002), pp. 570–579. DOI: 10.1006/icar.2001.6786.

[166] F. Marzari et al. "Jumping Jupiters in Binary Star Systems". In: *ApJ* 618 (Jan. 2005), pp. 502–511. DOI: 10.1086/425976.

[167] R. D. Mathieu and T. Mazeh. "The circularized binaries in open clusters - A new clock for age determination". In: *ApJ* 326 (Mar. 1988), pp. 256–264. DOI: 10.1086/166087.

[168] P. F. L. Maxted et al. "WASP-32b: A Transiting Hot Jupiter Planet Orbiting a Lithium-Poor, Solar-Type Star". In: *PASP* 122 (Dec. 2010), pp. 1465–1470. DOI: 10.1086/657658. arXiv:1010.1742 [astro-ph.EP].

[169] M. Mayor and D. Queloz. "A Jupiter-mass companion to a solar-type star". In: *Nature* 378 (Nov. 1995), pp. 355–359. DOI: 10.1038/378355a0.

[170] M. Mayor et al. "51 Pegasi". In: *IAU Circ* 6251 (Oct. 1995), pp. 1–+.

[171] M. Mayor et al. "Setting New Standards with HARPS". In: *The Messenger* 114 (Dec. 2003), pp. 20–24.

[172] T. Mazeh. "Observational Evidence for Tidal Interaction in Close Binary Systems". In: *EAS Publications Series*. Ed. by M.-J. Goupil & J.-P. Zahn. Vol. 29. EAS Publications Series. 2008, pp. 1–65. DOI: 10.1051/eas:0829001.

[173] T. Mazeh and S. Faigler. "Detection of the ellipsoidal and the relativistic beaming effects in the CoRoT-3 lightcurve". In: *A & A* 521, L59 (Oct. 2010), p. L59. DOI: 10.1051/0004-6361/201015550. arXiv:1008.3028 [astro-ph.EP].

[174] T. Mazeh, Y. Krymolowski, and G. Rosenfeld. "The High Eccentricity of the Planet Orbiting 16 Cygni B". In: *ApJL* 477 (Mar. 1997), pp. L103+. DOI: 10.1086/310536. eprint: arXiv:astro-ph/9611135.

[175] T. Mazeh, S. Zucker, and F. Pont. "An intriguing correlation between the masses and periods of the transiting planets". In: *MNRAS* 356 (Jan. 2005), pp. 955–957. DOI: 10.1111/j.1365-2966.2004.08511.x. eprint: arXiv:astro-ph/0411701.

[176] T. Mazeh et al. *Study of dynamical and tidal evolution of transiting extrasolar planets by additional RV measurements with HARPS*. ESO Prog. 0812.C-0312. 2008. URL: http://archive.eso.org/wdb/wdb/eso/sched_rep_arc/query?progid=082.C-0312.

[177] D. B. McLaughlin. "Some results of a spectrographic study of the Algol system." In: *ApJ* 60 (July 1924), pp. 22–31. DOI: 10.1086/142826.

[178] H. Mizuno. "Formation of the Giant Planets". In: *Progress of Theoretical Physics* 64 (Aug. 1980), pp. 544–557. DOI: 10.1143/PTP.64.544.

[179] C.D. Murray and S.F. Dermott. *Solar System Dynamics*. Cambridge University Press, 1999. ISBN: 9780521575973. URL: http://books.google.co.uk/books?id=aU6vcy5L8GAC.

[180] D. Naef et al. "HD 80606 b, a planet on an extremely elongated orbit". In: *A & A* 375 (Aug. 2001), pp. L27–L30. DOI: 10.1051/0004-6361:20010853. eprint: arXiv:astro-ph/0106256.

[181] M. Nagasawa, S. Ida, and T. Bessho. "Formation of Hot Planets by a Combination of Planet Scattering, Tidal Circularization, and the Kozai Mechanism". In: *ApJ* 678 (May 2008), pp. 498–508. DOI: 10.1086/529369. arXiv:0801.1368.

[182] S. Naoz et al. "Hot Jupiters from secular planet-planet interactions". In: *Nature* 473 (May 2011), pp. 187–189. DOI: 10.1038/nature10076. arXiv:1011.2501 [astro-ph.EP].

[183] P. Nutzman et al. "Precise Estimates of the Physical Parameters for the Exoplanet System HD 17156 Enabled by Hubble Space Telescope Fine Guidance Sensor Transit and Asteroseismic Observations". In: *ApJ* 726, 3 (Jan. 2011), p. 3. DOI: 10.1088/0004-637X/726/1/3. arXiv:1011.0440 [astro-ph.EP].

[184] F. T. O'Donovan et al. "TrES-2: The First Transiting Planet in the Kepler Field". In: *ApJL* 651 (Nov. 2006), pp. L61–L64. DOI: 10.1086/509123. eprint: arXiv:astro-ph/0609335.

[185] F. T. O'Donovan et al. "TrES-3: A Nearby, Massive, Transiting Hot Jupiter in a 31 Hour Orbit". In: *The Astrophysical Journal Letters* 663.1 (2007), pp. L37–L40. URL: http://stacks.iop.org/1538-4357/663/L37.

[186] G. I. Ogilvie and D. N. C. Lin. "Tidal Dissipation in Rotating Giant Planets". In: *ApJ* 610 (July 2004), pp. 477–509. DOI: 10.1086/421454. eprint: arXiv:astro-ph/0310218.

[187] G. I. Ogilvie and D. N. C. Lin. "Tidal Dissipation in Rotating Solar-Type Stars". In: *ApJ* 661 (June 2007), pp. 1180–1191. DOI: 10.1086/515435. eprint: arXiv:astro-ph/0702492.

[188] J. P. Ostriker, L. Spitzer Jr., and R. A. Chevalier. "On the Evolution of Globular Clusters". In: *ApJL* 176 (Sept. 1972), p. L51. DOI: 10.1086/181018.

[189] A. Pál et al. "HAT-P-7b: An Extremely Hot Massive Planet Transiting a Bright Star in the Kepler Field". In: *ApJ* 680 (June 2008), pp. 1450–1456. DOI: 10.1086/588010. arXiv:0803.0746.

[190] J. C. B. Papaloizou, R. P. Nelson, and F. Masset. "Orbital eccentricity growth through disc-companion tidal interaction". In: *A & A* 366 (Jan. 2001), pp. 263–275. DOI: 10.1051/0004-6361:20000011.

[191] J. C. B. Papaloizou and G. J. Savonije. "Non-adiabatic tidal forcing of a massive, uniformly rotating star. III - Asymptotic treatment for low frequencies in the inertial regime". In: *MNRAS* 291 (Nov. 1997), p. 651. eprint: arXiv:astro-ph/9706187.

[192] J. C. B. Papaloizou and C. Terquem. "Dynamical relaxation and massive extrasolar planets". In: *MNRAS* 325 (July 2001), pp. 221–230. DOI: 10.1046/j.1365-8711.2001.04386.x. eprint: arXiv:astro-ph/0012391.

[193] I. de Pater and J. J. Lissauer. *Planetary Sciences*. Cambridge University Press, 2001.

[194] S. J. Peale, P. Cassen, and R. T. Reynolds. "Melting of Io by tidal dissipation". In: *Science* 203 (Mar. 1979), pp. 892–894. DOI: 10.1126/science.203.4383.892.

[195] S. Perruchot et al. "The SOPHIE spectrograph: design and technical keypoints for high throughput and high stability". In: *Society of Photo-Optical Instrumentation Engineers (SPIE) Conference Series*. Vol. 7014. Presented at the Society of Photo-Optical Instrumentation Engineers (SPIE) Conference. Aug. 2008. DOI: 10.1117/12.787379.

[196] J. B. Pollack. "Origin and History of the Outer Planets: Theoretical Models and Observations L Contraints". In: *ARAA* 22 (1984), pp. 389–424. DOI: 10.1146/annurev.aa.22.090184.002133.

[197] J. B. Pollack et al. "Formation of the Giant Planets by Concurrent Accretion of Solids and Gas". In: *Icarus* Volume 124, Issue 1 (1996), pp. 62–85.

[198] F. Pont. "Empirical evidence for tidal evolution in transiting planetary systems". In: *MNRAS* 396 (July 2009), pp. 1789–1796. DOI: 10.1111/j.1365-2966.2009.14868.x. arXiv:0812.1463.

[199] F. Pont and L. Eyer. "Isochrone ages for field dwarfs: method and application to the age-metallicity relation". In: *MNRAS* 351 (June 2004), pp. 487–504. DOI: 10.1111/j.1365-2966.2004.07780.x. eprint: arXiv:astro-ph/0401418.

[200] F. Pont, S. Zucker, and D. Queloz. "The effect of red noise on planetary transit detection". In: *MNRAS* 373 (Nov. 2006), pp. 231–242. DOI: 10.1111/j.1365-2966.2006.11012.x. eprint: arXiv:astro-ph/0608597.

[201] F. Pont et al. "A planet-sized transiting star around OGLE-TR-122. Accurate mass and radius near the hydrogen-burning limit". In: *A & A* 433 (Apr. 2005), pp. L21–L24. DOI: 10.1051/0004-6361:200500025. eprint: arXiv:astro-ph/0501611.

[202] F. Pont et al. "Determining eccentricities of transiting planets: a divide in the mass-period plane". In: *MNRAS* 414 (June 2011), pp. 1278–1284. DOI: 10.1111/j.1365-2966.2011.18462.x. arXiv:1103.2081 [astro-ph.EP].

[203] F. Pont et al. "Doppler follow-up of OGLE planetary transit candidates in Carina". In: *A & A* 438 (Aug. 2005), pp. 1123–1140. DOI: 10.1051/0004-6361:20052771. eprint: arXiv:astro-ph/0501615.

[204] F. Pont et al. "Spin-orbit misalignment in the HD 80606−planetary system". In: *A & A* 502 (Aug. 2009), pp. 695–703. DOI: 10.1051/0004-6361/200912463. arXiv:0906.5605.

[205] F. Primini, S. Rappaport, and P. C. Joss. "Pulse profile and refined orbital elements for SMC X-1". In: *ApJ* 217 (Oct. 1977), pp. 543–548. DOI: 10.1086/155603.

[206] D. Queloz et al. "Detection of a spectroscopic transit by the planet orbiting the star HD209458". In: *A & A* 359 (July 2000), pp. L13–L17. eprint: arXiv:astro-ph/0006213.

[207] S. N. Quinn et al. "HAT-P-25b: A Hot-Jupiter Transiting a Moderately Faint G Star". In: *ApJ* 745, 80 (Jan. 2012), p. 80. DOI: 10.1088/0004-637X/745/1/80. arXiv:1008.3565 [astro-ph.EP].

[208] S. Raetz et al. "Planetary transit observations at the University Observatory Jena: TrES-2". In: *Astronomische Nachrichten* 330 (May 2009), pp. 459–+. DOI: 10.1002/asna.200811202. arXiv:0905.1842.

[209] D. Ragozzine and A. S. Wolf. "Probing the Interiors of very Hot Jupiters Using Transit Light Curves". In: *ApJ* 698 (June 2009), pp. 1778–1794. DOI: 10.1088/0004-637X/698/2/1778. arXiv:0807.2856.

[210] F. A. Rasio et al. "Tidal Decay of Close Planetary Orbits". In: *ApJ* 470 (Oct. 1996), pp. 1187–+. DOI: 10.1086/177941. eprint: arXiv:astro-ph/9605059.

[211] Frederic A. Rasio and Eric B. Ford. "Dynamical Instabilities and the Formation of Extrasolar Planetary Systems". In: *Science* 274.5289 (1996), pp. 954–956. DOI: 10.1126/science.274.5289.954. eprint: http://www.sciencemag.org/cgi/reprint/274/5289/954.pdf. URL: http://www.sciencemag.org/cgi/content/abstract/274/5289/954.

[212] H. Rauer et al. "Transiting exoplanets from the CoRoT space mission. VII. The "hot-Jupiter"-type planet CoRoT-5b". In: *A & A* 506 (Oct. 2009), pp. 281–286. DOI: 10.1051/0004-6361/200911902. arXiv:0909.3397.

[213] S. N. Raymond, P. J. Armitage, and N. Gorelick. "Planet-Planet Scattering in Planetesimal Disks. II. Predictions for Outer Extrasolar Planetary Systems". In: *ApJ* 711 (Mar. 2010), pp. 772–795. DOI: 10.1088/0004-637X/711/2/772. arXiv:1001.3409 [astro-ph.EP].

[214] S. N. Raymond et al. "Planet-Planet Scattering Leads to Tightly Packed Planetary Systems". In: *ApJL* 696 (May 2009), pp. L98–L101. DOI: 10.1088/0004-637X/696/1/L98. arXiv:0903.4700 [astro-ph.EP].

[215] I. Ribas and J. Miralda-Escudé. "The eccentricity-mass distribution of exoplanets: signatures of different formation mechanisms?" In: *A & A* 464 (Mar. 2007), pp. 779–785. DOI: 10.1051/0004-6361:20065726. eprint: arXiv:astro-ph/0606009.

[216] I. Ribas et al. "The case for a close-in perturber to GJ 436 b". In: *IAU Symposium*. Vol. 253. IAU Symposium. Feb. 2009, pp. 149–155. DOI: 10.1017/S1743921308026343. arXiv:0807.0235.

[217] W. K. M. Rice, J. Veljanoski, and A. Collier Cameron. "Tidal evolution of close-in giant planets: evidence of type II migration?" In: *MNRAS* 425 (Oct. 2012), pp. 2567–2575. DOI: 10.1111/j.1365-2966.2012.21728.x. arXiv:1207.5970 [astro-ph.EP].

[218] R. A. Rossiter. "On the detection of an effect of rotation during eclipse in the velocity of the brigher component of beta Lyrae, and on the constancy of velocity of this system." In: *ApJ* 60 (July 1924), pp. 15–21. DOI: 10.1086/142825.

[219] D. Rouan et al. "Transiting exoplanets from the CoRoT space mission . XIX. CoRoT-23b: a dense hot Jupiter on an eccentric orbit". In: *A & A* 537, A54 (Jan. 2012), A54. DOI: 10.1051/0004-6361/201117916. arXiv:1112.0584 [astro-ph.EP].

[220] G. J. Savonije, J. C. B. Papaloizou, and F. Alberts. "Nonadiabatic Tidal Forcing of a Massive Uniformly Rotating Star". In: *MNRAS* 277 (Nov. 1995), p. 471.

[221] G. J. Savonije and M. G. Witte. "Tidal interaction of a rotating 1 vec {M_sun} star with a binary companion". In: *A & A* 386 (Apr. 2002), pp. 211–221. DOI: 10.1051/0004-6361:20020237. eprint: arXiv:astro-ph/0202276.

[222] K. C. Schlaufman. "Evidence of Possible Spin-orbit Misalignment Along the Line of Sight in Transiting Exoplanet Systems". In: *ApJ* 719 (Aug. 2010), pp. 602–611. DOI: 10.1088/0004-637X/719/1/602. arXiv:1006.2851 [astro-ph.EP].

[223] Y. Shen and E. L. Turner. "On the Eccentricity Distribution of Exoplanets from Radial Velocity Surveys". In: *ApJ* 685 (Sept. 2008), pp. 553–559. DOI: 10.1086/590548. arXiv:0806.0032.

[224] Avi Shporer et al. "HAT-P-9b: A LOW-DENSITY PLANET TRANSITING A MODERATELY FAINT F STAR". In: *The Astrophysical Journal* 690.2 (2009), pp. 1393–1400. URL: http://stacks.iop.org/0004-637X/690/1393.

[225] D. Sivia. *Data Analysis: A Bayesian Tutorial*. Ed. by John Skilling. 2006.

[226] B. Smalley et al. "WASP-34b: a near-grazing transiting sub-Jupiter-mass exoplanet in a hierarchical triple system". In: *A & A* 526 (Feb. 2011), A130+. DOI: 10.1051/0004-6361/201015992. arXiv:1012.2278 [astro-ph.EP].

[227] M. D. Snellgrove, J. C. B. Papaloizou, and R. P. Nelson. "On disc driven inward migration of resonantly coupled planets with application to the system around GJ876". In: *A & A* 374 (Aug. 2001), pp. 1092–1099. DOI: 10.1051/0004-6361:20010779. eprint: arXiv:astro-ph/0104432.

[228] J. Southworth et al. "High-precision photometry by telescope defocusing - I. The transiting planetary system WASP-5". In: *MNRAS* 396 (June 2009), pp. 1023–1031. DOI: 10.1111/j.1365-2966.2009.14767.x. arXiv:0903.2139 [astro-ph.EP].

[229] J. Southworth et al. "High-precision photometry by telescope defocusing - III. The transiting planetary system WASP-2". In: *MNRAS* 408 (Nov. 2010), pp. 1680–1688. DOI: 10.1111/j.1365-2966.2010.17238.x. arXiv:1006.4464 [astro-ph.EP].

[230] K. R. Stapelfeldt et al. "An Edge-On Circumstellar Disk in the Young Binary System HK Tauri". In: *ApJL* 502 (July 1998), p. L65. DOI: 10.1086/311479.

[231] T. Sumi et al. "Unbound or distant planetary mass population detected by gravitational microlensing". In: *Nature* 473 (May 2011), pp. 349–352. DOI: 10.1038/nature10092. arXiv:1105.3544 [astro-ph.EP].

[232] C. Terquem and J. C. B. Papaloizou. "Dynamical relaxation and the orbits of low-mass extrasolar planets". In: *MNRAS* 332 (May 2002), pp. L39–L43. DOI: 10.1046/j.1365-8711.2002.05493.x. eprint: arXiv:astro-ph/0203187.

[233] C. Terquem et al. "On the Tidal Interaction of a Solar-Type Star with an Orbiting Companion: Excitation of g-Mode Oscillation and Orbital Evolution". In: *ApJ* 502 (Aug. 1998), pp. 788–+. DOI: 10.1086/305927. eprint: arXiv:astro-ph/9801280.

[234] B. Tingley et al. "Transiting exoplanets from the CoRoT space mission. XVI. CoRoT-14b: an unusually dense very hot Jupiter". In: *A & A* 528, A97 (Apr. 2011), A97. DOI: 10.1051/0004-6361/201015480. arXiv:1101.1899 [astro-ph.EP].

[235] A. Tokovinin et al. "Tertiary companions to close spectroscopic binaries". In: *A & A* 450 (May 2006), pp. 681–693. DOI: 10.1051/0004-6361:20054427. eprint: arXiv:astro-ph/0601518.

[236] A. H. M. J. Triaud et al. "Spin-orbit angle measurements for six southern transiting planets. New insights into the dynamical origins of hot Jupiters". In: *A & A* 524 (Dec. 2010), A25+. DOI: 10.1051/0004-6361/201014525. arXiv:1008.2353 [astro-ph.EP].

[237] A. H. M. J. Triaud et al. "The Rossiter-McLaughlin effect of CoRoT-3b and HD 189733b". In: *A & A* 506 (Oct. 2009), pp. 377–384. DOI: 10.1051/0004-6361/200911897. arXiv:0907.2956.

[238] A. H. M. J. Triaud et al. "WASP-23b: a transiting hot Jupiter around a K dwarf and its Rossiter-McLaughlin effect". In: *A & A* 531 (July 2011), A24+. DOI: 10.1051/0004-6361/201016367. arXiv:1103.2603 [astro-ph.EP].

[239] A. H. M. J. Triaud et al. "WASP-80b: a gas giant transiting a cool dwarf". In: *A & A* 551, A80 (Mar. 2013), A80. DOI: 10.1051/0004-6361/201220900. arXiv:1303.0254 [astro-ph.EP].

[240] D. E. Trilling, J. I. Lunine, and W. Benz. "Orbital migration and the frequency of giant planet formation". In: *A & A* 394 (Oct. 2002), pp. 241–251. DOI: 10.1051/0004-6361:20021108. eprint: arXiv:astro-ph/0208184.

[241] B. L. Van Der Waerden. "The Heliocentric System in Greek, Persian and Hindu Astronomy". In: *Annals of the New York Academy of Sciences* 500.1 (1987), pp. 525–545. ISSN: 1749-6632. DOI: 10.1111/j.1749-6632.1987.tb37224.x. URL: http://dx.doi.org/10.1111/j.1749-6632.1987.tb37224.x.

[242] D. Veras and P. J. Armitage. "Predictions for the Correlation between Giant and Terrestrial Extrasolar Planets in Dynamically Evolved Systems". In: *ApJ* 645 (July 2006), pp. 1509–1515. DOI: 10.1086/504582. eprint: arXiv:astro-ph/0604077.

[243] D. Veras and P. J. Armitage. "The Influence of Massive Planet Scattering on Nascent Terrestrial Planets". In: *ApJL* 620 (Feb. 2005), pp. L111–L114. DOI: 10.1086/428831. eprint: arXiv:astro-ph/0501356.

[244] D. Veras and S. N. Raymond. "Planet-planet scattering alone cannot explain the free-floating planet population". In: *MNRAS* 421 (Mar. 2012), pp. L117–L121. DOI: 10.1111/j.1745-3933.2012.01218.x. arXiv:1201.2175 [astro-ph.EP].

[245] J. Wang and E. B. Ford. "On the eccentricity distribution of short-period single-planet systems". In: *MNRAS* 418 (Dec. 2011), pp. 1822–1833. DOI: 10.1111/j.1365-2966.2011.19600.x. arXiv:1108.1811 [astro-ph.EP].

[246] W. R. Ward. "Survival of Planetary Systems". In: *APJ* 482 (June 1997), pp. L211+. DOI: 10.1086/310701.

[247] S. J. Weidenschilling and F. Marzari. "Gravitational scattering as a possible origin for giant planets at small stellar distances". In: *Nature* 384 (Dec. 1996), pp. 619–621. DOI: 10.1038/384619a0.

[248] W. F. Welsh et al. "The Discovery of Ellipsoidal Variations in the Kepler Light Curve of HAT-P-7". In: *ApJL* 713 (Apr. 2010), pp. L145–L149. DOI: 10.1088/2041-8205/713/2/L145. arXiv:1001.0413 [astro-ph.SR].

[249] R. G. West et al. "The sub-Jupiter mass transiting exoplanet WASP-11b". In: *A & A* 502 (July 2009), pp. 395–400. DOI: 10.1051/0004-6361/200810973. arXiv:0809.4597.

[250] D. M. Wilson et al. "WASP-4b: A 12th Magnitude Transiting Hot Jupiter in the Southern Hemisphere". In: *The Astrophysical Journal Letters* 675.2 (2008), pp. L113–L116. URL: http://stacks.iop.org/1538-4357/675/L113.

[251] J. N. Winn. *Exoplanets (Exoplanet Transits and Occultations)*. Ed. by S. Seager. University of Arizona Press, 2010, pp. 55–77.

[252] J. N. Winn and M. J. Holman. "Obliquity Tides on Hot Jupiters". In: *ApJL* 628 (Aug. 2005), pp. L159–L162. DOI: 10.1086/432834. eprint: arXiv:astro-ph/0506468.

[253] J. N. Winn et al. "HAT-P-7: A Retrograde or Polar Orbit, and a Third Body". In: *ApJL* 703 (Oct. 2009), pp. L99–L103. DOI: 10.1088/0004-637X/703/2/L99. arXiv:0908.1672.

[254] J. N. Winn et al. "Hot Stars with Hot Jupiters Have High Obliquities". In: *ApJL* 718 (Aug. 2010), pp. L145–L149. DOI: 10.1088/2041-8205/718/2/L145. arXiv:1006.4161 [astro-ph.EP].

[255] J. N. Winn et al. "Measurement of the Spin-Orbit Alignment in the Exoplanetary System HD 189733". In: *ApJL* 653 (Dec. 2006), pp. L69–L72. DOI: 10.1086/510528. eprint: arXiv:astro-ph/0609506.

[256] J. N. Winn et al. "The Transit Light Curve Project. XI. Submillimagnitude Photometry of Two Transits of the Bloated Planet WASP-4b". In: *AJ* 137 (Apr. 2009), pp. 3826–3833. DOI: 10.1088/0004-6256/137/4/3826. arXiv:0901.4346 [astro-ph.EP].

[257] M. G. Witte and G. J. Savonije. "Tidal evolution of eccentric orbits in massive binary systems. A study of resonance locking". In: *A & A* 350 (Oct. 1999), pp. 129–147. eprint: arXiv:astro-ph/9909073.

[258] A. Wolszczan and D. A. Frail. "A planetary system around the millisecond pulsar PSR1257+12". In: *Nature* 355 (Jan. 1992), pp. 145–147. DOI: 10.1038/355145a0.

[259] J. T. Wright et al. "Ten New and Updated Multiplanet Systems and a Survey of Exoplanetary Systems". In: *ApJ* 693 (Mar. 2009), pp. 1084–1099. DOI: 10.1088/0004-637X/693/2/1084. arXiv:0812.1582.

[260] Y. Wu and N. Murray. "Planet Migration and Binary Companions: The Case of HD 80606b". In: *ApJ* 589 (May 2003), pp. 605–614. DOI: 10.1086/374598. eprint: arXiv:astro-ph/0303010.

[261] J. P. Zahn. "Forced Oscillations in Close Binaries. The Adiabatic Approximation". In: *A & A* 4 (Mar. 1970), p. 452.

[262] J.-P. Zahn. "Physical mechanisms for tidal dissipation". In: Astronomical Society of the Pacific Conference Series 333 (Nov. 2005). Ed. by A. Claret, A. Giménez, & J.-P. Zahn, pp. 4–+.

[263] J.-P. Zahn. "The dynamical tide in close binaries". In: *A & A* 41 (July 1975), pp. 329–344.

[264] J.-P. Zahn. "Tidal dissipation in binary systems". In: EAS Publications Series 29 (2008). Ed. by M.-J. Goupil & J.-P. Zahn, pp. 67–90. DOI: 10.1051/eas:0829002. arXiv:0807.4870.

[265] J.-P. Zahn. "Tidal evolution of close binary stars. I - Revisiting the theory of the equilibrium tide". In: *A & A* 220 (Aug. 1989), pp. 112–116.

[266] J.-P. Zahn. "Tidal friction in close binary stars". In: *A & A* 57 (May 1977), pp. 383–394.

[267] N. L. Zakamska, M. Pan, and E. B. Ford. "Observational biases in determining extrasolar planet eccentricities in single-planet systems". In: *MNRAS* (Oct. 2010), pp. 1566–+. DOI: 10.1111/j.1365-2966.2010.17570.x. arXiv:1008.4152 [astro-ph.EP].

[268] S. Zucker and T. Mazeh. "On the Mass-Period Correlation of the Extrasolar Planets". In: *ApJL* 568 (Apr. 2002), pp. L113–L116. DOI: 10.1086/340373. eprint: arXiv:astro-ph/0202415.